Potential of Optical Remote Sensing for the Analysis of Salt Pan Environments

Robert Milewski

A cumulative dissertation

in partial fulfillment of the requirements for the academic degree of
“doctor rerum naturalium” (Dr. rer. nat.)
in the academic discipline "Remote Sensing"

submitted to the Faculty of Science
Institute of Geosciences
at Potsdam University
and
the German Research Centre for Geosciences (GFZ)

Place and date of the disputation: Potsdam, 05.05.2020

Primary supervisor: Prof. Dr. Luis Guanter
Secondary supervisor: Prof. Dr. Bodo Bookhagen
Further reviewers: Prof. Dr. Frank Eckardt, Prof. Dr. Helmut Echtler

Published online in the
Institutional Repository of the University of Potsdam:
https://doi.org/10.25932/publishup-47373
https://nbn-resolving.org/urn:nbn:de:kobv:517-opus4-473732

Abstract

Salt pans also termed playas are common landscape features of hydrologically closed basins in arid and semiarid zones, where evaporation significantly exceeds the local precipitation. The analysis and monitoring of salt pan environments is important for the evaluation of current and future impact of these landscape features. Locally, salt pans have importance for the ecosystem, wildlife and human health, and through dust emissions they influence the climate on regional and global scales. Increasing economic exploitation of these environments in the last years, e.g. by brine extraction for raw materials, as well as climate change severely affect the water, material and energy balance of these systems. Optical remote sensing has the potential to characterise salt pan environments and to increase the understanding of processes in playa basins, as well as to assess wider impacts and feedbacks that exist between climate forcing and human intervention in their regions. Remote sensing techniques can provide information for extensive regions on a high temporal basis compared to traditional field samples and ground observations. Specifically, for salt pans that are often challenging to study because of their large size, remote location, and limited accessibility due to missing infrastructure and ephemeral flooding. Furthermore, the availability of current and upcoming hyperspectral remote sensing data opened the opportunity for the analyses of the complex reflectance signatures that relate to the mineralogical mixtures found in the salt pan sediments. However, these new advances in sensor technology, as well as increased data availability currently have not been fully explored for the study of salt pan environments. The potential of new sensors needs to be assessed and state of the art methods need to be adapted and improved to provide reliable information for in depth analysis of processes and characterisation of the recent condition, as well as to support long-term monitoring and to evaluate environmental impacts of changing climate and anthropogenic activity.

This thesis provides an assessment of the capabilities of optical remote sensing for the study of salt pan environments that combines the information of hyperspectral data with the increased temporal coverage of multispectral observations for a more complete understanding of spatial and temporal complexity of salt pan environments using the Omongwa salt pan located in the south-west Kalahari as a test site. In particular, hyperspectral data are used for unmixing of the mineralogical surface composition, spectral feature-based modelling for quantification of main crust components, as well as time-series based classification of multispectral data for the assessment of the long-term dynamic and the analysis of the seasonal process regime. The results show that the surface of the Omongwa pan can be categorized into three major crust types based on diagnostic absorption features and mineralogical ground truth data. The mineralogical crust

types can be related to different zones of surface dynamic as well as pan morphology that influences brine flow during the pan inundation and desiccation cycles. Using current hyperspectral imagery, as well as simulated data of upcoming sensors, robust quantification of the gypsum component could be derived. For the test site the results further indicate that the crust dynamic is mainly driven by flooding events in the wet season, but it is also influenced by temperature and aeolian activity in the dry season. Overall, the scientific outcomes show that optical remote sensing can provide a wide range of information helpful for the study of salt pan environments. The thesis also highlights that remote sensing approaches are most relevant, when they are adapted to the specific site conditions and research scenario and that upcoming sensors will increase the potential for mineralogical, sedimentological and geomorphological analysis, and will improve the monitoring capabilities with increased data availability.

Zusammenfassung

Salzpfannen, auch Playas genannt, sind häufige Landschaftsformen endorheischer Becken in ariden und semi-ariden Zonen, in denen die Evaporation den lokalen Niederschlag deutlich übersteigt. Die Analyse und das Monitoring von Salzpfannen sind wichtig für die Bewertung des aktuellen und zukünftigen Wandels dieser Systeme. Salzpfannen haben große Bedeutung für das lokale Ökosystem, für die Gesundheit von Mensch und Tier, und durch ihre Staubemissionen können sie das Klima auf regionaler und globaler Ebene beeinflussen. Die zunehmende industrielle Nutzung dieser Räume in den letzten Jahren, z.B. durch Soleförderung zur Rohstoffgewinnung, sowie der Klimawandel haben erhebliche Auswirkungen auf ihre Wasser-, Stoff- und Energiebilanz. Die optische Fernerkundung bietet das Potenzial diese Landschaftsformen zu charakterisieren, Veränderungen zu erkennen und das Prozessverständnis zu fördern, sowie umfassende Auswirkungen und Rückkopplungen zwischen klimatischen und anthropogenen Einflüssen in diesen Regionen zu erkennen. Im Vergleich zu traditionellen Feldmethoden bietet der Einsatz von Fernerkundung eine Basis für großräumige und wiederholte Untersuchungen. Das gilt insbesondere für Salzpfannen, die aufgrund ihrer Größe, abgelegener Lage und durch begrenzte Zugänglichkeit, aufgrund fehlender Infrastruktur und episodischen Überschwemmungen, häufig schwer zu untersuchen sind. Darüber hinaus eröffnete die aktuelle und zukünftig gesteigerte Verfügbarkeit von hyperspektralen Fernerkundungsdaten die Möglichkeit zur detaillierten Analyse der Reflexionseigenschaften der komplexen Mineralogie und Sedimenteigenschaften von Salzpfannenoberflächen. Der Einsatz neuer Sensorik sowie die erhöhte Datenverfügbarkeit sind jedoch derzeit noch nicht ausreichend für die Untersuchung von Salzpfannen erforscht. Das Potenzial neuer Sensoren muss bewertet und die aktuelle Methodik angepasst und verbessert werden, um zuverlässige Informationen für die Charakterisierung und Analyse des aktuellen Zustands zu liefern, sowie eine langfristige Überwachung und Bewertung der Auswirkungen von Klimaveränderung und der anthropogenen Aktivität auf Salzpfannen und deren Regionen zu ermöglichen.

Diese Arbeit bietet eine Bewertung des Potentials der optischen Fernerkundung für die Untersuchung von Salzpfannen. Der Fokus liegt insbesondere auf der kombinierten Nutzung der analytischer Stärke von hyperspektralen Daten mit der erhöhten zeitlichen Auflösung von multispektralen Beobachtungen, um ein gesteigertes Verständnis der räumlichen und zeitlichen Komplexität von Salzpfannen zu erreichen. Als Testgebiet hierfür dient die Omongwa Salzpfanne in der Süd-Westlichen Kalahari. Im Rahmen dieser Arbeit werden hyperspektrale Fernerkundungsdaten für die spektrale Entmischung der mineralogischen

Oberflächenzusammensetzung und für die Quantifizierung mittels spektraler Parameter genutzt. Gleichzeitig ermöglicht die multitemporale Klassifikation von Multispektraldaten die Beurteilung der Langzeitdynamik und die Analyse des saisonalen Prozessgeschehens. Die Ergebnisse zeigen, dass die Oberfläche der Omongwa-Salzpfanne in drei Hauptklassen, dominiert von verschiedenen Evaporitmineralen, eingeteilt werden kann, die aufgrund diagnostischen Absorptionsmerkmalen und durch die Analyse von in-situ Daten unterschieden werden können. Diese mineralogischen Hauptklassen korrelieren mit Zonen unterschiedlicher zeitlicher Dynamik, sowie mit dem morphologischen Aufbau der Salzpfanne, die die räumliche Verteilung von Oberflächenwasser während episodischer Flutungen und die Ausfällung von Salzen während der Trockenzeiten beeinflussen. Des Weiteren konnte auf Grundlage hyperspektralen Daten von aktuellen Sensoren, sowie anhand simulierten Daten von in Planung befindlicher Sensoren eine robuste Quantifizierung der Gipskomponente in den Oberflächensedimenten abgeleitet werden. Für das Untersuchungsgebiet deuten die Ergebnisse der Zeitreihenanalyse darauf hin, dass die Krustendynamik und Oberflächenmineralogie hauptsächlich durch die wiederkehrenden Überschwemmungsereignisse in der Regenzeit geprägt sind, aber auch durch die Temperatur und äolische Aktivität in der Trockenzeit beeinflusst wird. Zusammenfassend zeigen die Ergebnisse, dass die optische Fernerkundung großes Potenzial zur genaueren Erforschung von Salzpfannen bietet und detaillierte Informationen zu saisonalen und langzeitlichen Veränderungen liefern kann. Die Arbeit hebt auch hervor, dass der Einsatz von Fernerkundungsmethoden am erfolgreichsten ist, wenn sie an die lokalen Bedingungen und die Forschungsfrage angepasst werden. Der Ausblick zeigt, dass zukünftige Sensoren die Möglichkeiten für die Erforschung dieser Räume weiter erhöhen und ein systematisches Monitoring durch die größere Datenverfügbarkeit verbessert wird.

Contents

Figures

Tables

Abbreviations

ASD	Analytical Spectral Devices
ASTER	Advanced Spaceborne Thermal Emission and Reflection Radiometer
AVHRR	Advanced Very High Resolution Radiometer
AVIRIS	Airborne Visible / Infrared Imaging Spectrometer
BMBF	German Federal Ministry of Education and Research
CHIME	Copernicus Hyperspectral Imaging Mission
CRAD	Continuum Removed Absorption Depth
DSM	Digital Surface Model
ECMWF	European Centre for Medium-Range Weather Forecasts
EMIT	Earth Surface Mineral Dust Source Investigation
EnMAP	Environmental Mapping and Analysis Program
EO-1	Earth Observing-1
ESA	European Space Agency, European Space Agency
GCP	Ground Control Point
GFZ	German Research Centre for Geosciences
HyMap	Hyperspectral Mapper
IR-MAD	Iterative-reweighted Multivariate Alteration Detection
ISS	International Space Station
LiDAR	Light Detection and Ranging
MODIS	Moderate Resolution Imaging Spectroradiometer
NASA	National Aeronautics and Space Administration
NDGI	Normalized Differenced Gypsum Index
NDWI	Normalized Differenced Water Index
OLI	Operational Land Imager
PLSR	Partial Least-Squares Regression
PRISMA	PRecursore IperSpettrale della Missione Applicativa
PSR	Portable Spectroradiometer
RADAR	RAdio Detection And Ranging
RMSE	Root Mean Square Error
SBG	Surface Biology and Geology
SHALOM	Spaceborne Hyperspectral Applicative Land and Ocean Mission
SLC	Scan Line Corrector
SMA	Spectral Mixture Analysis
SMACC	Sequential Maximum Angle Convex Cone
SPACES	Science Partnerships for the Assessment of Complex Earth System Processes
SWIR	Short-Wave Infrared
TOA	Top Of Atmosphere
VNIR	Visible Near-Infrared
XRD	X-Ray Diffraction

Chapter I - Introduction

1. Rationale and Structure

Salt pans or playas are common landscape features of hydrologically closed basins in arid and semiarid zones, where evaporation significantly exceeds the local precipitation (Shaw & Bryant, 2011). Although these environments represent only a small proportion of modem drylands, approximately ~5% after Cooke & Warren (1973), locally, they are of high ecological and economic significance, and even influence the regional and global climate through dust emissions. Specifically, for the southern Kalahari, Lancaster (1978) describes pans as "the principal geomorphic feature [...], which breaks the monotony of this otherwise almost featureless sand plain" that regionally can cover more than 20% of the land surface (Goudie & Wells, 1995). In Namibia and Southern Africa, any depression that holds water after a period of rain is called a pan. The term pan will be used synonymous with the term playa, defined by Neal (1975) as the flat central portion of the depression that may be covered by water after rain. The term salt or saline in conjunction with pan or playa refers to hydrologically closed depressions, where the evaporation exceeds water inflows and which sediments therefore contain a significant proportion of evaporite minerals such as sodium chloride (NaCl, 'common salt'), calcium carbonate ($CaCO_3$), calcium sulphate in its hydrous form (gypsum, $CaSO_4 \cdot 2H_2O$) or its dehydrated form (anhydrite $CaSO_4$) (Fookes & Lee, 2018).

Scientifically, salt pans have become increasingly important for the elucidation of palaeoenvironmental conditions from their sediments and landforms (M. Telfer, 2006), whilst also have being recognised as major sources for atmospheric dust (Prospero, Ginoux, Torres, Nicholson, & Gill, 2002), which calls for a regular monitoring of these environments (Shaw & Bryant, 2011). Salt pans can provide valuable information on the environment, because their morphological, as well as sedimentary and mineralogical characteristics can be related to fluvial or aeolian processes and climate drivers that controlled their formation or later modified them (Robert G. Bryant, 1999). The information gained from pans often have importance beyond their size, with environmental processes not only affecting the pan surrounding, but their emissions influence the climate on regional and even global scales (Lancaster, 2009). The composition of exposed salt pan surfaces can also affect human health, e.g. directly through emissions of heavy metals and small dust particles (Plumlee & Ziegler, 2003), as well as by providing suitable living conditions for microbes or fungi that can potentially functions as pathogens (Bultman, Fisher, & Pappagianis, 2013), which are determined by the pan environment and its dynamics. The various sediments and minerals of playa lake basins can also have economic significance and may take on greater relevance with the ever-

increasing demand for natural resources (Chapman, Rothery, Francis, & Pontual, 1989; Matter & Tucker, 1978). The economic potential of salt pan deposits is already known since decades, e.g. as an exploitable source for uranium in the energy sector or as agricultural fertilizer (Reeves, 1978). The importance further increased in recent years specifically by growing demand for lithium for energy storage technology that is currently fuelling a boom in exploration for new sources and feasibility studies (Kavanagh, Keohane, Garcia Cabellos, Lloyd, & Cleary, 2018). Some of the most promising lithium sources are salt pans of the closed drainage basins in the Andes of South America (Godfrey et al., 2013). Remote sensing can not only contribute to the exploration, but may be even more relevant in the monitoring of such economic exploitations and their influence to the pan dynamic, as well as the environmental consequences of such activities. For example, the extraction of salt rich brines is reported to cause drastic changes in the pan surface properties (Bowen, Kipnis, & Raming, 2017), and can lead to increased activity in pan emissions, due to reduction in groundwater level (Pelletier, 2006). The direct and indirect environmental impacts of industrial salt extraction also threaten the traditional use of salt pans for domestic purposes, e.g. to provide cattle with essential salt nutrients for their diet (Saayman, 2013). Furthermore, the pans of the Kalahari region are a preferred wildlife habitat as they provide natural mineral licks, protection from predators and an ephemeral source of drinking water (Bergström & Skarpe, 1999; Parris & Child, 1979; Selebatso, Bennitt, Maude, & Fynn, 2018). Finally, salt pan environments serve more exotic uses such as testing ranges for high speed vehicles and jet engines (Carpenter, Wallace, & Hamre, 2002), and provide a unique setting for geotourism (Dowling & Newsome, 2018), that are also challenged by degradation of the surface crust due to climate change and/or economic exploitation (Bowen et al., 2018).

However, the observation and monitoring of playa environments is a challenging task. Many of the processes related to formation and evolution of these landforms and their sediments are difficult to monitor using conventional ground-based instrumentation because of: (1) high-magnitude and low-frequency events such as episodic flooding; (2) strong seasonal patterns, which can include a change in the dominant process regime (e.g. from fluvial to aeolian during the season); (3) changes that are spatially discrete and uncorrelated to the development of the whole salt pan environment and therefore missed by point based observations (Millington, Jones, Quarmby, & Townshend, 1987). From a practical perspective, the application of ground-based observation and monitoring is further challenged by limited accessibility to salt pans, in time of partial or total flooding, as well as by generally harsh climatic and working conditions and limited infrastructure in these often remote and extensive arid areas (Robert G. Bryant, 1996). To overcome these difficulties a fair number of

studies have applied remote sensing techniques to study salt pan evaporite environments and were able to provide spatial information on pan surfaces in terms of evaporite mineral distribution supported by field observations. Most of them rely on optical multispectral satellite sensors (e.g. Alanazi & Ghrefat, 2013; Robert G. Bryant, 1999; Millington et al., 1989; White & Eckardt, 2006) that often do not provide the necessary spectral resolution to cover the spectral complexity of evaporite mineral assemblages on salt pan surfaces (Hubbard & Crowley, 2005). In comparison, analysis based on advanced hyperspectral imagery are more sensitive for the identification and quantification of a wider range of evaporite minerals (Robert G. Bryant, 1999; Kodikara et al., 2012), and usually achieve higher modelling results (Hubbard & Crowley, 2005). However, currently hyperspectral data are not as easily available as multispectral data and therefore only provide a mono-temporal assessment of the playa environment. In the frame of the BMBF funded SPACES GeoArchive project this thesis provides an assessment of the capabilities of optical remote sensing for the characterisation of salt pan environments that combines the information of hyperspectral data with the increased temporal coverage of multispectral observations for a more complete understanding of spatial and temporal complexity of salt pan environments.

The thesis comprises five main chapters. Chapter I gives an overview of the general research background, presents the specific research framework and poses main research objectives and research questions. Chapters II-IV present consecutive stand-alone manuscripts, whose sub-objectives contribute to the overall thesis. Chapter II provides a spatial comprehensive study of the surface mineralogy of the Omongwa salt pan using hyperspectral EO-1 Hyperion data and the assessment of the long-term surface dynamic covering the last 30 years since 1984 by exploiting the rich data archive of the multispectral satellites of the Landsat-series. Results are linked to the morphology of pan setting for interpretation of the pan's depositional environments. Following this assessment, Chapter III evaluates the capability of hyperspectral sensors at laboratory, airborne and spaceborne scale for the quantification of the mineralogical fraction in the salt pan surface sediments using the example of the gypsum mineral and proposes a robust and transferable approach in support of regular monitoring using current and upcoming hyperspectral sensors. Chapter IV focuses on temporally dense seasonal and inter-annual analysis using well established multispectral data of the Landsat OLI sensor that cover the surface changes of three major wet-dry cycles and provides an assessment of climatic parameters, such as the pan's moisture regime and aeolian activity that may drive the observed surface changes. The mineralogical classification provided in Chapter II based on hyperspectral data is also used in Chapter III to assess the potential and limitation of the crust type mapping using broad multispectral bands of the Landsat OLI sensor.

Finally, Chapter V builds a synthesis form the previously established results and provides an outlook regarding further research demands, as well as an assessment of complementary research approaches.

2. Research Background

The research background provides an overview of state of the art in optical remote sensing for pan environments in general (Section I-2.1) and the potential of advanced hyperspectral remote sensing in particular (Section I-2.2), as well as on the physical properties and dynamic of playa environments (Section I-2.3).

2.1 Optical remote sensing for pan environments

Optical remote sensing has the potential to characterise playa environments and to increase the understanding of processes in playa basins, as well as to assess wider impacts and feedbacks that exist between climate forcing and human intervention in their regions (Shaw & Bryant, 2011). Optical remote sensing of salt pans surfaces is based on the spectral reflectance properties of the different mineralogical and organic components present in the salt pan surface sediments. The Visible and Near-Infrared spectral range (VNIR, 0.4 – 1 µm) is primarily influenced by the highly reflective properties of salt minerals, such as halite and sedimentary components such as weathered silicate or carbonate minerals that depend on the lithological background of the playa environment (Robert G. Bryant, 1996; J.K. Crowley, 1993; Drake, 1995). The region is further influenced by the broad absorption features of metal (mainly iron)-oxides and hydroxides as well as organic matter introduced into the pan sediments. The Short-Wave Infrared (SWIR, 1 – 2.5 µm) spectral region is predominantly sensitive to a wide variety of minerals, like clays, carbonates and sulphates that have more discrete or sharp absorption features that are mostly too narrow to be accurately identified by broadband multispectral data (Chabrillat, Goetz, Krosley, & Olsen, 2002; Hunt, Salisbury, & Lenhoff, 1971). In addition to these chemical components, most physical properties of the salt pan surface such as the texture and roughness of the sediments, as well as water content affect the shape of the spectral curve through changes in baseline height and influence the absorption feature intensities (E. Ben-Dor et al., 2009).

Optical multispectral remote sensing data have been used to map and monitor the playa environments with evaporite surfaces on many different scales and sensors. Castañeda, Herrero, & Casterad (2005) used Landsat data to map depositional environments for the pans of the Monegros area in Northern Spain. Her studies focus on the differentiation of vegetated, wet, watery, and dry bare ground, which are robustly separable with multispectral data. For more complex differentiation of sedimentary surfaces in terms of evaporite mineralogy or clay rich crust types a number of studies used field samples and field or laboratory spectroscopy to determine which evaporite minerals can be differentiated and mapped with optical remote sensing. E.g. Chapman et

al. (1989) and Flahaut et al. (2017) could capture the majority of the mineralogical information and map mineral zones within the salt pans of the Andean highlands in Southern America using a combination of multispectral Landsat data and field spectroscopy and relate this information to local bedrock as well as hydrochemical conditions. For the endorheic basins of Northern Africa, the so-called Chotts, a rich basis of scientific studies has applied optical remote sensing for the study of these playa environments. Among their many results, they show that it is possible to differentiate evaporite rich sediments, most notably gypsum and halite dominated surfaces, using Landsat data and to apply this knowledge for the analysis of sediment transport processes (Abbas, Deroin, & Bouaziz, 2018; Drake, Bryant, Millington, & Townshend, 1994; Millington et al., 1989). For example the work of Bryant (1999) on the Chott el Djerid showed that the abundance of gypsum in the salt pan surface sediments can be estimated using mineralogical information from ground reference samples to calibrate Landsat based linear mixture models with good results, but a limited samples size ($r^2 > 0.8$, $n = 12$). Similar remote sensing studies by White & Eckardt (2006) on the Makgadikgadi pan complex in northern Botswana used MODIS and Landsat data to estimate abundancies of calcium carbonate in a similar methodological approach with more mixed results ($r^2 \approx 0.36\text{-}0.51$). However, already the relative mineralogical information on calcite surface distribution was useful to assess aeolian, fluvial and groundwater processes of the pan system (White & Eckardt, 2006).

2.2 Hyperspectral remote sensing

Whereas multispectral systems cover the optical region in a few very broad spectral channels, hyperspectral sensors, also termed imaging spectrometers, register hundreds of narrow, overlapping spectral bands that compose a continuous spectrum (Meer & Jong, 2007). Commonly, but not exclusively, the starting point of hyperspectral sensors is defined to begin with a band-pass smaller than 20 nm for each spectral band (Veraverbeke et al., 2018). The high spectral resolution enables a wide range of applications that require an accurate identification of materials or estimation of physical parameters, but usually require more sophisticated and complex data analysis methods to account for the higher dimensionality and size of the hyperspectral data (Bioucas-Dias et al., 2013). Over the last decades, hyperspectral remote sensing has opened the optical-reflective domain of the VNIR and SWIR part of electromagnetic spectrum with a large number of available hyperspectral radiometers today at ground or field level (e.g. ASD FieldSpec, Spectral Evolution PSR+), with imaging spectrometers mounted on aircrafts (e.g., AVIRIS, HyMap, HySpex, AisaFenix), and is currently emerging at the spaceborne scale with the integration of such sensors on earth-observing platforms (Bioucas-Dias et al., 2013; Guanter et al., 2018; Plaza et al., 2009). Regarding the satellite level, the only publicly available source of hyperspectral imagery that

covers the VNIR-SWIR spectral range in the last years has been acquired by the Hyperion sensor mounted on NASA's Earth Observing-1 (EO-1) satellite (Ungar, Pearlman, Mendenhall, & Reuter, 2003). The mission launched in 2000 and was originally planned with a lifetime of only one year and a technical exploration objective, specifically to enable the development of future Earth imaging technologies, but the mission did finally run for more than 16 years until the satellite was decommissioned in 2017 (Franks et al., 2017). Compared to controlled conditions in the laboratory, imaging spectroscopy at the air- and spaceborne level is encumbered by problems such as changes in viewing and illumination angles, atmospheric attenuation and relatively low signal-to-noise ratios (Eyal Ben-Dor, Irons, & Epema, 1999). Although these challenges that influence the quality of the remote sensing data still exist, major progress has been made to account for geometric, atmospheric and sensor related quality issues with state-of-the-art sensor design and processing approaches (Plaza et al., 2009; Richter & Schläpfer, 2002). Careful and sensor adapted calibration, application of normalisation techniques, as well as noise management can significantly improve the data basis even for sensors affected by high background noise (Datt, McVicar, Niel, Jupp, & Pearlman, 2003).

For the remote sensing of playa environments, the availability of hyperspectral data opened the opportunity for the analyses of the complex reflectance signatures that are the result of mineralogical mixtures found in the sediments of playa environments (Ghrefat & Goodell, 2011; Hubbard & Crowley, 2005). The advent of imaging spectrometers mounted on airplanes in the 1990s and use of hyperspectral data could provide major insights on the link between the salt pan mineralogy and surface reflectance in the VNIR-SWIR spectral range for a wide range of evaporite minerals over selected test sites (James K. Crowley, 1991; J.K. Crowley, 1993; Drake, 1995). These studies showed that many evaporite surfaces exhibit spectral absorption features that are related to their molecular properties and originate from the absorption of electromagnetic radiation due to either electronic or vibrational processes (Clark, King, Klejwa, Swayze, & Vergo, 1990). For evaporite minerals the vibrational processes mainly caused by excitation of atomic-bonds of the ion groups carbonates (CO_3), sulphates (SO_4), nitrates (NO_3), or ammonium (NH_4) that can be exploited for their discrimination by hyperspectral remote sensing (James K. Crowley, 1991; Drake, 1995). Although some evaporite minerals may have absorption features in a similar position, the large variations in number, spacing, size and shape of these features mean that their spectra can still be differentiated and considered diagnostic, especially if the specific evaporite environment is considered in the analysis. The identification of a particular suite of evaporite minerals further allows to distinguish between different brine and playa types and gives inside to specific

environmental conditions that are related to their formation (Drake, 1995). Hyperspectral data have also been proven useful for the related topics such as the general assessment of salinity (E. Ben-Dor, 2002; Farifteh, Meer, & Carranza, 2007), as well as the classification of halophytic vegetation of salt pans and irrigated soils (Dehaan & Taylor, 2001; A. Dutkiewicz, Lewis, & Ostendorf, 2009).

Currently, the main limitation for hyperspectral remote sensing approaches is still the data availability, coverage and frequency of observations, which prevents more extensive use or multitemporal assessments. Technical constraints in the definition of imaging spectrometers and the fraction of radiant flux available to the sensors usually make it necessary to trade spatial resolution as well as the sensor's footprint (also called swath width for line scanners) against higher spectral coverage and resolution, as opposed to multispectral sensors that are typically designed to maximize spatial and temporal resolution. According to these technical properties, major synergy lies in the complementary use of high frequency multispectral observations combined with the analytic strength of hyperspectral data (Guanter et al., 2018). Recent advances in optical remote sensing such as the European Space Agency's multispectral Sentinel-2 satellite (Drusch et al., 2012), the just launched hyperspectral mission of the Italian Space Agency PRISMA (Hyperspectral Precursor of the Application Mission) (Loizzo et al., 2018), as well as a wide range of upcoming hyperspectral missions, like the German Aerospace Agency's EnMAP (Environmental Mapping and Analysis Program) (Guanter et al., 2015) with scheduled for launch end of 2020 and the Italian-Israeli SHALOM (Spaceborne Hyperspectral Applicative Land and Ocean Mission) satellite, which is designed to provide higher spatial resolution of 10 m and a focus on commercial applications (Feingersh & Ben-Dor, 2015), will offer an improved databasis for exploitation of hyperspectral techniques, as well as synergetic use with multispectral imagery. A further hyperspectral sensor with the scheduled for 2022 is the Earth Surface Mineral Dust Source Investigation (EMIT), which will be mounted to the exterior of the International Space Station (ISS), with the direct mission objective to determine the mineral composition of natural sources that produce dust aerosols around the world (R. Green et al., 2019). Currently under discussion are also the next generation of hyperspectral satellite missions like ESA'S new Sentinel candidate the Copernicus Hyperspectral Imaging Mission (CHIME) (Nieke & Rast, 2018), as well as NASA's Biology and Geology (SBG). Both of these satellites will be designed to operationally acquire hyperspectral imagery over larger areas and much more frequently than the previous listed tasking missions. The technical developments of these sensors and platforms will provide new opportunities for improved characterisation and

monitoring of complex salt pan environments and their dynamics in the context of climate change and anthropogenic impact.

2.3 Playa environments and their dynamic

English-speaking geoscientists have turned to a variety of foreign language terms to describe the flat, mainly barren, periodically flooded and often salt-crusted basin of arid areas. Next to several other terms, these features have been called playas, salinas, salt pans or flats (Fookes & Lee, 2018). These flat, shallow depressions floored with mostly layered sediments are often salt rich and dry except when flooding turns them into a temporary, also termed ephemeral, saline lake environment (Eugster & Hardie, 1978). Salt pans can vary in size from small salt flats of less than 1 km² in areal extent to giants thousands of square kilometres in area, such as the Etosha and Makgadikgadi pan in Namibia or the salt pan at Lake Uyuni, Bolivia that covers more than 10,000 km². Continental saline pans occupy the lowest areas of closed arid basins. The flat, salt-encrusted pan surface often is surrounded by a brine-soaked mudflat permeated with evaporite minerals that grew within the sediment, and this saline mudflat in turn grades outward into a dry mudflat (Eugster & Hardie, 1978). This lateral zonation, which is sometimes termed 'bulls eye' pattern, relates to the properties of the depositional environment and reflects the sedimentological, hydrological and geomorphological condition of the local pan system. In these zones different abundances of minerals dominate the top sediment layer influenced by e.g. different subsurface hydrological conditions, as well as the lithological background of the pan basin. The occurrence of evaporite minerals is mainly related to their solubility and the pan's hydrological condition. Often less soluble carbonates can be found at the edge of the pan, followed by a succession of sulphates to chlorides towards the topographically lower, central pan area (B. F. Jones, 1965; Shaw & Bryant, 2011). In most settings a small but noticeable topographic break separates the mudflat from the sloping surface of surrounding terrain that can have the form of alluvial fans in major basins (Robert G. Bryant, 1996) or sand dunes in the case of the smaller pans of the Kalahari (Lancaster, 1986).

In the semiarid to arid landscapes of southern Africa pan depressions often represent the lowest local runoff point in the weakly developed drainage systems that is occasionally blocked by sand dunes or that got disconnected by shifts of the regional tectonic. Regionally, pans dominate the morphology of parts in eastern Namibia, north-western Botswana, and northern and western South Africa (Lancaster, 1978, 1986). Occasionally, strong precipitation events lead to transient runoff in sometimes relictic or ephemeral river systems, as well as to rising groundwater that leaches the rocks of the catchment during its subsurface flow and transports solute rich brines along the gradient that often discharges into such pan depressions. In consequence, pans are filled temporally with water from several days up to a few weeks depending on the amount of precipitation and infiltration capacity of the pan sediments. Solutes which are produced and

deposited in local or regional depressions are stored within the internal drainage system to form salt pans (Goudie & Thomas, 1985). Local environmental factors such as precipitation, surface drainage, and aeolian activity can substantially influence the sedimentology and morphology of pan structures (P. D. Roy, Smykatz-Kloss, & Sinha, 2006). The most dominant process for the build-up for the evaporite rich sediments is the regular cycle of flooding and desiccation. A general model for the process dynamic of salt pans and its effect on their surface composition is provided by the saline pan cycle after (Lowenstein & Hardie, 1985) (**Figure 1**).

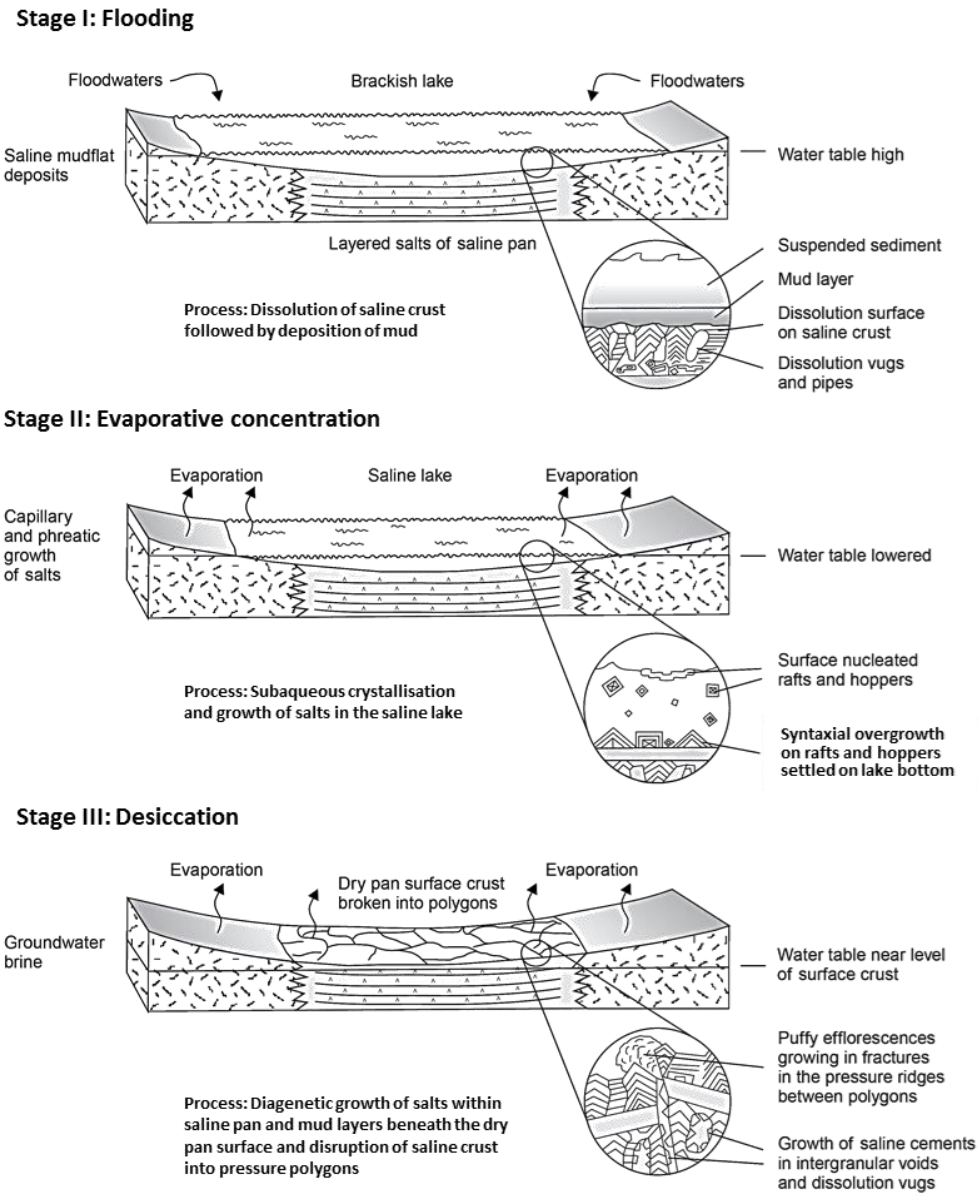

Figure 1. The saline pan cycle within a playa basin (Chivas, 2007 modified; based on Lowenstein & Hardie, 1985).

It describes that the episodic formation and dissolution of surface crust follows a cycle of flooding, evaporation, and desiccation of the playa surface (Chivas, 2007; Lowenstein & Hardie, 1985). These pan cycles are mainly driven by the surface water balance that effect evaporite sediment deposition and dissolution (Bowen et al., 2017; Warren, 2016), but are also influenced by air temperature, humidity and wind regime (Lowenstein & Hardie, 1985).

3. Aims and Objectives

The general objective of the thesis is to evaluate the potential of current and upcoming advances in optical remote sensing data to further the understanding of salt pan environments by addressing their spatial and temporal complexity. In particular, 1) the liberation of Landsat data archives over a decade ago (Wulder, Masek, Cohen, Loveland, & Woodcock, 2012) opened the way for detailed analyses of longer term and high frequency changes of the earth surface through the use of adequate methodologies that must be adapted to the high temporal data dimensionality, and 2) the emergence of hyperspectral satellites such as the Hyperion EO-1, as well as upcoming hyperspectral missions, provide analytical potential, that will be assessed in the frame of this thesis. This objective is addressed by adapting and applying state-of-the-art methods of multispectral and hyperspectral optical remote sensing data over the Omongwa salt pan test site in the southwestern Kalahari. For the test site specifically, the objective of this work aims at the better understanding of the natural process regime that drives the seasonal and inter-annual dynamic of the Omongwa salt pan. For this purpose, the spatial distribution of surface mineralogy and crust types is derived and the temporal dynamic of the pan surface crust types is assessed. Furthermore, remote sensing-based approaches are developed that allow an efficient and robust derivation of evaporite abundances in the surface sediment mixture in order to support regular monitoring using current and upcoming hyperspectral sensors. Methodologically, this research focuses on a combined approach that exploits: 1) the spectral information provided by hyperspectral remote sensing to differentiate the mineralogy of playa surface sediments, 2) the temporal coverage, monitoring capabilities and archived acquisitions of Earth Observing multispectral satellite missions to assess the surface changes and the general dynamic of such environments. A major step in this work is the assessment of the sedimentological and mineralogical variability of this specific salt pan setting and the effect on the spectral properties of the surface that are observable by spectroscopic techniques, as well as the translation of this insight to the different remote sensing scales and an assessment of the limitations of the used sensors and applied approaches.

Based on the objectives the following research questions will be addressed in this thesis:

(1) What can optical remote sensing contribute to the characterisation of the salt pan depositional environment?

(2) Can mineralogical crust components of salt pan environments be robustly mapped and quantified by current and upcoming hyperspectral sensors?

(3) What processes can be characterised by multitemporal remote sensing regarding seasonal pan changes and their link to the climatic drivers?

4. Research Framework

The research framework provides an overview of the test site (Section I-4.1), and lists the remote sensing and ground-truth data (Section I-4.2) used throughout the chapters.

4.1 Study Area

The Omongwa pan is located in east Namibia - part of the western Kalahari - approximately 260 km south-east of Windhoek (**Figure 2**). With a size of ~20 km^2 it is the largest one in a series of pans that appear to be aligned along a former branch of the Nossob River system, with a southward palaeodrainage direction (Kautz & Parada, 1976; Lancaster, 1986; Mees, 1999).

The salt pan evolved in calcareous deposits of Kalahari Group, which are exposed in the paleo river valley and in interdune space of shallow dunes (Mees, 1999; D. Thomas & Shaw, 1991; Veleen & Baker, 2009). Prominent outcrops of this calcareous material appear along the pan margins (Mees, 2002), e.g. ~1 m high scarp at the north-eastern margin of Omongwa pan. The pan is situated in the north-eastern Aranos Basin, which is part of the super-regional inland sedimentary Kalahari Basin that resulted from the uplift of the Great Escarpment in the Cretaceous. During the following Tertiary until Late Pleistocene re-occurring changes in moisture and sedimentary regime enabled both pedogenic and groundwater calcretes to cement early Kalahari deposits especially along river courses like the former Nossob tributary in the study region (Miller, 2008). The Kalahari Group is relatively thin in this region with a thickness of < 10 m (SACS 1980), which have been recognised from the cuttings of several water boreholes in the Aminuis region (JICA 2002; Miller 2008). One borehole (WW26165) directly north of the Omongwa pan revealed only 1 m of Kalahari Group deposits (JICA STUDY TEAM, 2002). They overlie more than 50 m of Pre-Kalahari basalts of the Kalkrand Formation. The surroundings landscape of the pans are generally covered by the reddish sands of the Kalahari Group (Lancaster, 1986; Miller, 2008), which are classified as Rubi-Feralic Arenosols, ARo (red, iron rich, sandy soils) according to the WRB system (FAO 2006), whereas the calcareous deposits along the paleo riverbed, in which the Omongwa pan is situated, form greyish soils that classify as Petric Calcisols, CLp (soils with secondary lime accumulation and strongly cemented layers) (Veleen & Baker, 2009).

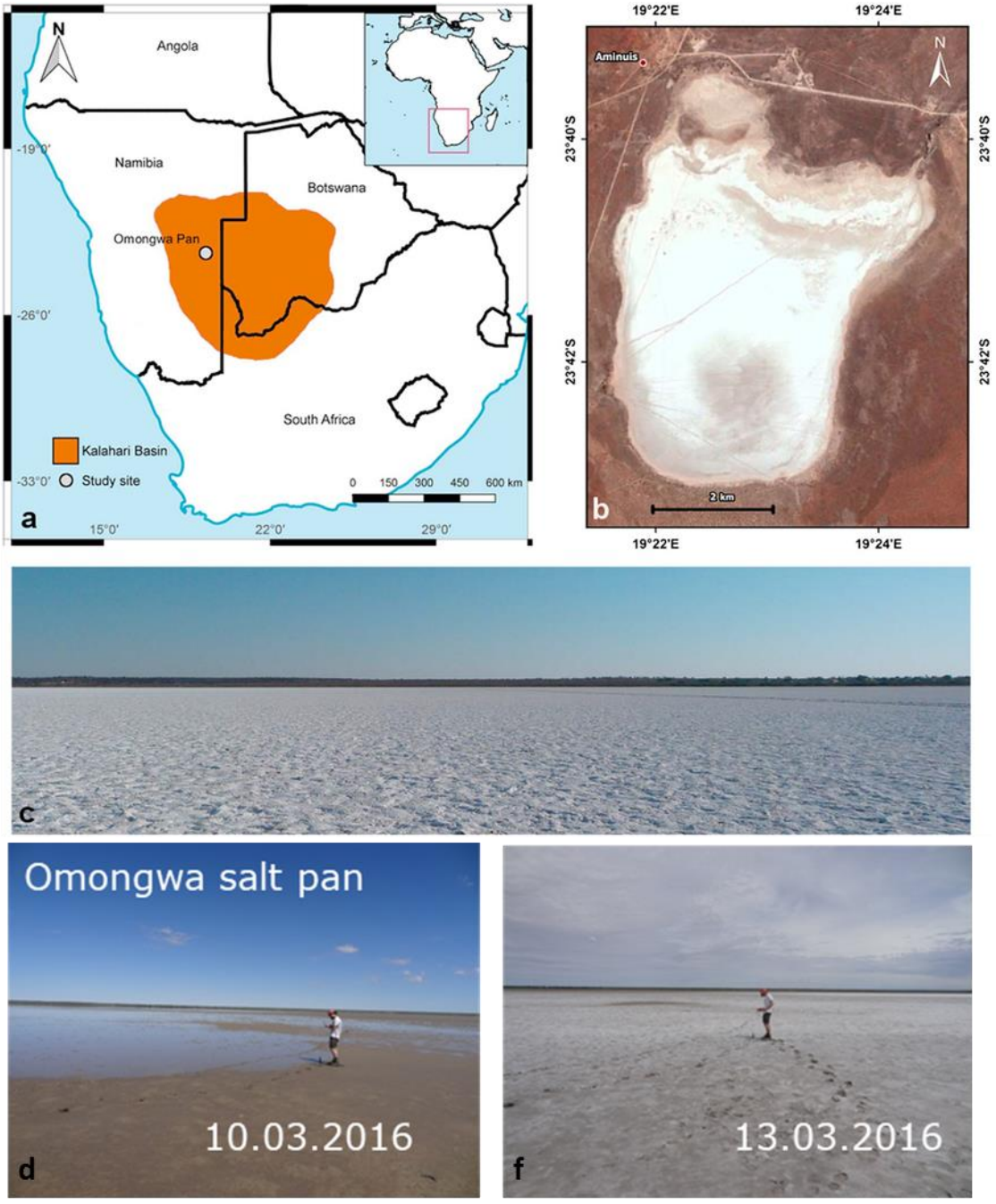

Figure 2. (a) Map of Southern Africa with the location of the study site in the western Kalahari after Genderjahn et al. (2018). (b) RGB imagery of Omongwa pan (Digital Globe, September 2013, provided by Google Inc.). (c) Picture of Omongwa pan in its desiccation state with devolved bright salt crust in October 2013. (d) Image of Omongwa pan in a partially inundated state after rainfall in March 2016 and (f) in the beginning of desiccation a few days later.

The modern surface is mostly dry throughout the year (**Figure 2c**) except when surface flooding by seasonal rainfall turn the pan or parts of into a shallow lake (**Figure 2d**). Surface runoff from the surrounding savannah landscape is very minor due to by restriction by lateral longitudinal dunes and a lunette dune at the southern pan margin (Mees, 1999). At some locations small inflows channels locally impact the pan's surface hydrology and fluvial sediment influx. Most significant is an inflow channel located at the north-eastern pan margin that forms a small drainage line that was dammed up into a small man-made water retention basin, from which the runoff occasionally drains into the pan and flows along the northern pan margin.

Climatically, the western Kalahari area is defined as hot desert climate by the Köppen–Geiger climate classification. The mean annual rainfall is 200–250 mm recorded for the period of 1982–2002 with high monthly, seasonal, and inter-annual variations and a mean annual temperature of about 21°C. On average 90% of the total precipitation occurring in the wet season from December to April (Atlas of Namibia Project, 2002). The potential evapotranspiration (ETP) is of above 3000 mm for the region a, with a maximum in July and August, where the maximum temperature can reach 48 °C. With a precipitation to potential evaporation ratio (P/ETP) of about 0.08 it is classified as arid close to hyper-arid zone. In the region, the main wind direction is north to north-west. The surface is mostly unvegetated except the north-western area that builds a small sub-basin and supports patches of halophytic vegetation that is sparse at its centre and increases in direction of the pan margin. The mostly unconsolidated material of the salt pan surface provides ideal conditions for aeolian activity. In general, salt playa surfaces experience deflation during dry periods, with transport in the dominant wind direction forming dunes on the playa and at its margins (Shaw & Thomas, 1989). However, it is also possible that aeolian material (mainly in the form of dust) can be brought into the basin from elsewhere. As such, playa basins can also be defined as open aeolian systems.

4.2 Data Basis

A multi-spatial, multitemporal, and spectral scale approach was used to address the research questions. A unique data set of spaceborne multispectral time-series data and hyperspectral ground-based, airborne, spaceborne and simulated spaceborne data at fine to coarse spatial resolution have been combined with sedimentological and mineralogical ground truth data acquired at different seasons throughout three field campaigns (**Figure 3** and **Table 1.** Remote Sensing Database.).

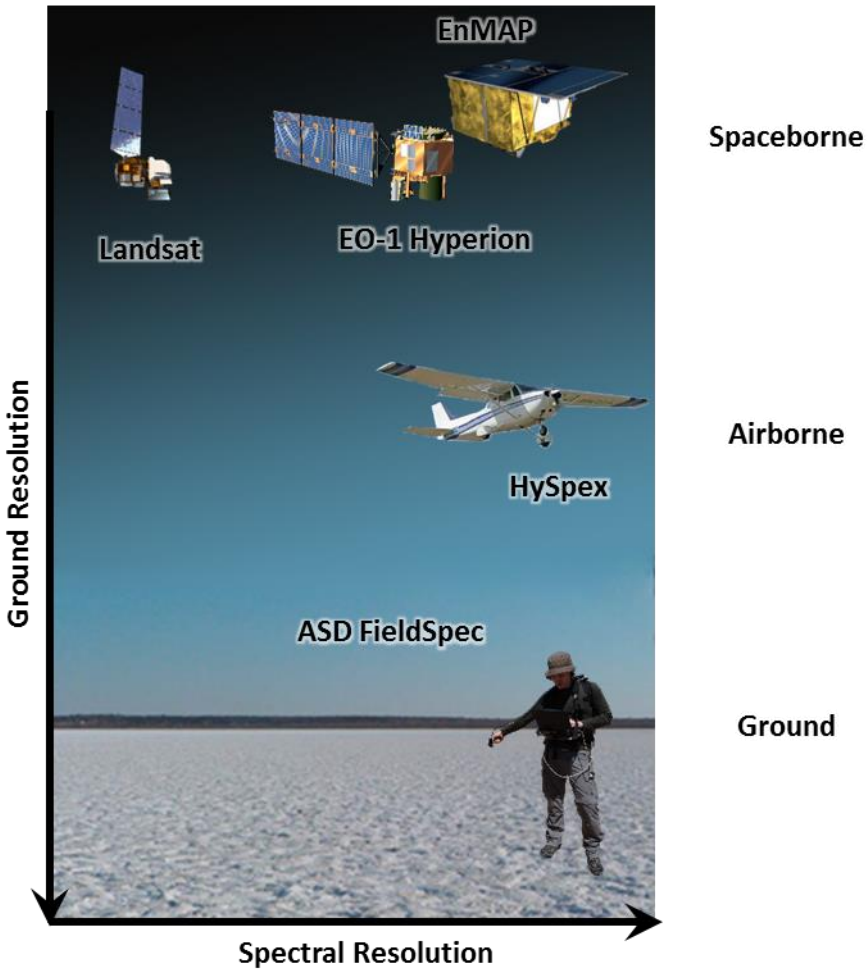

Figure 3. Schematic of the multi-scale data basis of the thesis and remote sensing devices used.

In-situ and Laboratory Spectral Data

In-situ reflectance measurements and surface sampling of the test site took place during three field campaigns in October 2014, June 2015 and March 2016, which respectively represent the end and beginning of the dry season, as well as the end of the wet season. Field spectra of untouched surfaces were collected along transects into the pan and for sites of interest representative for the variability of surface conditions and sediment mixtures using an ASD (Analytical Spectral Devices) FieldSpec 3 point spectroradiometer, covering the VNIR-SWIR spectral range with 3 to 10 nm spectral resolution resampled to sampling interval of 1 nm (ASD Inc., 2015).

Mineralogical Ground-truth Data

During three field campaigns a total of 49 samples of top surface curst have been collected (see **Figure 4**). Mineralogical characterization of the field samples was carried out using a PANalytical Empyrean powder X-ray diffractometer (XRD) with a theta-theta-goniometer, Cu-Kα radiation (λ = 0.15418 nm), automatic divergent and anti-scatter slits and a PIXcel3D detector. Diffraction data were recorded from 4.5° to 85° 2Θ with a step-size of 0.0131 and a step time of 60 s. The generator settings were 40 kV and 40 mA. All samples were crushed and powdered to a grain size of <62 micron. These samples were used for the qualitative and quantitative mineral analysis. A few samples were also powdered to <10 micron, but no strong differences in intensities were observed. The qualitative phase composition was determined using the software DIFFRAC.EVA (Bruker), and the quantitative mineralogical composition of the samples (in weight %) was calculated using a Rietveld based method implemented in the program AutoQuan (GE SEIFERT; Taut, Kleeberg, and Bergmann 1998).

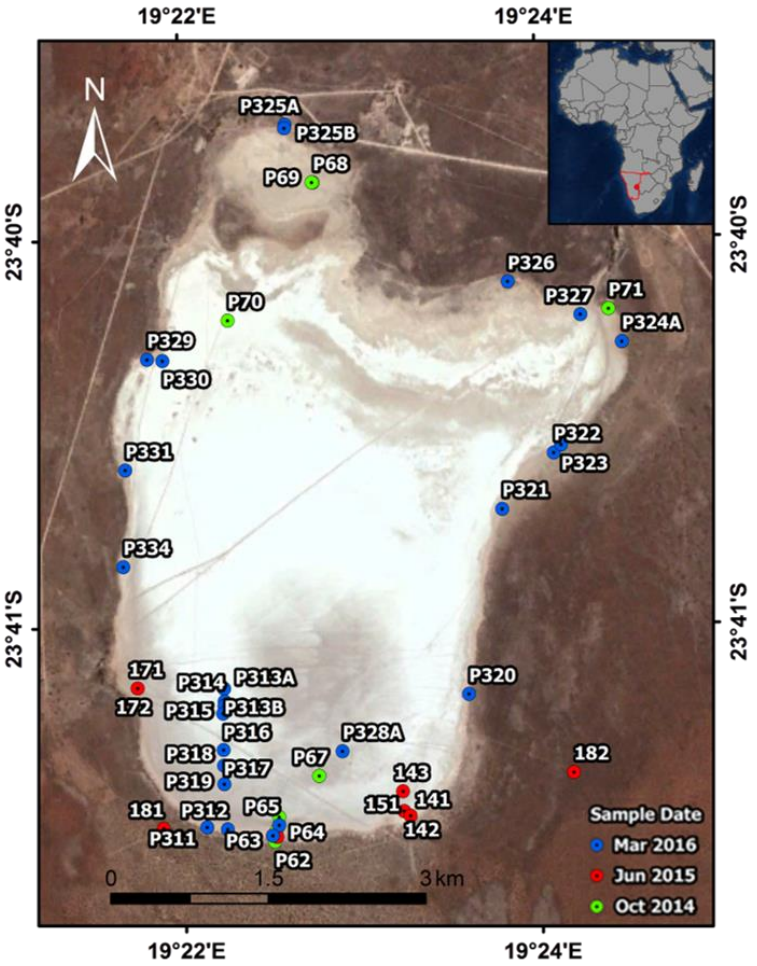

Figure 4. Locations of field surface samples (Basemap source: DigitalGlobe RGB image, September 2013, provided by Google Inc. (Mountain View, CA, USA)).

Table 1. Remote Sensing Database.

Sensor	GSD	No. of Bands	Time	Images	Provider
Landsat TM	30	7	1984-2015	98	USGS
Landsat ETM+	30	8	1999-2003	16	USGS
Landsat OLI	30	11	2013-2017	77	USGS
Airborne HySpex	2.4	416	06.06.2015	1	Dimap/GFZ
Spaceborne Hyperion	30	198	07.09.2014	1	USGS
Spaceborne EnMAP (simulated)	30	242	06.06.2015	1	GFZ

*Ground Sampling Distance

Spaceborne Landsat Multispectral Imagery

For the long-term multitemporal surface dynamic analysis of chapter II all available, cloud free Landsat images of the study area at World Reference System-2 path/row 176/76 were acquired through the USGS EarthExplorer data portal (http://earthexplorer.usgs.gov/). The time series covers the last 3 decades (1984-2015) and is composed of imagery from three different satellite and sensor generations of the Landsat Mission. From a total of 146 cloud-free scenes, the majority (98 of them) originate from Landsat 5 (TM), 16 from Landsat 7 (ETM+) and 32 from Landsat 8 (OLI). The three sensors have the same spatial resolution of 30 m, but slightly different spectral coverage or even additional bands (Chander, Markham, & Helder, 2009). Only the six reflective bands (Blue, Green, Red, NIR, MIR, and SWIR) common to all sensors are used. The Landsat data were pre-processed to top of atmosphere (TOA) reflectance by the Landsat Ecosystem Disturbance Adaptive Processing System (LEDAPS) (Masek et al., 2013). For seasonal and intra seasonal analysis of chapter III all available Landsat 8 Operational Land Imager (OLI) images of the study area at World Reference System-2 path/row 176/76 were acquired through the Google Earth Engine public data catalogue (Gorelick et al., 2017) that host the extensive USGS Tier 1 and 2 Landsat Collection. The OLI sensor has seven reflective bands (Coastal Blue: 443 nm, Blue: 482 nm, Green: 562 nm, Red: 655 nm, NIR: 865 nm, SWIR I: 1609 nm, SWIR II: 2201 nm) at a spatial resolution of 30 m (USGS, 2016). The time-series covers ~4.5 years (04/2013-10/2017) with a temporal resolution of 16 days. From the total 94 scenes 17 had to be excluded due to cloud cover over the salt pan.

Airborne HySpex Hyperspectral Imagery

The airborne datasets used in chapter III were obtained at an altitude of 2850 m above ground level over the Omongwa pan on the 6th June 2015 during a GFZ/DIMAP airborne campaign (http://dimap-spectral.com/). The hyperspectral data have been acquired using two HySpex cameras (Norsk Elektro Optikk) in nine flightlines with alternating SE/NW heading under blue sky conditions at 10:30-12:00 UTC with a sun elevation angle of 40-45° and sun azimuth angle of -10° to 20°. The NEO HySpex system consists of two push-broom hyperspectral cameras (VNIR-1600 operating over the 0.4-1.0-µm and SWIR-320m-e operating over 1.0-2.5 µm range) with a total of 416 wavebands and a spectral resolution of 3.7 nm (VNIR-1600) and 6.0 nm (SWIR-320m-e) (Norsk Elektro Optikk, 2017). The original ground sampling distance (GSD) of the image captured was 1.2 m for the VNIR spectrometer and 4.4 m for the SWIR-320m-e camera with a field of view expander.

Spaceborne Hyperion Hyperspectral Imagery

The EO-1 Hyperion hyperspectral image used in chapter I and II has been acquired on the 7th September 2014 at 07:34 UTC with a sun azimuth of 63° and a sun elevation of 36°. The

Hyperion sensor covers the VNIR and SWIR spectral region (400-2500 nm) with 198 calibrated bands of ~10 nm width at a spatial resolution of 30 m. The spatial extent is 7.5 km wide 105 km long. The signal-to-noise ratio (SNR) is specified as ~140:1 to 190:1 for the VNIR and 96:1 - 38:1 for the SWIR detector (Pearlman et al., 2003).

Simulated EnMAP Hyperspectral Imagery

For the comparison of current and upcoming hyperspectral spaceborne sensors in chapter III EnMAP hyperspectral imagery were simulated using the EnMAP End-to-End Simulation tool (EeteS). EeteS has been developed by the GFZ as part of the scientific preparatory program to provide a complete and accurate simulation of image generation, calibration, and the processing chain (Segl et al., 2012). EeteS simulation was applied on the preprocessed airborne HySpex mosaic and provides simulated imagery comparable to the expected data quality of the EnMAP reflectance product (Level-2A) at 30 m resolution. The EnMAP sensor consists of a dual-spectrometer instrument measuring in 242 spectral bands between 420 and 2450 nm with a spectral sampling distance varying between 5 and 12 nm (Guanter et al., 2015). It has a measured signal-to-noise ratio of 400:1 in the visible and near-infrared and 180:1 in the shortwave-infrared parts of the spectrum that is considered in the EeteS sensor model (Segl et al., 2012).

5. Thesis Structure and Author Contribution

This thesis contains an introduction (Chapter I), three main chapters representing three manuscripts (Chapter II-IV), and an overall synthesis and discussion (Chapter V). Chapter II and III are original publications that have been published in peer-reviewed and ISI listed scientific journals and the tried (Chapter IV) has been submitted to a peer-reviewed and ISI listed scientific journals and is currently awaiting review. All work represents stand-alone independent research. There is some overlapping general information between publications particular in the description of the study area, introductory and methods part as all work was conducted at the same test site and spectroscopic methods, e.g. field reflectance measurements and laboratory analysis were applied throughout this research.

Chapter II - Analyses of Recent Sediment Surface Dynamic of a Namibian Kalahari Salt Pan Based on Multitemporal Landsat and Hyperspectral Hyperion Data

Authors: Robert Milewski, Sabine Chabrillat and Robert Behling

Remote Sensing, 2017, 9(2), 170. https://doi.org/10.3390/rs9020170

This first published manuscript presents a spatial comprehensive study of the surface mineralogy of the Omongwa salt pan using hyperspectral EO-1 Hyperion data combined with the assessment of the long-term surface dynamic covering the last 30 years since 1984 by exploiting the rich data archive of the multispectral satellites of the Landsat-series. This information combined with the morphology of pan setting is used for interpretation of the pan's depositional environments. R. Milewski developed the overall idea and approach supported by S. Chabrillat. R. Milewski conducted the fieldwork, image processing and analysis, generation of figures and tables, and wrote the manuscript. R. Behling contributed to the methodological programming and adaptation of the IR-MAD as well as fieldwork. S. Chabrillat contributed to data interpretation and manuscript review.

Chapter III - Assessment of the 1.75 µm Absorption Feature for Gypsum Estimation Using Laboratory, Air- and Spaceborne Hyperspectral Sensors

Authors: Robert Milewski, Sabine Chabrillat, Maximillian Brell, Anja M. Schleicher and Luis Guanter

International Journal of Applied Earth Observation and Geoinformation, 2019, 77, 69–83. https://doi.org/10.1016/j.jag.2018.12.012

This second published manuscript presents an assessment of the capability of hyperspectral sensors at laboratory, airborne and spaceborne scale for the quantification of the mineralogical fraction in the salt pan surface sediments using the example of the gypsum mineral and proposes a robust and transferable approach in support of regular monitoring using current and upcoming satellite data.

R. Milewski developed the overall idea and approach supported by S. Chabrillat. R. Milewski conducted the field and laboratory work, the image processing and statistical analysis, generation of figures and tables, and wrote the manuscript. A. M. Schleicher guided the mineralogical sample analysis and its interpretation. M. Brell contributed to the geometric and spectral processing of the airborne data. S. Chabrillat and L. Guanter contributed to data interpretation and manuscript review.

Chapter IV - Analyses of Namibian Seasonal Salt Pan Crust Dynamics and Climatic Drivers Using Landsat 8 Time-Series and Ground Data

Authors: Robert Milewski, Sabine Chabrillat, Bodo Bookhagen

Remote Sensing, 2020, 12(3), 474. https://doi.org/10.3390/rs12030474

The third published manuscript, examines temporally dense seasonal and inter-annual surface dynamic of the test site using well established multispectral data of the Landsat OLI sensor that cover three major wet-dry cycles and provides an assessment of climatic parameters, such as the pan's moisture regime and aeolian activity that may drive the observed surface changes. R. Milewski developed the overall idea and approach supported by S. Chabrillat. R. Milewski conducted processing of time-series data, generation of figures and tables, and wrote the manuscript. S. Chabrillat and B. Bookhagen contributed to data interpretation and manuscript review.

Chapter II - Analyses of Recent Sediment Surface Dynamic of a Namibian Kalahari Salt Pan Based on Multitemporal Landsat and Hyperspectral Hyperion Data

This is the accepted version after peer review (Postprint) of the following article:

Milewski, R., Chabrillat, S., & Behling, R. (2017). Analyses of Recent Sediment Surface Dynamic of a Namibian Kalahari Salt Pan Based on Multitemporal Landsat and Hyperspectral Hyperion Data. Remote Sensing, 9(2), 170. https://doi.org/10.3390/rs9020170

Received: 27 July 2016; Accepted: 15 February 2017; Published: 18 February 2017

Abstract

This study combines spaceborne multitemporal and hyperspectral data to analyse the spatial distribution of surface evaporite minerals and changes in a semi-arid depositional environment associated with episodic flooding events, the Omongwa salt pan (Kalahari, Namibia). The dynamic of the surface crust is evaluated by a change-detection approach using the Iterative-reweighted Multivariate Alteration Detection (IR-MAD) based on the Landsat archive imagery from 1984 to 2015. The results show that the salt pan is a highly dynamic and heterogeneous landform. A change gradient is observed from very stable pan border to a highly dynamic central pan. On the basis of hyperspectral EO-1 Hyperion images, the current distribution of surface evaporite minerals is characterized using Spectral Mixture Analysis (SMA). Assessment of field and image endmembers revealed that the pan surface can be categorized into three major crust types based on diagnostic absorption features and mineralogical ground truth data. The mineralogical crust types are related to different zones of surface change as well as pan morphology that influences brine flow during the pan inundation and desiccation cycles. This combined information is used to spatially map depositional environments where the more dynamic halite crust concentrates in lower areas although stable gypsum and calcite/sepiolite crusts appear in higher elevated areas.

1. Introduction

Natural salt pan environments, also known as salt flats or playas, are some of the most geomorphological dynamic environments on Earth (Millington et al., 1989; Shaw & Bryant, 2011). According to (Neal, 1975), there are approximately 50,000 salt pans on Earth. Although the area of individual salt pans is small, mostly less than a few square kilometres, except for prominent examples such as Salar de Uyuni (Bolivia) or Etosha pan (Namibia), the study of salt pan is important because of increasing population, agricultural demand and the hydrology of these dry regions becoming greatly stressed (Rosen, 1994). Salt pans are also one of the biggest sources of mineral dust emission in arid regions (Prospero et al., 2002; Washington, Todd, Middleton, & Goudie, 2003) especially in the southern Africa Kalahari desert (Botswana, Namibia, Republic South Africa) (Vickery, Eckardt, & Bryant, 2013) and the specific salt pan mineralogy influences the susceptibility for dust emission (Buck, King, & Etyemezian, 2011; Nield et al., 2015; Reynolds et al., 2007). For continued advances in understanding dust sources a spatially and temporally detailed assessment of their surface sediments is necessary (Katra & Lancaster, 2008). Salt pans are also a potential significant carbon stock in the Kalahari environment (A. D. Thomas, Dougill, Elliott, & Mairs, 2014) and the dynamic of salt pan surfaces is of great importance for the understanding of the carbon

cycle and carbon fluxes of a pan systems. Furthermore, the sensitive interrelation between regional changes in climate patterns and tectonic activity within continents is often record in the pan sedimentary deposit, and insights on current surface processes are needed for a proper interpretation of paleoenvironmental conditions (Robert G. Bryant, 1996).

The harsh nature (Drake, 1995) and limited accessibility of salt pan environments makes them hard to study by conventional field mapping. This problem is exacerbated by ephemeral nature of salt pan evaporite minerals that is caused by sedimentological processes occurring at the surface as well as changes of the brine composition and the associated sequence of minerals one can expect to form in episodic dry-wet-dry cycles. The saline pan cycle described by e.g. Lowenstein and Hardie (Lowenstein & Hardie, 1985) provides a conceptual model of pan process dynamic and its effect on the pan deposits and associated evaporite mineralogy. In this model, the stages of salt pan cycles are described beginning at the desiccation stage (dry saline pan), followed by the flooding stage (brackish pan), then by the evaporative concentration stage (saline pan) and finally the return to the first status, the desiccation stage (dry saline pan). The ephemeral nature of salt pan evaporite minerals also emphasises the need for multitemporal observations (Drake, 1995; Shaw & Bryant, 2011). Over the last decades a limited number of studies have applied remote sensing techniques to study salt pan evaporite minerals and were able to provide spatial information on pan surfaces in terms of evaporite mineral discrimination supported by field observations. Most of them rely on traditional optical multi-spectral satellite sensors (Alanazi & Ghrefat, 2013; Robert G. Bryant, 1996; Chapman et al., 1989; J. Li, Menenti, Mousivand, & Luthi, 2014; Millington et al., 1989; White & Eckardt, 2006) that often do not provide the necessary spectral resolution to cover the spectral complexity of evaporite mineral assemblages on salt pan surfaces (Hubbard & Crowley, 2005) and only provide a mono-temporal assessment. In comparison analysis based on advanced hyperspectral imagery, also named imaging spectroscopy, are more sensitive for the identification and quantification of a wider range of evaporite minerals (Robert G. Bryant, 1996; Kodikara et al., 2012), and usually achieve higher modelling results (Hubbard & Crowley, 2005). EO-1 Hyperion is the first hyperspectral satellite that operates across the full solar- reflective spectrum with nominal spectral coverage form 0.4 µm – 2.5 µm and 10 µnm spectral response functions (R. O. Green, Pavri, & Chrien, 2003). Although the applications of Hyperion imagery is limited by the sensor's relatively low signal-to-noise ratio (Alanazi & Ghrefat, 2013; Thome, Biggar, & Wisniewski, 2003), spectral mapping results with Hyperion data compare reasonably well with results obtained from airborne hyperspectral sensors, including Hyperspectral Mapper (HyMap) (Anna Dutkiewicz, Lewis, & Ostendorf, 2008) and Airborne Visible/Infrared Imaging Spectrometer (AVIRIS) (J. K. Crowley,

Hubbard, & Mars, 2003; F. A. Kruse, Boardman, & Huntington, 2003). Nevertheless, the availability of hyperspectral data, spaceborne or airborne, is very limited, which prevents time-series analyses of salt pan surfaces.

In this context, this paper is looking at the potential of modern remote sensing analyses for the study of the surface processes and dynamics of salt pans. This study combines both the potential of hyperspectral EO-1 Hyperion satellite data for the identification and mapping of major salt crust types and the potential of freely available 30 years Landsat time-series archives evaluating the temporal stability of the pan surface, linked with accurate elevation information from LIDAR data. The Omongwa salt pan in Namibian Kalahari, one of the largest and most studied salt pans in its region, is known for episodic flooding events and ongoing formation of evaporates minerals at the surface (Mees, 1999; Mees & Van Ranst, 2011). The Omongwa salt pan is taken as the object of investigation in this paper, as representing other extended saline pan bodies in arid regions of the world that could be similarly studied with newly available remote sensing data. The pan's spatial extend allows it to be complete covered by current spaceborne hyperspectral datasets (Hyperion) and therefore presents a suitable opportunity to test the potential of such datasets on a regionally important site with coherent coverage. The focus of the paper is placed on the development of the relationships between evaporite mineral mapping, time-series based surface dynamic and pan morphology to differentiate depositional environment of the investigated salt pan. State-of-the-art methodological tools in optical remote sensing for change detection analyses based on multitemporal Landsat data and for surface spectral mapping based on hyperspectral imagery are used in order to deepen our knowledge and understanding of the surface processes in the Omongwa pan.

2. Study Area

The Omongwa pan is located in eastern Namibia near Aminuis, ~260 km south-east of Windhoek (**Figure 5**). With a size of ~20 km^2 it is the largest one in a series of pans that appear to be aligned along a former branch of the Nossob River system, with a southward paleodrainage direction (Kautz & Parada, 1976; Lancaster, 1986; Mees, 1999). The climate in the Aminuis region is hot and semi-arid. It classifies as BWh according to the Köppen scheme (Köppen & Geiger, 1930) with average annual temperature and yearly precipitation of 19.8 °C and 200-250 mm respectively. The rainfall is highly seasonal with 90% of the total precipitation occurring in the wet season from December to April. The inter-annual precipitation variation is very high, resulting in occasional draught years with down to ~40% of the average amount (Atlas of Namibia Project, 2002). The salt is very flat with

a mean elevation of ~1200 m above sea level. The surrounding Kalahari landscape is characterized by an undulating linear dune system typically in a NW-SE direction (as shaped by the prevailing winds) with elevation magnitudes of ~1-3 m between dune crest and interdune valley. South of the pan a lunette dune rises up to ~50 m above the pan floor level.

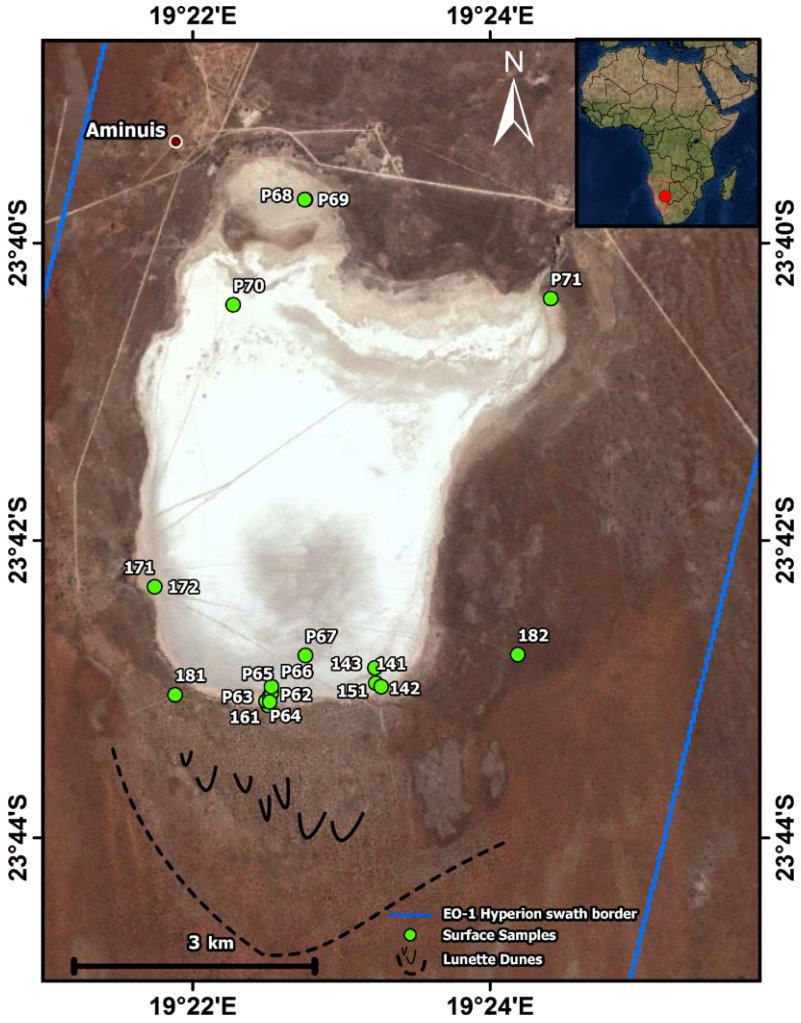

Figure 5. Location and overview of the Omongwa salt pan showing surface sample location, position of lunette dunes and extent of EO-1 Hyperion image (Basemap source: DigitalGlobe RGB image, Sep 2013, provided by Google Inc.).

The pan evolved in calcareous deposits of Kalahari Group which are exposed in the paleo river valley and in interdune space of shallow dunes (Mees, 1999; D. Thomas & Shaw, 1991; Veleen & Baker, 2009). Along these paleo river courses, Early Kalahari deposits were cemented by pedogenic and groundwater calcretes driven by re-occurring changes in moisture and sedimentary regime during the Tertiary until the Late Pleistocene (Miller, 2008). Prominent outcrops of calcareous material appear along the pan margins (Mees, 2002), e.g., ~1 m high scarp at the north-eastern margin of

Omongwa pan. Detailed mineralogical information of the pan deposits are known from a diagonal sampling survey from the SW to NE of Omongwa pan conducted by F. Mees (Mees, 1999) in 1991 and 1992. The upper lithological unit (top ~50 cm) of the pan deposits are a mainly sand-sized detrital grains with varying contents in halite (>30%), gypsum (5-40%) and calcite (10-20%) mixed with the clay and mica minerals sepiolite, muscovite, and smectite. The lower units have evaporite-filled cracks in the upper part (vadose zone) and generally increase in calcite content with depth until the calcareous mudstone bedrock is met in up to 3.5 m below the surface (Mees, 1999). It is further noted that the mineralogy of the pan is sensitive to changes of the hydrological conditions. The point based mineralogical description together with the analysis of the general pan environment is very helpful for the evaluation of the remote sensing based mapping of the surface mineralogy as it provides a baseline for the interpretation of this study. In general, the Kalahari Group is relatively thin in this region with a thickness of < 10 m (SACS (The South African Committee for Stratigraphy), 1980), which has been recognised from the cuttings of several water boreholes in the Aminuis region (JICA STUDY TEAM, 2002; Miller, 2008). One borehole (WW26165) directly north of the Omongwa pan revealed only 1 m of Kalahari Group deposits (JICA STUDY TEAM, 2002). They overlie more than 50 m of Pre-Kalahari basalts of the Kalkrand Formation. The surroundings landscape of the pans are generally covered by the reddish sands of the Kalahari Group (Lancaster, 1986; Miller, 2008), which are classified as Rubi-Feralic Arenosols, ARo (red, iron rich, sandy soils) according to the WRB system (FAO (Food and Agriculture Organization of the United Nations), 2006), whereas the calcareous deposits along the paleo riverbed form greyish soils that classify as Petric Calcisols, CLp (soils with secondary lime accumulation and strongly cemented layers) (Veleen & Baker, 2009).

The pan lacks significant surface inflow, as surface runoff is minimized by the high infiltration rates of the Kalahari sands and topographically limited to by distance of the next dune crest. The hydrogeological situation of the study region is very complex due to the occurrence of several pre-Kalahari normal faults as well as rapid facies changes in the Kalahari Group deposits (Miller, 2008; Stone & Edmunds, 2012). Borehole data near Aminuis suggest that the groundwater level is reached below the Kalahari Group deposits between 13-43 m in the Pre-Kalahari basalt layers (JICA STUDY TEAM, 2002). However, the calcareous mudstone of the Omongwa pan is likely to support a locally perched groundwater tables above the regional aquifer due to its low permeability. This is supported by the observations of fluctuating groundwater levels of 25-150 cm between the wet and the dry season 1991-1992 (Mees, 1999) as well as temporally formation of shallow open waterholes fed by groundwater discharge (Lancaster, 1986).

3. Materials and Methods

3.1. Field and Laboratory Analysis

Two field campaigns for surface characterisation and sampling took place in October 2014 and June 2015, which represent the end and beginning of the dry season respectively. Prior to both visits small precipitation events of <5 mm led to slight moist conditions in the central part of the Omongwa pan (Namibian Ministries of Agriculture, Basic Education and Health, office Aminuis, 2015), which limited the accessibility to the most outer ~500 m of the pan, and lead to a sample size of 17 surface samples.

Fieldwork consisted of acquisition of surface samples and field reflectance spectroscopy measurements along transects into the pan and for sites of interest representative for the variability of surface conditions and presumed sediment mixtures of the pan (see **Figure 5**). Sampling was performed in homogeneous areas collecting the top surface crust (<2 cm). These samples were composed of 5 to 10 sub-samples collected at random locations within a 5 m wide square around the centre point for each site of interest. Prior to sampling, field spectra of the untouched surfaces were collected at the selected locations using an ASD (Analytical Spectral Devices) FieldSpec 3 point spectroradiometer, covering the VNIR-SWIR spectral range (ASD Inc., 2015). Per site of interest, 5 spectra were acquired at nadir configuration from 1 m height with a ~25 cm target radius from the centre of each location. The measurements were calibrated to a barium-sulphate white reference standard to determine relative reflectance, and were subsequently corrected for detector offset and averaged for higher signal-to-noise ratio. All spectra and centre of sampling location were geolocated using the Global Positioning System (GPS).

Geochemical and VNIR-SWIR spectral analyses of surface samples were conducted in the laboratory including the parameters mineralogy, grain size, pH, and conductivity. Initial sample preparation comprised of sub-sampling and drying at 105 °C. After the removal of organic material and carbonates using 10% H_2O_2 and 17% HCl respectively, sample texture was determined by a combination of wet-sieving (particles >63 µm) and sedimentation (particles <63 µm) following (German Institute for Standardization, 2002). Electrical conductivity was measured in a 1:5 ratio with bi-distilled water after (German Institute for Standardization, 1997) and pH in a 0.01M $CaCl_2$ suspension after (German Institute for Standardization, 2002). The sub-samples used for powder X-ray diffraction (XRD) were crushed in a vibrating disc mill to a particle size <63 µm. Powder samples were measured using Cu-Kα radiation. Diffractograms were recorded from 5° to 85° 2θ using a

PANalytical Empyrean diffractometer. Results were analysed using the software Bruker EVA for mineral identification and Seifert AUTOQUAN for quantification. Laboratory spectral characterisation was performed with the ASD FieldSpec 3 point spectroradiometer under controlled light illumination simulating spaceborne observations (sensor nadir viewing, light source azimuth 35°). Finally, two spectral libraries of Omongwa sediment surfaces were created associated with field and laboratory optical signatures.

3.2. Remote Sensing Change Detection Analyses

The multitemporal analysis uses all available, cloud free Landsat images of the study area at World Reference System-2 path/row 176/76 acquired through the USGS EarthExplorer data portal (http://earthexplorer.usgs.gov/). The time series covers the last 3 decades (1984-2015) and is composed of imagery from three different satellite and sensor generations of the Landsat Mission. From a total of 146 cloud-free scenes, the majority (98 of them) originate from Landsat 5 (TM), 16 from Landsat 7 (ETM+) and 32 from Landsat 8 (OLI). The three sensors have the same spatial resolution of 30 m, but slightly different spectral coverage or even additional bands (Chander et al., 2009). Only the six reflective bands (Blue, Green, Red, NIR, MIR, and SWIR) common to all sensors are used. On average the data series is composed of 5 images per year, but the distribution is highly irregular. Data gaps occur during the mid 1980es and from late 2011 to early 2013 when Landsat 5 data were discontinued and Landsat 8 was not yet operative. Between 2003-2013 data availability further decreased to 1-4 scenes/year after the failure of the Scan Line Corrector (SLC) of the Landsat 7 ETM+ sensor, which makes the data unusable for change-detection approaches such as in this study.

The Landsat data were pre-processed to top of atmosphere (TOA) reflectance by the Landsat Ecosystem Disturbance Adaptive Processing System (LEDAPS) (Masek et al., 2013) including the conversion of calibrated Digital Numbers (DNs) to absolute units of at-sensor spectral radiance and reduction of in scene-to-scene variability due to different solar/sensor geometry and Sun/Earth distance. Top of atmosphere (TOA) reflectance is used to normalize scene radiances differences due to variations in solar illumination, sensor viewing geometry, and seasonality (Earth-Sun distance). Surface reflectance products for all optical bands are also available (Masek et al., 2006; USGS, 2015). However the atmospheric correction applied by LEDAP follows the popular dense vegetation (DDV) approach (Kaufman et al., 1997), which is known to provide limited accuracy in arid environments (Maiersperger et al., 2013), as it depends on finding sufficient and evenly distributed dark objects like dense vegetation or water bodies that are completely absent in the

study area. Because of the lack of such surfaces in the study area, it is unclear on which basis the estimation of the aerosol properties is performed and it is likely that an artificial bias is introduced to the data instead of a correction. Furthermore, the provisional AOT estimation for the Landsat 8 OLI images is based on coarse (0.05 deg) MODIS data (Vermote, Justice, Claverie, & Franch, n.d.), which can lead to tilling artefacts in the processed image (USGS, 2015) that were also identified on images of the Omongwa pan. Due to the current limitations in corrections to surface reflectance especially applied in arid areas, TOA reflectance is used in this paper for the change detection analyses. An adapted procedure for change detection analysis is used that limits the atmospheric influence.

In a first step, to restrict the change detection analyses to the dynamic of the pan surface deposits in dry state, Landsat images related to pan flooded state have to be excluded from the dataset. For this purpose, Xu's Normalized Differenced Water Index (NDWI) (Xu, 2006), a band ratio using the green and mid-infrared (MIR) band, is derived from the Landsat record. This adaption of the NDWI is sensitive even to shallow water bodies (W. Li et al., 2013). A conservative threshold of 0.5 was selected to filter scenes featuring surface water. This restriction robustly excludes images that show an inundated pan surface, as well as scenes which have significant moisture in the top layer of pan deposits. Exactly how the selected NDWI threshold relates to the water content of the surface sediments is scene dependent and cannot be profoundly estimated from the remote sensing image. A total of 30 scenes were water covered or in very wet surface conditions and discarded for further analyses.

On the remaining 116 Landsat images a change detection analysis is applied. The described discontinuities and gaps of the Landsat record restrict popular approaches of time series analyses based on temporal trajectories like the Breaks For Additive Season and Trend (BFAST) (Verbesselt, Hyndman, Newnham, & Culvenor, 2010) and Reversed Ordered Cusum (ROC) (Pesaran & Timmermann, 2002) procedures. Discontinuous datasets do not meet the need of many curve-fitting time series methods to establish a "stable" reference model from historical data (DeVries, Verbesselt, Kooistra, & Herold, 2015), e.g. 16-day time series over 2 years (Verbesselt, Zeileis, & Herold, 2012). Accordingly, a temporally more robust approach of bi-temporal change detection, the Iterative-reweighted Multivariate Alteration Detection (IR-MAD) developed by A.A. Nielsen (Allan Aasbjerg Nielsen, 2007) is selected. The IR-MAD has been successfully used for different applications and sensors, e.g., to detect changes caused by floods from coarse AVHRR imagery (Liao, Zhu, & Gong, 2000), mining activity (Mezned, Dkhala, & Abdeljaouad, 2015; Pathak, 2014)

and forest disturbance from Landsat data (Colditz, Llamas, Gebhardt, Wehrmann, & Equihua, 2015), as well as earthquakes from high resolution imagery of GF-1/PMS and GeoEye-1 (Hoja, Krauss, & Reinartz, 2013; Y. Ma et al., 2016). The core idea of MAD is to find maximum differences between two images by removing correlations between them as much as possible (L. Zhang, Liao, Yang, & Lin, 2007). The MAD algorithm transforms two sets of multivariate observations (in this case two multispectral satellite images covering the same geographical area acquired at different points in time) into a difference between two linear combinations of the original variables explaining maximal change (i.e. the difference explaining maximal variance) in all variables (wavelength) simultaneously (Allan Aasbjerg Nielsen, 1994). IR-MAD is an improvement of the MAD approach. In order to increase the detection of observations, whose status over time is uncertain, weights are put on difficult observations that exhibit small change according to their change probability in the previous run. In each iteration a better no-change background is identified, achieving a better separability between the change and no-change classes (Allan Aasbjerg Nielsen, 2007).

The IR-MAD can be classified as a bi-temporal linear data transformation type of change detection (Coppin, Jonckheere, Nackaerts, Muys, & Lambin, 2004). This change-detection approach is most suitable to observe the type of changes that can be expected in the salt pan environment, due to the following properties: 1) It can detect modifications (changes in crust composition) and not only discrete conversions (crust type A to crust type B); 2) it is sensible to progressive as well as abrupt changes (slow deflation of particles, loss and build-up of new crust after inundation); 3) it can work with the temporal sampling rates of the observations (irregular, data gaps) (Coppin et al., 2004). A further advantage over most other change detection methods is that IR-MAD is invariant to linear transformations of the original image intensities (Allan A. Nielsen, Conradsen, & Simpson, 1998; Allan Aasbjerg Nielsen, 2007). The method is robust to differences in atmospheric conditions or sensor calibrations at two acquisition times, which greatly reduces the requirements on radiometric correction or normalization (L. Zhang et al., 2007). This is an important advantage for this study because it limits the atmospheric influence on the change detection result when using TOA reflectance data. A general constraint to bi-temporal change detection methods such as the IR-MAD is the loss of data due to a number of contaminations or errors like SLC-off data gaps (DeVries et al., 2015) and cloud cover (Ju & Roy, 2008). Although well-performing correction approaches have been proposed for data gaps with information derived from neighbouring pixels (Aghamohamadnia & Abedini, 2014) or even other sensors (Chen, Zhu, Vogelmann, Gao, & Jin, 2011), interpolation or the inclusion of extraneous data can introduce additional errors

(Alexandridis et al., 2013; Bédard, Reichert, Dobbins, & Trépanier, 2008). For this, SLC-off acquisitions as well as clouded scenes are discarded.

In this study, the python implementation of IR-MAD by (Canty, 2014) is used to which some modifications were made that allow for batch processing of the Landsat image stack. For the Omongwa pan subset a total of 115 bi-temporal change maps are produced. The IR-MAD processing always converged to a no-change background before hitting the defined maximum of 50 iterations. Besides providing the basis for the no-change probability calculation, the sum of squared, standardized MAD variates, also called $\chi 2$ image (Canty & Nielsen, 2012) is used as a general measure of change of the pan surface similar to (Hoja et al., 2013; Liang, Hoja, Schmitt, & Stilla, 2011; Allan Aasbjerg Nielsen, Hecheltjen, Thonfeld, Canty, & others, 2010). From each bi-temporal IR-MAD analysis of the Landsat dataset, the final $\chi 2$ image is used to derive aggregated change over the time-series to differentiate dynamic pan areas from radiometrically more stable regions.

3.3. Remote Sensing Surface Characterisation

3.1.1. EO-1 Hyperion mineralogical mapping

One EO-1 Hyperion hyperspectral image is used in this study. It has been acquired on the 7th September 2014 at 07:34 UTC with a sun azimuth of 63° and a sun elevation of 36°. The Hyperion sensor covers the VNIR and SWIR spectral region (400-2500 nm) with 198 calibrated bands of ~10 nm width at a spatial resolution of 30 m (Pearlman et al., 2003) similar to the Landsat imagery. The spatial extent is 7.5 km wide 105 km long. The signal-to-noise ratio (SNR) is specified as ~140:1 to 190:1 for the VNIR and 96:1 - 38:1 for the SWIR detector (Pearlman et al., 2003).

An automated pre-processing chain for EO-1 Hyperion data developed by (Rogass, Guanter, et al., 2014) is used that provides georeferenced surface reflectance data. The L1 radiance data (L1R), L1T radiance terrain corrected data, acquisition parameters from the metadata and an ASTER 30 m DEM, freely distributed through the USGS EarthExplorer data portal (http://earthexplorer.usgs.gov/) are used. Data processing includes rescaling to radiance, removal of the spectrally overlapping bands, bad band detection, reductions for dead pixel and erroneous detector columns, as well as corrections for intra-band spatial shifts, keystone, erroneous co-registration, radiometric miscalibration. Part of the processing chain is the atmospheric correction as proposed in (Guanter, Richter, & Kaufmann, 2009; Guanter, Segl, et al., 2009) originally designed for the EnMAP Box (van der Linden et al., 2015). It includes a complex Radiative Transfer Modelling (RTM), Aerosol Optical Thickness (AOT), Columnar Water Vapour (CWV) retrieval as well as spectral Smile and adjacency correction (Rogass, Guanter, et al., 2014). Georeferencing is performed via

GCP (Ground Control Point) selection and first-order transformation using ENVI 5.3 (Harris Geospatial Solutions, 2015) between the corrected image and the orthorectified L1T Hyperion image. The geometrical transformation is applied at the end on the results to prevent resampling effects on the spectral analyses. The pre-processing chain was used previously for geological applications e.g. by Mielke et al. (Mielke, Muedi, et al., 2016; Mielke, Rogass, Boesche, Segl, & Altenberger, 2016) proving that it can deal with the sensor limited quality and still delivers reflectance data that are adequate for mineralogical identification analyses.

Spectral mixture analyses (SMA) (Adams, Smith, & Johnson, 1986; J.W. Boardman & Kruse, 1994) implemented in ENVI 5.3 (Harris Geospatial Solutions, 2015) is used to determine the mineralogy of the pan surface based on the EO-1 Hyperion image. SMA is a physically-based model that transforms radiance or reflectance values to physical variables that are linked to the subpixel abundances of surface components within each pixel (Joseph W. Boardman, 1993; Tompkins, 1997). SMA proved useful specifically for the mapping of salt and gypsum surfaces (Robert G. Bryant, 1996; Shrestha, Margate, van der Meer, & Anh, 2005), but also in a wide range of other applications, like vegetation e.g. (Garcia-Haro, Gilabert, & Melia, 1996), mineralogical and lithological mapping e.g. (Chabrillat, Pinet, Ceuleneer, Johnson, & Mustard, 2000; F. Kruse, Lefkoff, & Dietz, 1993), soil degradation assessment (Metternicht & Fermont, 1998). The SMA analysis assumes a linear mixing of the scene constituents in the sensor field-of-view and is particularly adapted to arid landscapes with aerial mixing. In SMA, the reflectance of a pixel is determined by the sum of the reflectance of each material within a pixel multiplied by its fractional cover. Most crucial for the quality of an unmixing model is the selection of endmembers that account for the spectral variability of the data, while remaining physically meaningful (Dennison & Roberts, 2003; Tompkins, 1997). Instead of focusing on specific absorption features, SMA uses the whole reflectance of the VNIR-SWIR selected endmember to map subpixel abundances. This is especially helpful in the study of salt affected surfaces that often do not show diagnostic absorption features outside of the known water (vapour) absorption region (Farifteh, van der Meer, van der Meijde, & Atzberger, 2008). The inherent dimensionality of the EO-1 Hyperion data is examined via minimum noise fraction transformation (A. A. Green, Berman, Switzer, & Craig, 1988) and image endmembers are extracted from the edges of the data cloud. Following (Joseph W. Boardman, Kruse, & Green, 1995), candidate endmembers extracted from the image are further redefined in minimum noise fraction transformed space to assign the purest and least noisy pixel spectra as final endmembers. In order to focus on the fractional cover of different mineralogical crust types and to reduce the

spectral variability of the data set, the areas outside the Omongwa pan are excluded from the image for SMA analyses using an albedo threshold.

3.1.2. LiDAR digital surface model

Airborne Light Detection and Ranging (LiDAR) data were acquired with a Riegl LMS-Q780 at an altitude of 2850 m above ground level over the Omongwa pan on June 6 2015 during a GFZ/DIMAP airborne campaign (http://dimap-spectral.com/). The pan surface was partly moist, but not flooded at the time of overflight. A total of nine flightlines were recorded with a swath width of ~3 km and an overlap of approximately 60% and an average point density of 2.1 pts/m². Fundamental accuracy assessed through calibration flights showed ±10 cm vertical and ±15 cm horizontal accuracy within a of 95% confidence level. For the topography of the Omongwa pan a 1 m grid Digital Surface Model (DSM) was generated from the first return LiDAR mass point data by converting the points to a Triangulated Irregular Network (TIN) surface mesh and the TIN to a regular raster grid with Natural Nearest Neighbour interpolation using the program Terrasolid TerraScan. Values are given in meters above sea level (a.s.l.)

4. Results

4.1. Field and Laboratory Analysis

Field observations showed highly heterogeneous pan environments that could be grouped into three different crust types (**Figure 6a-c**): a) Halite (NaCl) is present over the whole pan surface in variable amounts, and is identifiable as bright white surfaces, with puffy structure and blisters; b) The sulphate mineral gypsum ($CaSO_4 \cdot 2H_2O$) is a major constituted of the crust at the pan margin and appear as a smoother and darker surface; c) Carbonate crust appears in the form of some sediment accumulation mixed with salt composition, linked with carbonate outcrops at the border of the pan (**Figure 6e**). Surface roughness as well as the general brightness are very variable between the crust types and are also affected by anthropogenic disturbances (**Figure 6f**). In general, the pan surface is bare of any vegetation with the exception of the most northern part that is sparsely covered with patches bushes that increase in density in the direction of the pan margin (**Figure 6d**).

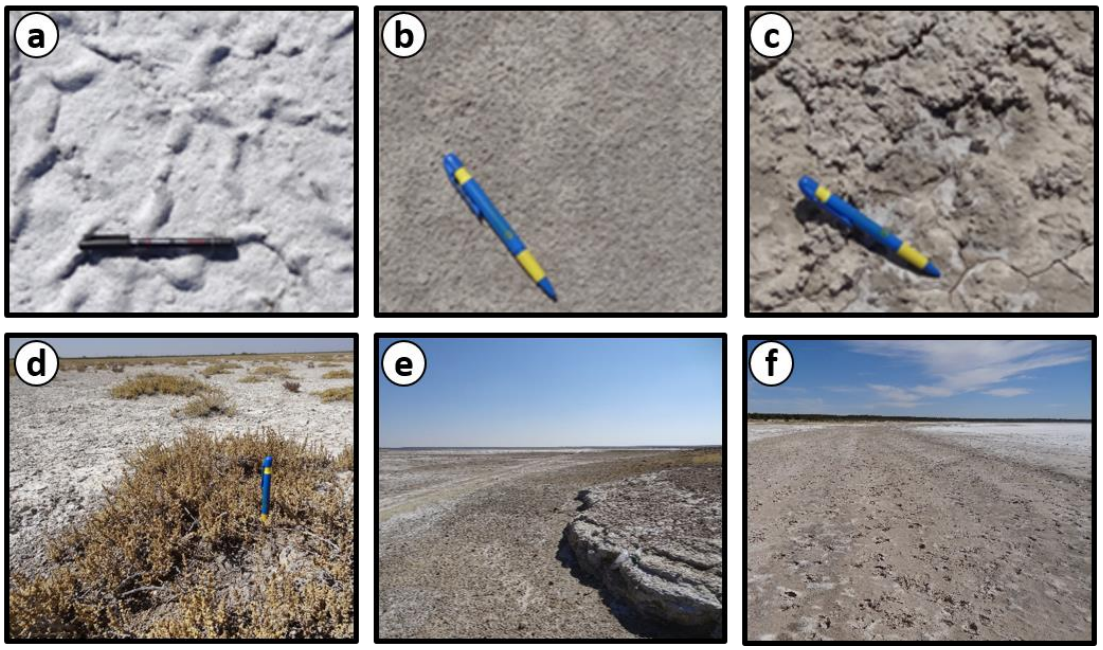

Figure 6. Different types of pan surfaces composed of detrital and evaporite mineral mixtures and environments of the Omongwa pan in October 2014 and June 2015. (a) bright efflorescent halite crust, puffy salt blisters; (b) smooth structure gypsum surface; (c) rough carbonate / sepiolite crust; d) vegetated patches of the north-eastern pan area; (e) ~50 cm high outcrop of the carbonatic mudstone bedrock, northern pan margin; (f) surface disturbed by cattle treading at the southern pan margin; length of pen used for scale ~13 cm.

From field spectral measurements as well as laboratory geochemical analysis, the major mineralogical components in the salt pan sediments could be identified and related to the different crust types. **Figure 7** shows the field spectra for the three representative crusts types and Table 1 the geochemical results of all samples. According to the XRD analysis, Omongwa halite field endmember (sample 141, **Figure 6a**) is almost pure halite (NaCl) (94%) mixed with small amounts of gypsum ($CaSO_4 \cdot 2H_2O$) (3%). The associated field spectrum shows a constant high reflectance level in the VNIR with almost no slope, which is typical for pure halite (Hunt et al., 1971) or halite rich salt pan sediments (Anna Dutkiewicz et al., 2008). The absorption and general lower reflectance level of the Omongwa halite field spectrum compared to standard laboratory halite powder spectral reflectance from the USGS spectral library (Clark et al., 2007) originates from the partially moist conditions at the time of field spectral acquisition as well as from the intermixture with some gypsum at that location. Laboratory spectral measurements of this sample after air drying for several days result in reflectance level up to 70% in the VNIR, close to reference halite spectral characteristics. The field spectrum of the second crust type (sample P65, **Figure 6b**) is characterised

by strong absorption features in the SWIR at ~1750 nm and ~2200 nm as well as the unique triplet absorption around 1500 nm, which are characteristic for gypsum spectral properties (F. M. Howari, Goodell, & Miyamoto, 2002; Hunt et al., 1971; Khayamim et al., 2015). The XRD analysis also confirms the high gypsum content (83%) mixed with some halite. The third surface crust type (sample P68, **Figure 6c**) is dominated by high calcite ($CaCO_3$) content (45%), mixed with the clay mineral sepiolite ($Mg_4Si_6O_{15}(OH)_2 \cdot 6H_2O$) (16%). The associated field spectrum shows a strong absorption feature at ~2340 µm. Both calcite and sepiolite have their characteristic absorption features at this wavelength (Hunt et al., 1971).

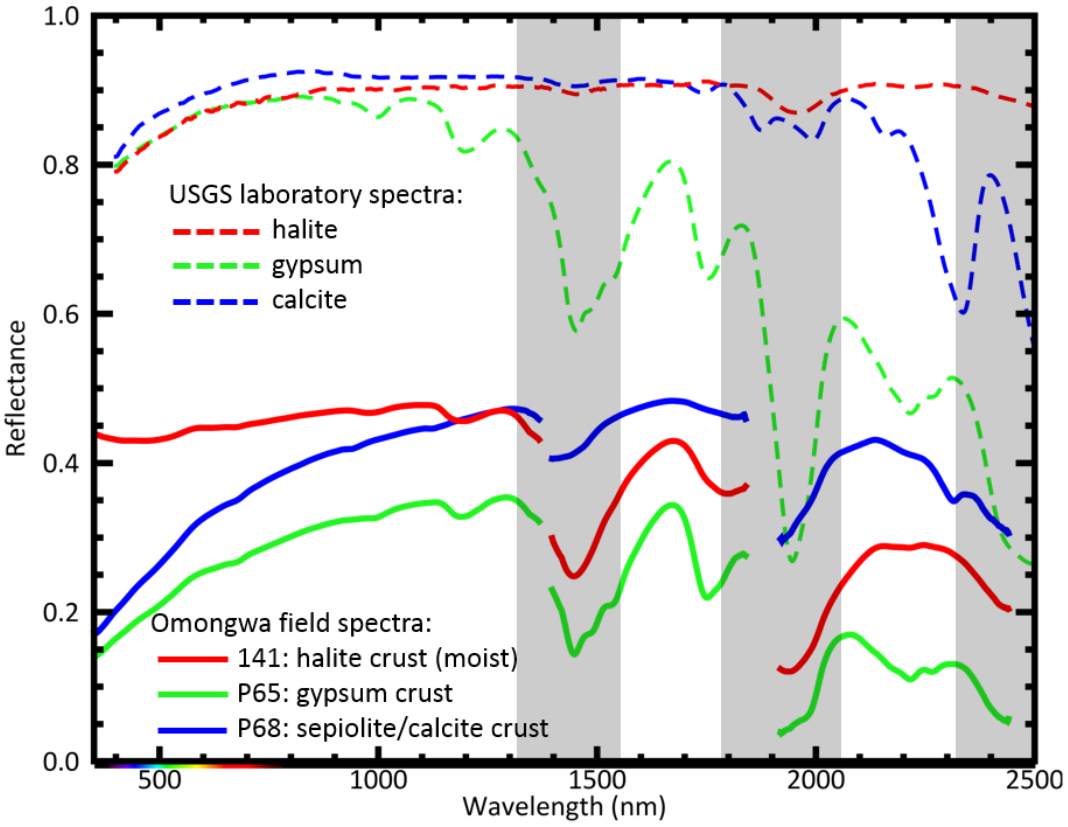

Figure 7. Field spectra (straight lines) of the three characteristic pan surface types of the Omongwa pan associated with halite crust (sample 141), gypsum crust (sample P65), and sepiolite/calcite crust (sample P68) and USGS laboratory spectra (Clark et al., 2007) (dotted lines) of the main minerals. The grey overlay indicates wavelength regions of atmospheric absorption and sensor lower signal-to-noise ratio not useable for Hyperion analyses.

Table 2. Properties of Omongwa surface samples. Location of field samples are shown in **Figure 5**.

Label	Mineralogy (bulk XRD) semi-quantitative estimates [%]						pH	EC [dS/m]	Grain size [%]		
	quartz	halite	gypsum	calcite	sepiolite	dolomite			clay	silt	sand
P62	79	-	21	-	-	-	7.9	1.9	2	3	95
P63	19	5	75	-	-	-	8.6	17.6	1	4	95
P64	17	36	47	-	-	-	-	-	-	-	-
P65	3	14	83	-	-	-	8.5	42.3	5	4	91
P66	13	41	44	-	1	-	-	-	-	-	-
P67	3	46	45	-	5	-	8.4	80.7	4	40	56
P68	36	3	-	45	16	-	8.3	10.8	4	37	59
P69	28	15	-	41	15	-	8.7	36.5	8	39	53
P70	32	16	26	15	11	-	8.6	33.7	2	34	64
P71	26	7	-	47	6	14	-	-	-	-	-
141	1	94	3	-	-	-	-	-	-	-	-
142	63	9	15	7	5	-	8.8	23.4	7	24	69
143	1	52	38	4	5	-	8.3	129.7	6	73	21
151	64	21	7	9	-	-	9.1	48.2	2	17	81
161	14	3	79	3	-	-	8.2	11.6	2	11	88
171	27	50	17	4	-	-	9.0	98.0	4	24	72
172	41	17	33	8	-	1	8.7	42.3	2	16	82

4.2. EO1 Hyperion Analyses

Four images endmembers are extracted from the Hyperion imagery and shown in **Figure 8**. Overall, the main spectral properties of the first three extracted endmembers are similar to the field spectra of the different crust types. However, some differences are observed due to variable sensor characteristics and surface conditions. The extracted Hyperion endmember spectrum (EM 1 in Figure 4) for halite crust has a high reflectance level around 70% and significant spectral slope in the shorter wavelength compared to the field halite spectrum. The higher general albedo can be attributed to the dry conditions of the central pan surface at the time of Hyperion image acquisition, whereas the differences in the shorter wavelength could result from a higher proportion of silicates exposed due to the larger Hyperion pixel or that are present in the central part of the pan not accessible during the field campaigns. In the image endmember that corresponds to the gypsum crust (EM 2 in **Figure 8**) the triplet absorption around 1500 nm visible in the gypsum field spectrum is within the water vapour atmospheric absorption bands and cannot be observed, but the other absorption features at ~1750 nm and ~2200 nm are well defined. The characteristic absorption feature of the calcite and sepiolite crust at ~2340 nm exceeds the usable spectral range of the Hyperion scene. However, the left slope and shoulder of the absorption feature can still be identified at ~2300 nm in the image endmember (EM 3 in **Figure 8**). Because the observed

absorption at ~2300 nm can originate from both minerals, we refer this endmember as calcite/sepiolite. In the surface reference samples analysed by XRD the minerals mostly occur together with ~2-3x higher share of calcite. Besides the spectrally and mineralogically well-defined endmembers of halite, gypsum, and calcite/sepiolite, a fourth image endmember had to be added to account for the spectral variability within the scene. This endmember is associated with disturbed halite crust of lower reflectance (EM 4 in **Figure 8**).

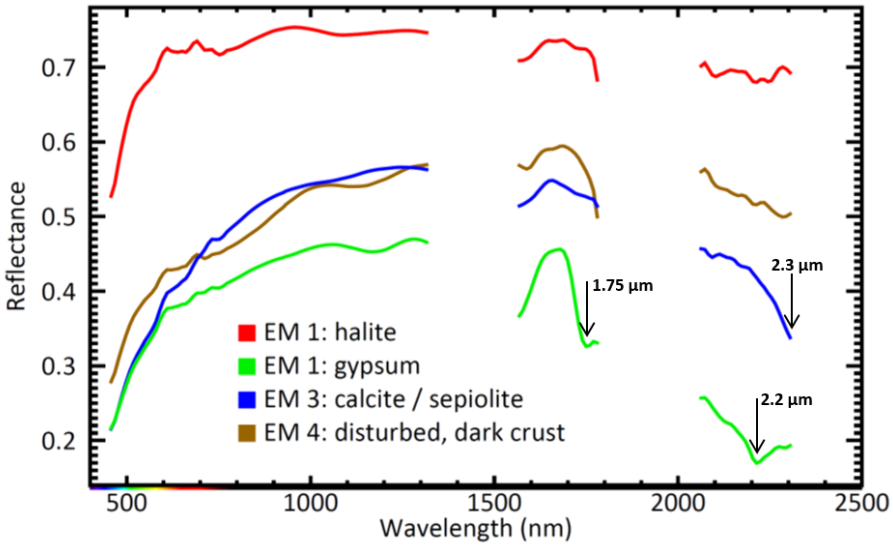

Figure 8. Hyperion endmember image spectra used for the spectral mixing analysis. Arrows indicate the position of diagnostic absorption features for gypsum and calcite / sepiolite crust.

Figure 9 show the SMA result of the identified pan crust components based on the Hyperion image. Each abundance map represents the fraction of the surface type on the Omongwa salt pan in a) bright halite crust, b) gypsum crust, c) calcite and sepiolite crust, d) disturbed, dark crust. In general, all endmembers have their abundances well mapped with no component exceeding 1. The accuracy of the unmixing model is assessed through the root mean squared error (**Figure 9e**). The RMSE image shows that the overall pan surface is well explained with the linear mixture of the four selected endmembers except for higher RMSE areas at 1) the North-East corner and western pan border associated with heavy cattle disturbances, 2) the mainly diagonal SW-NE lines crossing the pan, which are used as driving shortcuts across the pan during the dry season as well as cattle path ways, and 3) the parallel, vertical stripes (~11°), associated with remaining sensor noise that were not removed through the pre-processing procedure. In general the performance of the unmixing model is very good with an overall mean RMSE of ~1% comparable to equivalent studies, e.g., (Ghosh, Kumar, & Saha, 2012) achieved an mean RMSE of ~2% using linear unmixing on Hyperion data to map salt effect soils or (Xia Zhang, Shang, Cen, Shuai, & Sun, 2014) getting the same accuracy

range for the abundances of vegetation, soil and limestone bedrock. The SMA mapping shows that more than half of the pan surface is dominated by halite crust in variable amounts (**Figure 9a**). The highest abundances are mapped in the central part and in a circular shape in the southern half of the pan, whereas the border region and the anthropogenic pathways have minimal fractions of halite crust. In most regions the distribution of gypsum crust appears to be inversely related to the halite crust. Highest gypsum composition is found at the southern pan border, in the south-central circular shape and in a ~1.5 km long stripe in the northern pan area (**Figure 9b**). The occurrence of calcite and sepiolite crust is confined to the northern part of the pan and to the pan border (**Figure 9c**) close to outcrops of the carbonatic bedrock that were observed in the field (**Figure 6e**). The disturbed, dark crust endmember (**Figure 7d**) is mainly associated with the cattle and human disturbance of the salt crust through the pathways crossing the pan and at the border regions (e.g., **Figure 6f**). In these areas the top crust is at partly removed and the subsurface material is exposed. The subsurface is usually less concentrated in evaporite minerals and more mixed with the clastic, quartz-rich material of the pan. This is reflected by the geochemical analyses of subsurface field samples 142 (halite: 9%, quartz: 63%) and 172 (halite: 17%, quartz: 41%), directly sampled under the surface crust of samples 141 (halite: 94%, quartz: 1%) and 171 (halite: 50%, quartz: 27%), respectively at a depth at a depth of ~10 cm. The sub-surface samples show decreased halite and increased quartz content compared to surface samples (Table 1). In addition to mineralogical differences, the physical properties of the salt pan surface are altered by cattle trampling, increasing the surface roughness (Baddock, Zobeck, Van Pelt, & Fredrickson, 2011), which may also cause the reflectance to decrease even at similar salt content by casting micro shadows (Metternicht & Zinck, 2003). The rougher surface crust is also likely to be more moist (Nield et al., 2016) adding to the decrease in reflectance.

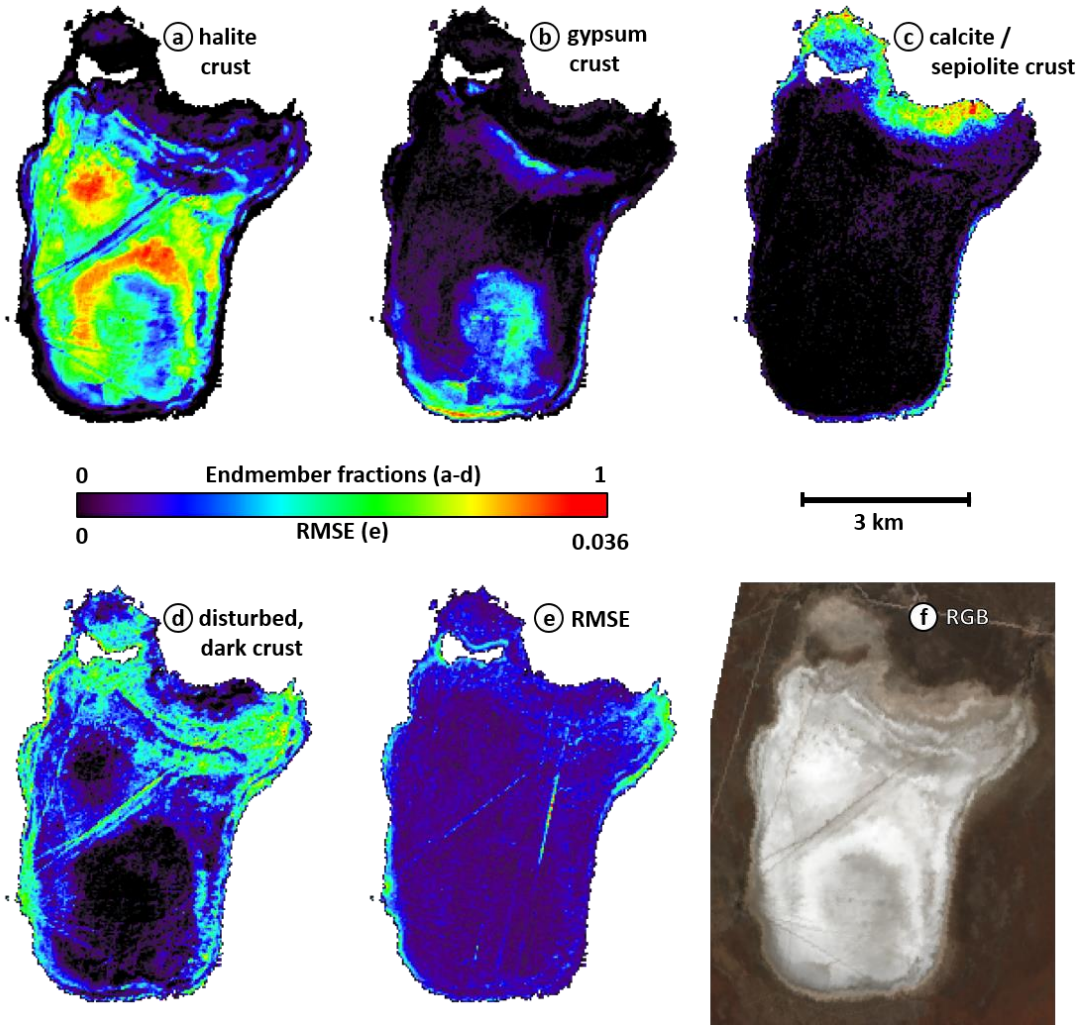

Figure 9. Hyperion mineralogical analysis: Endmember abundances and RMSE of linear spectral unmixing analysis: (a) halite, (b) gypsum, (c) calcite /sepiolite, (d) disturbed, dark crust, (e) RMSE, (f) RGB (R: 641 nm, G: 549 nm, B: 457 nm) true colour Hyperion image

4.3. Remote Sensing Change Detection Analyses

Figure 10 shows the result of the IR-MAD analysis. It represents the mean of the 115 IR-MAD $\chi 2$ images derived from the Landsat scene dry surface conditions of the period 1984-2015. The change magnitude map reveals that the salt pan is a highly dynamic and also heterogeneous landform. Compared to the changes of pan surface, the magnitude of spectral change in the surrounding Kalahari savannah is insignificant, which include the seasonal dynamic of the vegetation. Other change signals outside of the pan are of anthropogenic origin associated with housing activity in the south-west of the pan (see few pixels south of the pan in **Figure 10**) and a gravel road in the north of the pan. Within the pan, a gradient of change is determined from a very stable pan border to a highly dynamic central pan. The small northern sub-pan, where P68 and P69 are located (**Figure**

5), is very stable compared to the main pan body. The changes in the central part of the pan are very heterogeneous. Two regions of highest change (red colour in **Figure 10**) are identified located in the north of a circular area in the central southern part of the pan and a corridor in the northern part of the pan. In relation to the highest change in the pan centre, several distinctive regions of lower change can be identified. For example, straight lines crossing the pan as well as the mentioned circular shape have lower change magnitude compared to their surroundings. The largest of these lines crosses the pan centre and is associated with a pathway that connects settlements in the west and north-east of the pan.

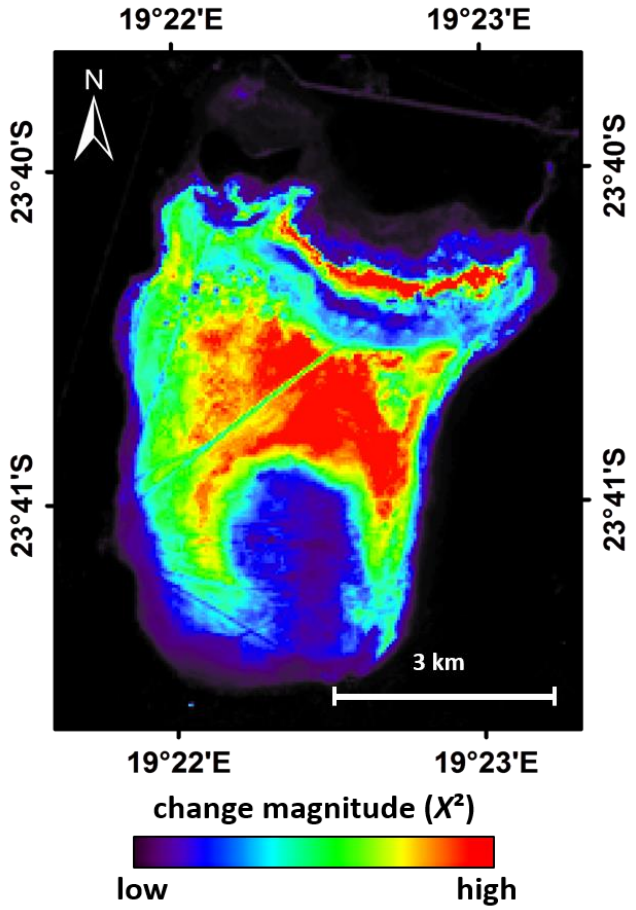

Figure 10. Landsat multitemporal analysis: Change magnitude map that represents the mean of 115 IR-MAD χ2 images (1984-2015).

5. Discussion

5.1. Pan Surface Characterisation

The combined remote sensing results over the Omongwa pan based on Landsat change detection analyses, Hyperion mineralogical identification and mapping and the LIDAR elevation model are summarized in **Figure 11**. Hyperion mineralogical identification agrees with the findings of previous studies (Mees, 1999) based on conventional point-based field sampling. The main mineralogical constituents of the top layer of the pan deposits described in (Mees, 1999), namely: quartz, halite, gypsum, calcite and sepiolite could be identified in our XRD analyses and furthermore Hyperion satellite imagery was able to provide spatial distribution of the major crust types and abundance maps over the whole pan. However, no indication of muscovite or smectite (described to occur in traces in Mees, (1999) were found in our analysed field samples nor were these minerals recognized in the spectral properties of in-situ or laboratory measurements. This discrepancy may be the result of different sampling locations or depth. In this study the top <2 cm of the pan deposits was sampled, unfortunately (Mees, 1999) does not provide spatial differentiation of the mineralogy or state the specific sampling depth, which prevents further evaluation. Another possible explanation is a change in exposed surface mineralogy. The mineralogical data published by (Mees, 1999) were sampled in 1991 and 1992. During this >20-year time frame the surface alteration e.g. by redistribution of surface particles du to surface flooding (Lowenstein & Hardie, 1985) and or wind erosion (Reynolds et al., 2007) are possible scenarios. The formation of fresh halite crust after significant rainfall and flooding events may superimpose underlying less soluble (e.g. clastic) minerals (Chivas, 2007) and hide these (minor) components from surface observations, especially in the central halite dominated, dynamic part of the salt pan. The detection of minor crust components may be also limited by the low signal-to-noise ratio of the Hyperion data (Alanazi & Ghrefat, 2013; Thome et al., 2003). However, the spectral properties of the most abundant crust components are represented in the selected endmember spectra of the generalised major crust types. **Figure 11** shows that the different areas of surface change appear to be well correlated to the crust mineralogical mapping as well as pan morphology. Areas associated with high change magnitudes are located in the central part of the pan, which is dominated by halite mineralogy and lower topographical areas. Gypsum crust is the second most abundant crust type of the Omongwa pan (**Figure 11b**). Unlike the halite crust, the gypsum area mapped with Hyperion is associated with more stable or intermediately dynamic surface regions in the multitemporal analysis (**Figure 11a**) and slightly higher topography (**Figure 11c**). Although the difference in pan height of 10-15 cm

between halite dominated and gypsum mixed crust is rather small, it seems to be enough to affect the surface mineralogy.

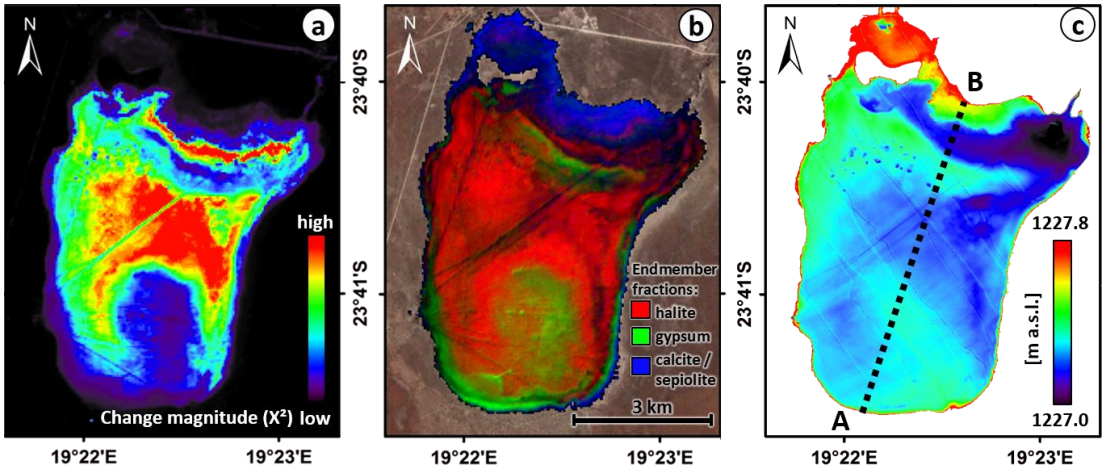

Figure 11. Omongwa pan remote sensing analysis: (a) Landsat change magnitude map (1984-2015); (b) Hyperion mineralogical map (09/2014); (c) DEM derived from LiDAR survey. A---B locates the spatial transect shown in **Figure 13**.

Figure 12 presents the relationship between endmember abundance and digital elevation model resampled to Hyperion spatial scale. For clarity not all Hyperion pixels are shown, rather a Random Stratified Sampling (RSS) pixel selection is represented. RSS is used to respect the pixel distribution over all elevations and put emphasis on the extreme elevations that represent ~33% of the total pan area. The figure shows that pan depressions (areas lower than 1227.25 m, ~18% of the total pan area) are dominated by halite crust and higher topographical positions (areas higher than 1227.4 m, ~15% of the total pan area) are dominated by gypsum crust, whereas the majority of pixels with more mixed crust abundances are present at the medium elevations.

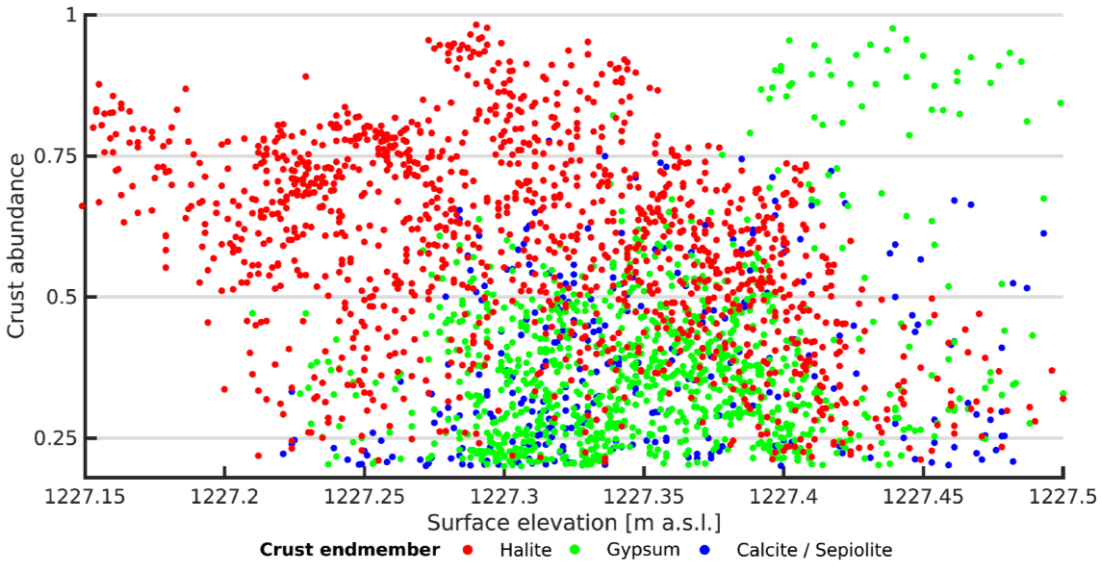

Figure 12. Relationship of pan surface elevation and crust endmember abundance.

5.2. Interpretation of Pan Surface Processes and Depositional Environment

The interpretation of the observed differences in pan surface dynamic, mineralogy and morphology based on the remote sensing findings confirms that Omongwa pan follows the conceptual model of the depositional cycle of salt pan environments given by Lowenstein & Hardie (Lowenstein & Hardie, 1985), and that this sediment dynamic can be spatially mapped with advanced remote sensing analyses such as in this paper. The conceptual model describes the reaction of pan deposits to a precipitation event. The stages of these pan cycle are: (1) desiccation stage (dry saline pan), (2) flooding stage (brackish pan), (3) evaporative concentration stage (saline pan) and the return to (1) desiccation stage (dry saline pan). Starting from the dry pan state (stage 1) ephemeral inundation events occur that cover parts or rarely even total surface area of the pan. Evaporite minerals will be dissolved by undersaturated meteoric water and redistributed over the pan mainly following the topography (stage 2). Halite is one of the less stable (more soluble) evaporite minerals and will be quickly leached into the brine and removed from the uppermost surface layer (Warren, 2016), whereas gypsum and calcite are more stable (less soluble) (Smith & Compton, 2004) and therefore are more likely to remain in the surface crust in higher abundancies, which is what we observe in the Hyperion mapping where high gypsum and calcite areas are more concentrated on the borders of the pan, which are also the most stable areas as identified in the Landsat time-series change analyses. After some time of continued evaporation, the increasingly concentrated brine will accumulate in the local depressions (stage 3). In these saline brine pools, the dissolved solutes will (re-)precipitate in reversed order of solubility. Gypsum crystals will form first in the brine pool

and halite will be the last evaporite mineral that forms on top of the other deposits (Warren, 2016) resulting in a most pure efflorescent salt crust surface layer. In summary, the increasing concentration of brine leads to a horizontal zonation of evaporite minerals ordered by solubility. Such a 'bulls eye' effect of lateral zonation of evaporite minerals from carbonates at the edge, through sulphates to chlorides in the topographically lower, central part are also observed in other salt pans (B. F. Jones, 1965; Shaw & Bryant, 2011). Influences that complicate this idealised model of evaporite mineral deposition and zonation that lead to a more complex distribution are 1) high groundwater levels during flooding events that affect the surface brine chemical composition and its saturation stage in respective to the ions of evaporite minerals (Smith & Compton, 2004), 2) strong winds can move the standing waterbody on the very low-angle salt pan (Millington et al., 1989) during the brine concentration stage (stage 3) ignoring the minimal elevation differences. Subsurface brines of the Omongwa pan that were sampled in 1991 at the end of the raining season by (Mees, 1999) were Na-K-Cl-SO_4 dominated with a total dissolved solids concentration of about 260 g/L, which basically reflect the elemental composition of the mapped surface evaporite minerals. When the diluted meteoric water mix with these groundwater brines it lowers the potential for dissolving the surface crust evaporite minerals.

The highest change magnitude in the halite crust region detected with the multitemporal remote sensing analyses correlates very well with the regular build-up of bright efflorescent halite crust described by the model of the pan depositional cycle. During each flooding-and-desiccation cycle, the surface albedo will significantly lower after a rainfall event due to (partly) dissolved halite curst and potentially from some remaining moist sediments at the surface and will increase again, when the surface has dried and the halite crust is reformed. This means, episodic flooding events are likely to be the main driver for the observed Landsat change in surface reflectance linked to crust dynamic. The reformation of a surface salt crust during the desiccation stage is typical for the wet playas type with shallow (< 5 m), fluctuating ground water table described by (Reynolds et al., 2007). In these types of salt pans capillary action in the sediments allows for continuous evaporation from shallow ground water that results in the formation of evaporite minerals in the capillary fringe zone as well as directly on the surface (Reynolds et al., 2007). This categorisation is supported by the observed evaporite filled cracks and fissures in the first 50 cm of sediments reported by (Mees, 1999) throughout vertical profiles of the Omongwa pan. These efflorescent salt crusts that form directly from evaporation at the surface are commonly very soft and fluffy and have a high potential for dust emission even under moderate winds (Buck et al., 2011). The soft consistency of the upper ~10 cm of halite rich sediments has been also observed for the Omongwa

pan (Mees, 1999). Over time theses soft surfaces have the potential to become crusted surfaces sufficiently thick to shut down all dust emission, through receding groundwater levels during the dry season or extended periods without rainfall (Reynolds et al., 2007). However, the high change magnitudes in the Landsat multitemporal analysis indicate that the halite crust is periodically dissolved and reprecipitated, thus do not support that in Omongwa long-remaining hard layered halite crusts are regularly formed.

Following the idea of (Robert Gavin Bryant, 1993), proportion maps of the mineralogical crust type can be used to classify the depositional environment of a salt pan. In this study the approach is adapted to the different geomorphological setting of the Omongwa pan (bordering calcite bedrock instead of clastic alluvial facies) and complemented by the topographic information and the change detection result. **Figure 13** shows an exemplary South-North profile of Hyperion mineralogical mapping compared with Landsat ~30 years dynamic mapping and LiDAR topography that crosses the different depositional zones of the Omongwa pan (location of the profile is giving in **Figure 11c**). Six zones with three different levels of activity are recognised. The most southern surface is dominated by high proportions of gypsum crust (40-90%) with some calcite / sepiolite crust (up to 30%) and lower gypsum content at the very beginning. This very stable gypsiferous surface represents the southern pan margin with increasing topography in direction of the lunette dune. As the profile moves north an increase in halite crust abundance (up to 70%) and a decrease in gypsum abundance (around 30%) is observed. This mixture dominated saline mud flat (Robert Gavin Bryant, 1993) is more active compared to the pan margin, but still more stable than the lower central depression of the salt pan. Further north the gypsum fraction in the surface sediment quickly declines and halite increases further. This very dynamic region dominated by high halite proportions (between 50-95%) can be interpreted as the central area of saline pan sediments (Robert G. Bryant, 1996; Lowenstein & Hardie, 1985). This is the aforementioned region where build-up of bright efflorescent halite crust alternates with more moist phases and lower surface albedo in each recurring inundation cycle. To the north the saline pan zone is bordered by a slight increase in topography (~10 cm) that results in conditions similar to the southern mud flat with lower surface dynamic and mineralogical mixture of halite, gypsum, but also northward increase of calcite / sepiolite. North of this elevated ridge position the halite fraction increases again and comparable condition to the central saline pan are met. This linear shaped depression in the north of the pan originates from a short, poorly developed channel that feeds into the depression at the north-eastern pan margin and is active during significant rainfall events (**Figure 11c**). The channel was observed to hold water for several days after a rainfall in October 2014 and June 2015. The

transect ends at the stable pan margin dominated by the calcite / sepiolite mudstone bedrock that seems to deposit into the adjacent halite dominated depression. Additionally, anthropogenic disturbance lead to modification of the original salt crust especially at the pan border, where the fresh efflorescent halite crust is removed and mineralogically more mixed material emerges from the subsurface that is less cohesive and can more easily contribute to dust emission.

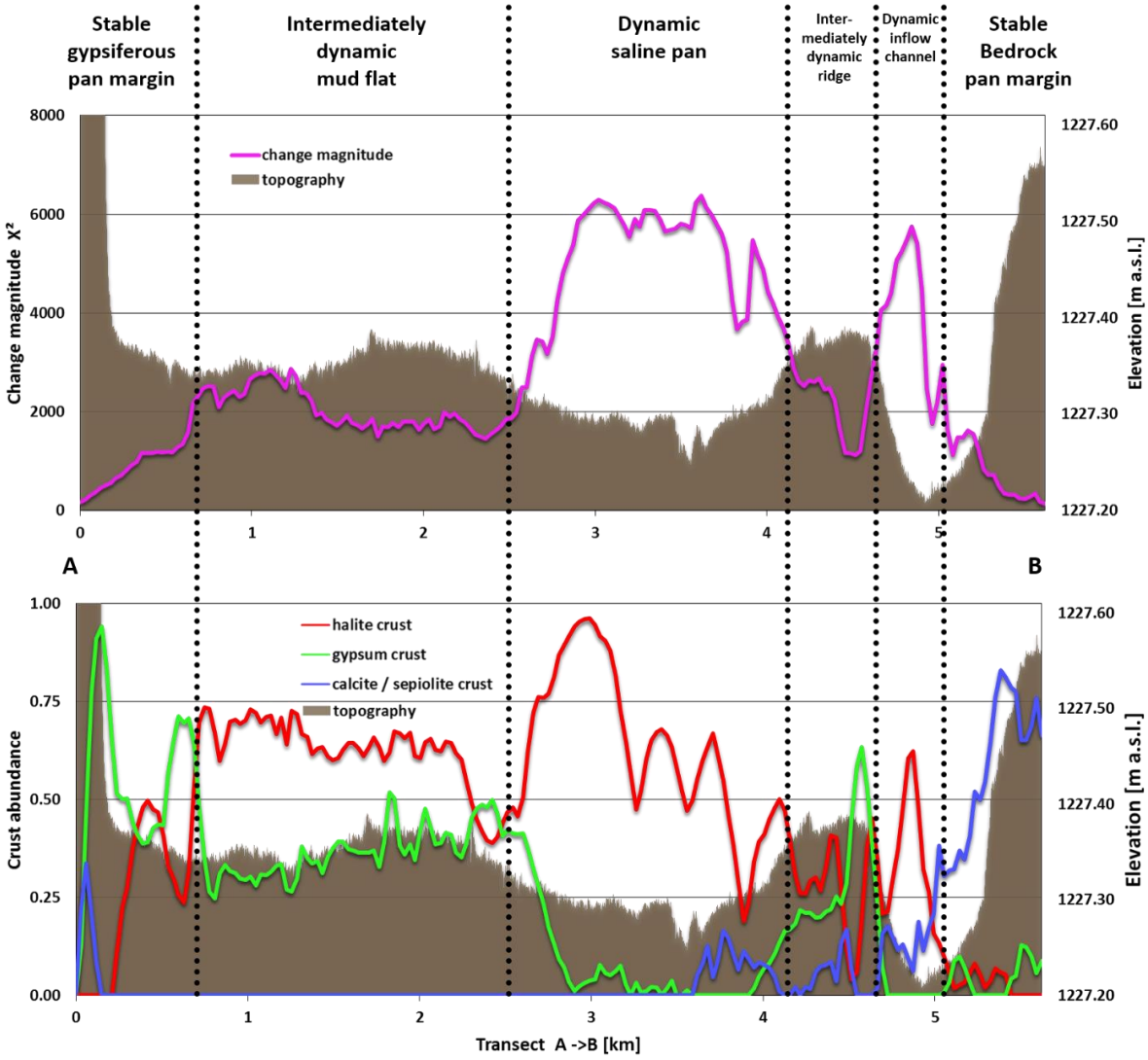

Figure 13. Spatial profile through the Omongwa salt pan (A-B, SW to NE, marked in **Figure 11c**). Pan topography, vertical exaggeration ~10^4 (filled graph) is shown with Landsat change magnitude (top), and Hyperion mineralogical abundances (bottom).

6. Conclusions

In this paper combined multitemporal and hyperspectral remote sensing analyses over the Omongwa salt pan in the Namibian Kalahari region are used to spatially differentiate and map

depositional environments within the pan that deepen our knowledge of the local surface processes. Additional field and laboratory measurements and LiDAR topographical survey support the interpretation. The results show that the major salt pan mineralogical crust types (halite, gypsum, sepiolite/calcite, disturbed dark crust) could be spatially and spectrally well differentiated by Spectral Mixture Analysis on the basis of to EO-1 Hyperion imagery. The spatial distribution patterns of the mineralogical crust types correlate well with the Landsat ~30 years change map of the pan surface derived with IR-MAD analysis. A Highly dynamic pan centre is identified that is dominated by halite crust, whereas at the more stable pan margins and the southern parts of the pan gypsum and calcite / sepiolite crusts are more common. The surface change map relates well to different susceptibility to pan inundation events according to the solubility of the evaporite minerals as described in conceptual models of the depositional cycle within salt pan environments. Whereas halite is more easily dissolved even by small precipitation events, gypsum and calcite are more likely to remain in the surface layer. Our analyses provide for the first time a deep understanding of the spatial distribution of the fresh efflorescent salt crust formation and the influence of pan morphology. The change detection map also does not support the presence of long-lasting stable halite crust but rather confirm and detail the dynamic aspect of the distribution of halite crust, due to climatic and anthropogenic influences. The study also shows that the detailed morphological information provided by the LiDAR DSM could complement the analysis of surface mineralogy and dynamic and could contribute to the classification of salt pan's depositional environment related to topographical position. While dynamic halite crust dominates most of the surface area and especially the lower regions, more stable gypsum and calcite/sepiolite crust appear to concentrate in higher areas.

The results demonstrate the potential of current advanced remote sensing optical methodologies for the improvement of our knowledge on pan surface processes. To further deepen the understanding of the pan environment and its responses to climatic events, future work should focus on high temporal monitoring of hydrological parameters like groundwater flow, precipitation and flooding events that could lead to insights into major driving factors for the observed surface change and mineralogical patterns both in the dry and in the wet seasons. Further improvement on the classification of the pan surface and its properties lies in the combination of the presented approach with RADAR based multitemporal assessments of the surface roughness. Nevertheless, in this paper with newly available Earth observation techniques the full complexity of a saline pan dynamic could be spatially described, combining mineralogical and topographical mapping with ~30 years change detection analyses. The Omongwa pan is presented as an exemplarily object of study

to test the potential of new remote sensing techniques. The approach used in this study are not pan-specific and could be well transferred and applied for the study of arid landscapes and salt pan characterisation in the region and in others arid regions of the world. The proposed framework of methods is also relevant regarding upcoming remote sensing technology. For example, regarding the planned and upcoming Earth Observation missions equipped with high quality imaging spectrometers, like the German Environmental Mapping and Analysis Program (EnMAP) mission (Guanter et al., 2015), hyperspectral analyses, such as the proposed mineralogical pan surface characterization, will become available even for extensive sites on a more regular temporal basis. A better wider characterisation of pans mineralogy would also support further studies on pan susceptibility for wind erosion and contribute to assessment of potential dust emissions.

Acknowledgments: This work was funded by the German Federal Ministry of Education and Research (BMBF) within the framework of the SPACES – “Science Partnerships for the Assessment of Complex Earth System Processes” program under the GeoArchives project – “Signals of Climate and Landscape Change preserved in Southern African Geoarchives”. Jörg Völkel and GeoArchives project partners are gratefully acknowledged for providing the opportunity to develop this work, and science discussion. Many thanks are due to Christian Mielke and Luis Guanter for their support and helpful comments with the data preprocessing, Daniel Berger for his help with the field work, and Anja Schleicher for support with the XRD analysis, as well as Hartmut Liep and Marina Ospald for the sample preparation. The authors also thank the USGS and NASA for providing Landsat and Hyperion data, especially Stuart Frye and the EO-1 Science Team for acquiring the Hyperion datasets that were used in this study.

Chapter III - Assessment of the 1.75 µm Absorption Feature for Gypsum Estimation Using Laboratory, Air- and Spaceborne Hyperspectral Sensors

This is the accepted version after peer review (Postprint) of the following article:

Milewski, R., Chabrillat, S., Brell, M., Schleicher, A. M., & Guanter, L. (2019). Assessment of the 1.75 µm absorption feature for gypsum estimation using laboratory, air- and spaceborne hyperspectral sensors. International Journal of Applied Earth Observation and Geoinformation, 77, 69–83. https://doi.org/10.1016/j.jag.2018.12.012

Received: 4 August 2017; Accepted 27 December 2018; Published: 3 January 2019

Abstract

High spectral resolution (hyperspectral) remote sensing has already demonstrated its capabilities for soil constituent mapping based on absorption feature parameters. This paper tests different parameterizations of the 1.75 µm gypsum feature for the determination of gypsum abundances, from the laboratory to remote sensing applications of recent as well as upcoming hyperspectral sensors. In particular, this study focuses on remote sensing imagery over the large body of the Omongwa pan located in the Namibian Kalahari. Four common absorption feature parameters are compared: band ratio through the introduction of the Normalized Difference Gypsum Index (NDGI), the shape-based parameters Slope, and Half-Area, and the Continuum Removed Absorption Depth (CRAD). On laboratory soil samples from the pan, CRAD and NDGI approaches perform best to determine gypsum content tested in cross validated regression models with XRD mineralogical data (R^2 = 0.84 for NDGI and R^2 = 0.86 for CARD). Subsequently the laboratory prediction functions are transferred to remote sensing imagery of spaceborne Hyperion, airborne HySpex and simulated spaceborne EnMAP sensor. Variable results were obtained depending on sensor characteristics, data quality, preprocessing and spectral parameters. Overall, the CRAD parameter in this wavelength region proved not to be robust for remote sensing applications, and the simple band ratio-based parameter, the NDGI, proved robust and is recommended for future use for the determination of gypsum content in bare soils based on remote sensing hyperspectral imagery.

1. Introduction

Soils and sediments in arid and semi-arid regions can be strongly affected by the accumulation of the evaporite mineral gypsum ($CaSO_4 \cdot H_2O$) (Herrero, Artieda, & Hudnall, 2009), which has a significant effect on soil fertility, plant development and productivity (Soil Resources, Management and Conservation Service & FAO, 1990). Gypsiferous soils can be found in abundance in wetlands or arid salt pan environments around the world, where information on content and spatial distribution of gypsum is needed for the evaluation of environmental processes, as gypsum is strongly coupled to the biogeochemical sulphur cycle (F. D. Eckardt, Drake, Goudie, White, & Viles, 2001) and relates to hydrological conditions like groundwater level, flow and the geomorphology of the region (Shaw & Bryant, 2011). Information on gypsum can also contribute to facies characterisation (Robert G. Bryant, 1996; Ghrefat & Goodell, 2011; Mees, 1999), as well as mineral exploration efforts (Bharti, Kalimuthu, & Ramakrishnan, 2015; Ferrier & Wadge, 1996). Gypsiferous soils are also reported to cause poor soil aggregation and structure (Poch & Verplancke, 1997), water retention properties (Moret-Fernández & Herrero, 2015), reduced soil pore space and water

infiltration rates (Poch, Coster, & Stoops, 1998), which often leads to low crop yields (Soil Resources, Management and Conservation Service & FAO, 1990). However such soils can be productive and managed profitably, but they need to be studied properly first (Etesami, Halajian, & Jamei, 2012). In small quantities, gypsum may even be favourable for plant growth (Alphen & Romero, 1971) and is recommended as a chemical soil amendment (Lee, Seo, Ro, & Yun, 2016), especially for reclamation of sodic soils (Qadir, Schubert, Ghafoor, & Murtaza, 2001). In contrast to traditional field and laboratory methods for the analysis of soils mineralogical constituents, optical high spectral resolution remote sensing has the capability for fast and cost-effective regular monitoring of top-soil mineralogical properties over extended areas (E. Ben-Dor et al., 2009). In contrast to many other evaporite minerals, that basically do not have diagnostic absorption features in the optical or thermal spectral range (e.g. halite), gypsum is characterized by multiple distinctive absorption features in the visible, near-infrared (VNIR) and shortwave-infrared (SWIR) spectral region (Hunt et al., 1971). These spectral properties distinguish gypsum from most other surface materials and allow to estimate its abundance in the soil mixture via reflectance spectroscopy in the laboratory as well as potentially by remote sensing through air- and spaceborne sensors.

Previous studies at laboratory scale have shown that the gypsum content of mixed samples can be reliably quantified under a controlled laboratory environment using statistical techniques like Partial Least-Squares Regression (PLSR) (Khayamim et al., 2015) or Penalized Spline Regression (PSR) (Weindorf et al., 2016). However statistical approaches like PLSR need a high amount of well-distributed calibration data that is costly and often difficult to come by for remote and extensive areas regularly covered by remote sensing data. The resulting regression models or other, generalist machine learning approaches are also highly adapted to the local and present conditions, which limits their spatial and temporal transferability. These limitations are especially meaningful, when models are transferred to other regions, in which different soil mineral components, such as clays, may overlap the spectral regions that are used by these approaches for the estimation of gypsum content trained with the total spectral range. Studies that applied PLSR for the estimation of soil parameters have observed that the resulting models often find correlations with spectral features that do not belong to the target soil parameter, but are caused by co-correlations that may only exist for the specific test site and therefore question the robustness and transferability of PLSR models (e.g. Bartholomeus et al., 2008; Brown, Bricklemyer, & Miller, 2005), especially in the transfer from laboratory to the airborne level of data (Peon et al., 2017). Less sophisticated regression methods using spectral parameters, e.g. band ratios, are easier to transfer among

sensors and can be used as a more robust alternative to PSLS modelling, mainly because they are based on known physical characteristics of the target material (e.g. D. Li et al., 2012; Peon et al., 2017). Furthermore, the application of gypsum estimation on the remote sensing scale is challenged by factors like atmospheric absorption, illumination condition and sensor viewing geometry (Richter & Schläpfer, 2002). Especially with the planned and upcoming earth observation missions equipped with imaging spectrometers (e.g. EnMAP, PRISMA, SHALOM), hyperspectral analyses have to become more robust to different acquisition conditions and transferable to other areas, without the need for large calibration data sets to support regular monitoring of the geosphere. Most hyperspectral remote sensing studies working on gypsum assessment provide the identification of gypsum minerals or the classification as gypsiferous soils using methods such as Support Vector Machines (SVM) (Gleeson et al., 2010), Spectral Angle Mapper (SAM) (Bharti et al., 2015; Shrestha et al., 2005), Spectral Feature Fitting (SFF), Match Filtering (MF) and Spectral Mixture Analysis (SMA) (A. Dutkiewicz et al., 2009; Gleeson et al., 2010). All of these studies need an extensive training data set or rely on scene dependent selection of target spectra (endmember) for the gypsum analysis and do not provide quantitative estimates of gypsum abundance.

In this frame, the aim of this study is to evaluate suitable absorption feature based parameters for gypsum estimation from hyperspectral remote sensing data that can provide relative quantitative assessments without the use of training data or a selection of endmember spectra, and also can provide absolute quantification when ground truth data are available. For model calibration, empirical prediction functions based on spectral absorption feature have the advantage that they are directly related to the known physical properties of the material, and bear the potential to develop repeatable and transferable methods to regions of similar environmental conditions (Mulder, de Bruin, Schaepman, & Mayr, 2011). These methods are generally less prone to data inherent noise compared to exclusively statistical multivariate based prediction methods like PSLR (Bayer, Bachmann, Rogge, Müller, & Kaufmann, 2016) and can still provide relative quantitative assessments without the use of training data. Furthermore, such techniques can be incorporated in present software toolboxes for soil properties mapping such as the HYSOMA/EnSoMAP (Chabrillat et al., 2011; Chabrillat, Guillaso, Rabe, Foerster, & Guanter, 2016), which opens the analytical potential for a broad non-expert community and soil applications.

In this study gypsum models based on different parameters for the absorption features are first calibrated and tested under controlled laboratory conditions. Subsequently, the gypsum prediction functions are applied to hyperspectral imagery of different sensors and scales to evaluate the

approach under variable conditions, e.g. different sensor radiometry, spectral and spatial resolution. Specifically, spaceborne EO-1 Hyperion imagery (Pearlman et al., 2003), airborne HySpex imagery (Norsk Elektro Optikk, 2017) as well as a simulated dataset of the upcoming EnMAP sensor (Guanter et al., 2015) are considered for the evaluation of gypsum retrieval methods based on absorption features parameters for future large-scale quantification of soil gypsum content.

This study focuses on the Omongwa salt pan test site, which is a natural playa basin located in the Namibian Kalahari region. The Omongwa pan presents a large (~5x3 km) exposure of vegetation-free, unconsolidated and evaporite rich sediments with a high range in local gypsum abundances and high variability in surface mineralogical mixtures.

2. Material and Methods

2.1. Field and Laboratory Data

Field campaigns for sampling acquisition took place on 14-16 October 2014, 4-6 June 2015 and 3-5 March 2016 at the Omongwa pan located in the south-western Kalahari, Namibia. The properties and mineralogy of the pan deposits were extensively studied and discussed by F. Mees and colleagues (Mees, 1999; Mees, Casteñeda, Herrero, & Ranst, 2012; Mees, Hatert, & Rowe, 2008). The top soils of the pan are mainly gypsiferous, low in organic matter and consist of sand-sized detrital grains with varying mixtures of quartz, gypsum, halite and calcite with minor content of clay minerals sepiolite and montmorillonite, with variable spatial distribution along the pan (Mees, 1999; Milewski, Chabrillat, & Behling, 2017). The climate in this region is semi-arid with average precipitation of 200-250 mm (Mees, 1999). **Figure 14** shows the location of the study area, and spatial distribution of surface sample acquisition. The sampling focused on areas with high gypsum content along the border of the pan, and following a gradient sampling scheme from high to low gypsum content towards the centre of the pan. Towards the slightly lower elevated pan centre the top crust contains less gypsum and is increasingly dominated by halite, which is enriched in the top sediments through capillary rise during the pan's desiccation stage (Milewski et al., 2017).

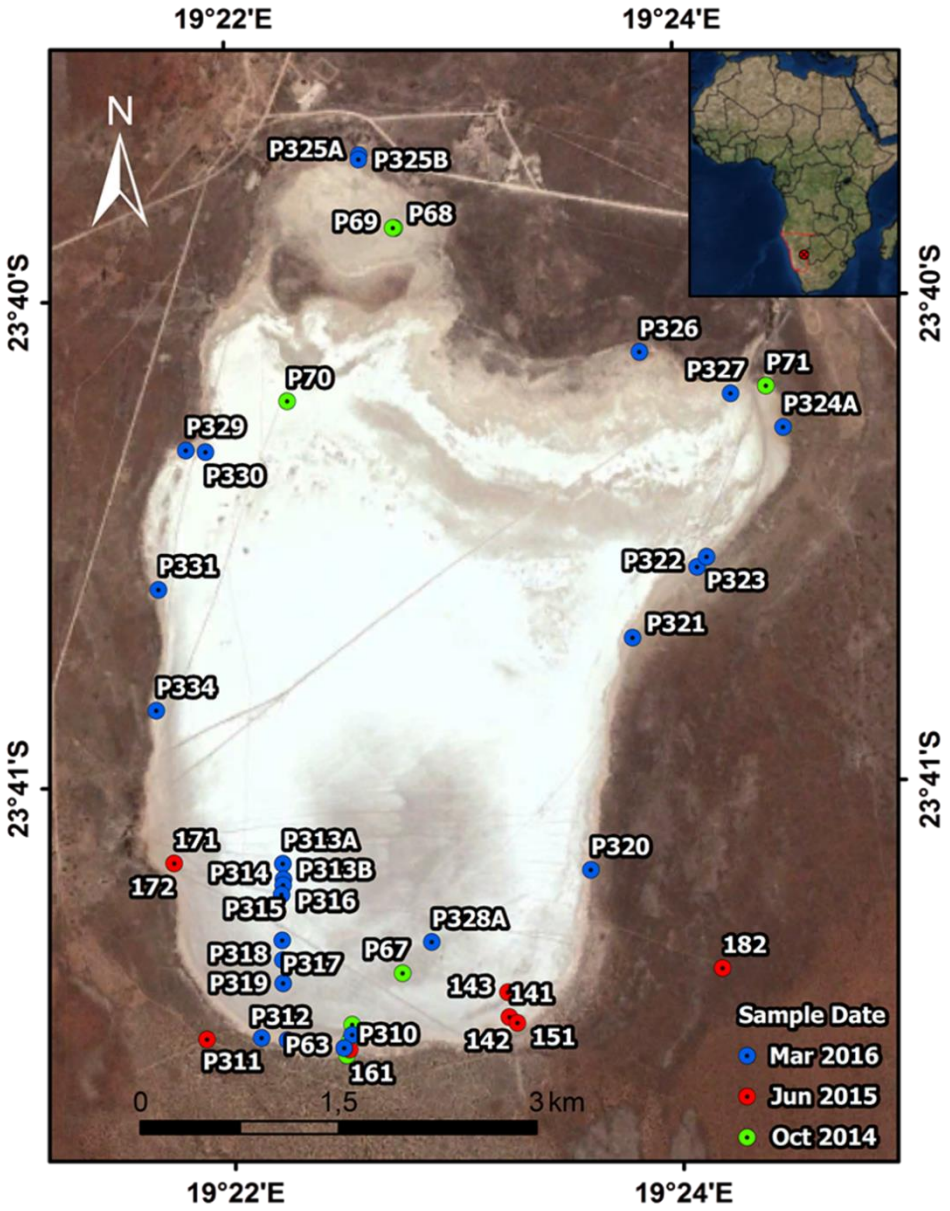

Figure 14. Omongwa pan test site and sample location (Basemap source: DigitalGlobe RGB image, September 2013, provided by Google Inc. (Mountain View, CA, USA)).

A total of 49 top surface crust (<2 cm) samples were collected in homogeneous areas. For 16 of these samples it was possible to isolate the very top surface crust from the more mixed layers below. All samples were composed of 5 to 10 sub-samples collected at random locations within a 5 m wide square around the centre point for each site of interest. Prior to sampling, field spectra of the untouched surfaces were collected at the selected locations using an ASD (Analytical Spectral Devices) FieldSpec 3 spectroradiometer, covering the VNIR-SWIR spectral range 420-2450 nm with 3 to 10 nm spectral resolution and 2151 wavelengths resampled to 1 nm (ASD Inc., 2015). Per site of interest, 5 spectra were acquired at nadir configuration from 1 m height with a ~25 cm target

radius from the centre of each location. All samples were air-dried, and divided into homogeneous sub-samples for spectral and chemical analyses.

Laboratory spectral characterisation over bulk samples was performed with the same spectroradiometer, but under controlled environmental and illumination conditions simulating spaceborne observations (sensor nadir viewing, light source azimuth 35°). A spectral library associated with the optical signatures of the 49 soil samples were created using ENVI 5.3 (Harris Geospatial Solutions, 2015) after correcting the detector offset and averaging the 5 measurements per target.

Mineral characterization was carried out using a PANalytical Empyrean powder X-ray diffractometer (XRD) with a theta-theta-goniometer, Cu-Kα radiation (λ = 0.15418 nm), automatic divergent and anti-scatter slits and a PIXcel3D detector. Diffraction data were recorded from 4.5° to 85° 2Θ with a step-size of 0.0131 and a step time of 60 s. The generator settings were 40 kV and 40 mA. All samples were crushed and powdered to a grain size of <62 micron. These samples were used for the qualitative and quantitative mineral analysis. A few samples were also powdered to <10 micron, but no strong differences in intensities were observed. The qualitative phase composition was determined using the software DIFFRAC.EVA (Bruker), and the quantitative mineralogical composition of the samples (in weight %) was calculated using a Rietveld based method implemented in the program AutoQuan (GE SEIFERT; (Taut et al., 1998).

2.2 Remote Sensing Data

2.2.1 Spaceborne EO-1 Hyperion

The EO-1 Hyperion hyperspectral image used in this study has been acquired on the 7th September 2014 at 07:34 UTC with a sun azimuth of 63° and a sun elevation of 36°. The Hyperion sensor covers the VNIR-SWIR spectral region (400-2500 nm) with 198 wavelengths of ~10 nm bandwidth at a spatial resolution of 30 m (Pearlman et al., 2003). The signal-to-noise ratio (SNR) is specified as ~140:1 to 190:1 for the VNIR and 96:1 to 38:1 for the SWIR detector (Pearlman et al., 2003).

An automated preprocessing chain for EO-1 Hyperion data developed by (Rogass, Guanter, et al., 2014) is used that provides georeferenced surface reflectance data. The L1 radiance data (L1R), L1T radiance terrain corrected data, acquisition parameters from the metadata and an ASTER 30 m DEM, freely distributed through the USGS EarthExplorer data portal (http://earthexplorer.usgs.gov/) are used. Data processing includes rescaling to radiance, removal of the spectrally overlapping bands, bad band detection, reductions for dead pixel and erroneous

detector columns, as well as corrections for intra-band spatial shifts, keystone, erroneous co-registration, radiometric miscalibration. The processing chain includes the atmospheric correction as proposed in (Guanter, Richter, et al., 2009; Guanter, Segl, et al., 2009) originally designed for the EnMAP Box (van der Linden et al., 2015). It includes a complex Radiative Transfer Modelling (RTM), Aerosol Optical Thickness (AOT), Columnar Water Vapour (CWV) retrieval as well as spectral Smile and adjacency correction (Rogass, Guanter, et al., 2014). Georeferencing is performed via GCP (Ground Control Point) selection and first order transformation using ENVI 5.3 (Harris Geospatial Solutions, 2015) between the corrected image and the orthorectified L1T Hyperion image. The geometrical transformation is applied at the end of the correction process on final mineralogical mapping results to prevent resampling effects for the spectral analyses.

2.2.2 Airborne HySpex

The airborne datasets were obtained at an altitude of 2850 m above ground level over the Omongwa pan on the 6th June 2015 during a GFZ/DIMAP airborne campaign (http://dimap-spectral.com/). The hyperspectral data have been acquired using two HySpex cameras (Norsk Elektro Optikk) in nine flightlines with alternating SE/NW heading under blue sky conditions at 10:30-12:00 UTC with a sun elevation angle of 40-45° and sun azimuth angle of -10° to 20°. The NEO HySpex system consists of two push-broom hyperspectral cameras (VNIR-1600 operating over the 0.4-1.0-µm and SWIR-320m-e operating over 1.0-2.5 µm range) with a total of 416 wavebands and a spectral resolution of 3.7 nm (VNIR-1600) and 6.0 nm (SWIR-320m-e) (Norsk Elektro Optikk, 2017). The original ground sampling distance (GSD) of the image captured was 1.2 m for the VNIR spectrometer and 4.4 m for the SWIR-320m-e camera with a field of view expander.

The preprocessing of the HySpex data to orthorectified reflectance was realized with the GFZ in-house processing chain HyPrepAir. In a first step, physically based atmospheric correction of the HySpex data was carried out in sensor geometry for the separated VNIR and SWIR sensors with the ATCOR-4 software (Richter & Schläpfer, 2016) based on the radiative transfer model MODTRAN 5 (Richter & Schläpfer, 2002). A desert aerosol model, water vapour column of 1.0 g m^{-2}, and a visibility of 60 km, were selected as atmospheric parameters. Spectral smile could be detected and removed using the ATCOR-4 smile detection routine. In a second step, a direct geometric correction was realized. The VNIR sensor was used as a reference to co-register the SWIR sensors automatically based on a ray tracing procedure (Brell, Rogass, Segl, Bookhagen, & Guanter, 2016). Thus the SWIR spectra are implemented and adapted to the overlapping VNIR spectra wavelength. The used modules and algorithms adopted for the geometric processing are described in (Brell et al., 2016).

Then the flight stripes were composed into a single mosaic with a spatial resolution of 2.3 m without image feathering or colour balancing to keep the original data values. To further remove atmospheric attenuation and spectral artefacts an Empirical Line Calibration (ELC) (Aspinall, Marcus, & Boardman, 2002) implemented in ENVI 5.3 (Harris Geospatial Solutions 2015) was performed using field-measurements of several reflectance targets with different albedo.

2.2.3 Simulation of Spaceborne EnMAP Data

The simulation of the EnMAP reflectance product (Level-2A) at 30 m resolution was performed on the basis of the preprocessed airborne HySpex mosaic using the EnMAP end-to-end simulation software EeteS (Segl et al., 2012). The EeteS software follows the forward and backward processing schemes simulating the EnMAP image generation process, sensor calibration and data preprocessing. The EnMAP sensor consists of a dual-spectrometer instrument measuring in 242 spectral bands between 420 and 2450 nm with a spectral sampling distance varying between 5 and 12 nm (Guanter et al., 2015). It has a measured signal-to-noise ratio of 400:1 in the visible and near-infrared and 180:1 in the shortwave-infrared parts of the spectrum that is considered in the EeteS sensor model (Segl et al., 2012). Sensor-like raw image data were produced using the HySpex airborne imagery. Next, the data were transformed to Level 1C applying a detector co-registration and image orthorectification, then subsequently processed to reflectance orthorectified data (Level-2A) applying an atmospheric correction.

2.3. Selection and Parametrization of Absorption Feature

The application and parametrization of spectral absorption features in general are complicated due to the influence and overlapping of other spectral features from multiple sources (e.g. other soil components or atmosphere influence). This emphasises the need for a thoughtful selection of the most suitable absorption feature to the application scenario. The reflectance of gypsum shows multiple characteristic absorption features (**Figure 15**). Most prominent are triple absorption features around 1.5 µm, as well as further features at 1.75 and 2.2 µm in the VNIR-SWIR spectral region (Drake, 1995; Hunt et al., 1971).

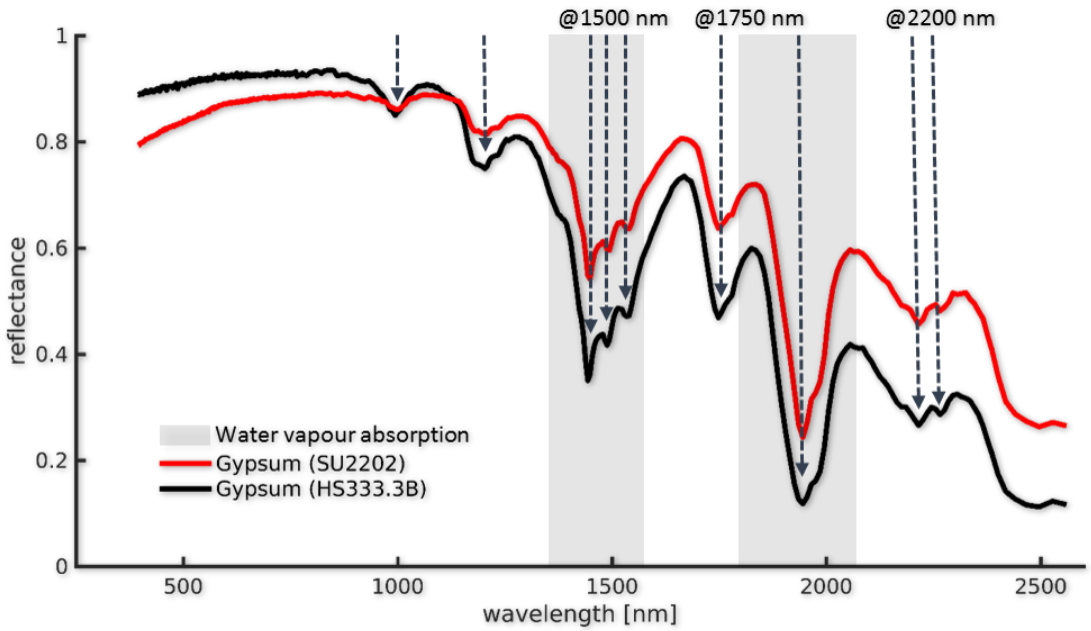

Figure 15. USGS laboratory spectra of the mineral gypsum (Clark et al., 2007). The major gypsum absorption wavelength and water vapour absorption regions are indicated.

For remote sensing applications, the triple absorption feature at 1.5 µm is not suitable due to atmospheric water vapour absorption. The gypsum 2.2 µm doublet absorption could be confused with the 2.2 µm clay absorption feature in soils and thus is problematic for spectral discrimination, especially in data with low spectral quality. Therefore the 1.75 µm feature is selected as the best discriminator for the quantification of gypsum absorption for the most common soil mixtures and acquisition conditions. However, absorption features caused by vegetation coverage as well as soils mixed with dry plant remains e.g., starch, cellulose and several other biochemical constituents may overlap gypsum features and limit the capability for gypsum mapping when partial vegetation cover is present at the surface. Notably the dry plant pigments cellulose and lignin absorb close to the 1.75 gypsum absorption feature (Kokaly and Clark 1999). Another overlapping absorption exists between gypsum and hydrocarbon based materials like oil and plastics that have an absorption maximum at 1.73 µm (Kühn, Oppermann, & Hörig, 2004), which can be introduced into the soil by environmental pollution.

In feature parametrization, the spectral datasets are analysed for the selected spectral characteristics of the target material (in this case gypsum) and are transferred to numerical parameters or variables that describe the shape of the spectral feature. These numerical parameters correlate with the concentration of the target material in a mixed sample. The following four parameters are derived from the selected absorption feature: 1) the Normalized Difference

Gypsum Ratio (NDGI), 2) the Continuum Removed Absorption Depth (CRAD), 3) the Slope, and 4) the Half-Area (**Figure 16**).

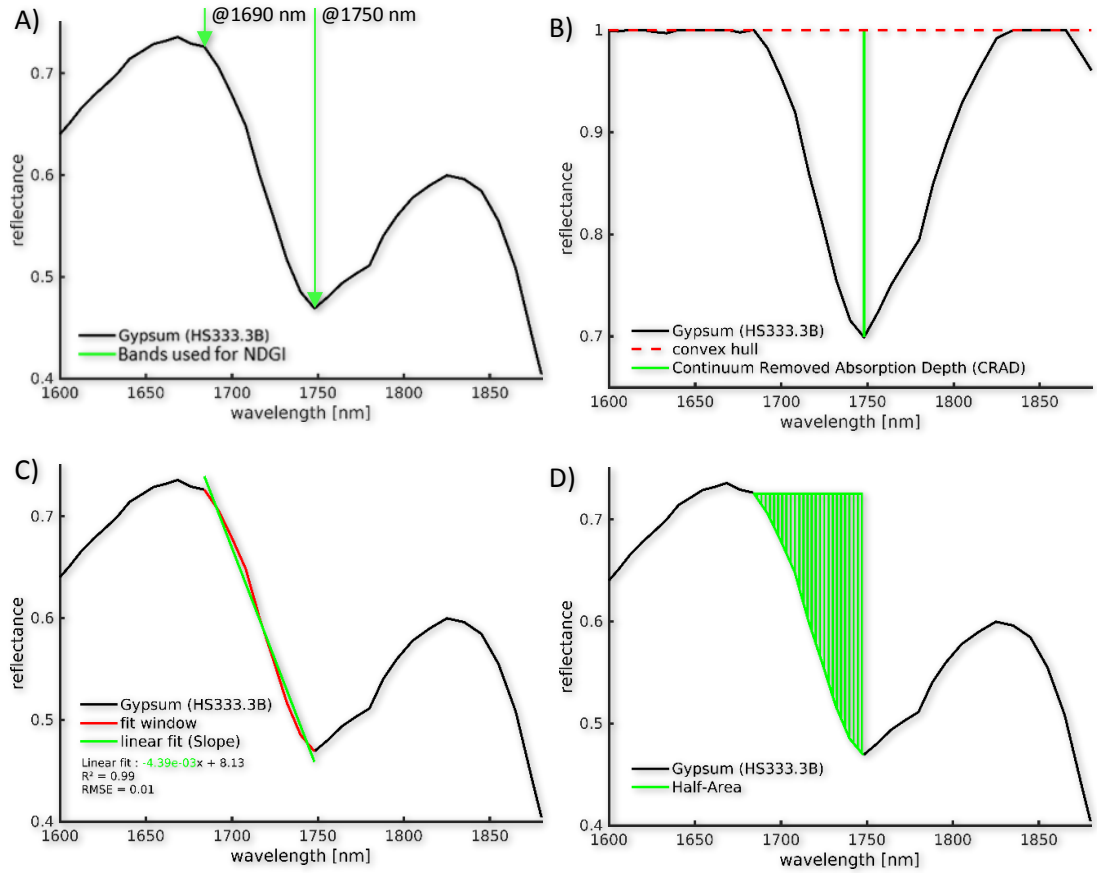

Figure 16. Absorption feature parameters tested for gypsum estimation. A) Normalized Difference Gypsum Index (NDGI), B) Continuum Removed Absorption Depth (CRAD), C) Slope and D) Half-Area. The exemplary gypsum spectrum is from USGS spectral library (Clark et al., 2007).

All of the tested parameters operate in a very limited wavelength range of 60 - 100 nm (between 1690 - 1790 nm), which provides the advantage that the analysis is more robust against spectral overfitting to unrepresentative correlations that may appear outside of the wavelength region of interest, as well as against radiometric uncertainties which is especially threatening for modelling from small number of observations. The wavelength positions used for the parameterization were chosen after testing regression models for each band combination in the wavelength range of the gypsum feature (1690 - 1790 nm) based on the laboratory dataset with 1 nm spectral binning.

The Normalized Difference Gypsum Ratio (NDGI) calculates the normalized ratio between the most relevant narrow spectral bands of the gypsum absorption feature (**Figure 16A**) such as:

$$NDGI = \frac{(r1690\ nm - r1750\ nm)}{(r1690\ nm + r1750\ nm)}$$

, where r is the reflectance at the stated wavelength. It follows the principles of the established Normalized Difference Vegetation Index (NDVI), which has been extensively used for vegetation analysis (Gao, 1996), and the Normalised Soil Moisture Index (NSMI) used for soil moisture estimation from hyperspectral imagery (Haubrock, Chabrillat, Kuhnert, Hostert, & Kaufmann, 2008). Such band ratios are easy-to-use mathematical algorithms, transforming multi-band data into a single parameter showing the presence and relative quantity of the target material. They can be effective parameters for spectral analysis, when applied with a well-formulated rationale (Mustard & Sunshine, 1999). For imaging spectroscopy band ratios have already been proven successful for the estimation of different soil components, e.g. iron-oxide (E. Ben-Dor et al., 2006), clay content (Levin, Kidron, & Ben-Dor, 2007), but so far have not been tested for gypsum estimation.

The second parameter tested for the gypsum estimation is the Continuum Removed Absorption Depth (CRAD). This parameter is derived using the continuum removal method (Clark & Roush, 1984) integrated in the HYSOMA software (Chabrillat et al., 2011). CRAD is the difference between the continuum defined by the convex hull between the shoulder positions and the absorption maximum (**Figure 16B**):

$$CRAD = 1 - \frac{r1750\ nm}{r_C 1750\ nm}$$

, where r is the measured reflectance and r_C the reflectance of the convex hull at the absorption maximum. While the left shoulder for the gypsum CRAD calculation is well defined at 1690 nm, the wavelength position for the right shoulder at 1790 nm is chosen as trade-off between the ideal reflectance shoulder position at ~1850 nm, under laboratory conditions (with minimal atmospheric thickness between target and sensor), and the increasing influence of water vapour absorption at that wavelength range under remote sensing conditions. Spectral analysis techniques such as the CRAD that parameterise absorption features by their relative depth from the continuum removed reflectance have originally been developed for mineral mapping (Clark, 1983; James K. Crowley, Brickey, & Rowan, 1989). This method of waveform characterization (Okada & Iwashita, 1992) has been proven successful for remote sensing analysis of a wide range of applications (Van der Meer, 2004), such as different soil components (Bayer, Bachmann, Kaufmann, & Mueller, 2012; Chabrillat

et al., 2011), plant materials (Kokaly & Clark, 1999), hydrocarbons (Kühn et al., 2004), as well as geological applications (Kokaly, King, & Hoefen, 2011; Mielke, Rogass, et al., 2016).

The third and fourth parameters tested for the gypsum estimation are the Slope and Half-Area of the absorption feature. In this paper the spectral Slope is defined as the gradient of a linear fit of the left-hand side of the absorption feature (**Figure 16C**):

$$Slope = \frac{\sum_{i=1}^{1} (x_i - \underline{x})(r_i - \underline{r})}{\sum_{i=1}^{n} (x_i - \underline{x})^2}$$

, where r is the reflectance and x the wavelength of the bands between 1690 nm and 1750 nm. The Half-Area represents the surface area above this wavelength range (**Figure 16D**) approximated using the trapezoidal method (Burden & Faires, 2011):

$$HalfArea = \int_a^b f(x)\,dx \approx \frac{b-a}{2N} \sum_{n=1}^{N} (f(x_n) + f(x_{n+1}))$$

on the zero scaled and inverted reflectance f at wavelength x with $n+1$ evenly spaced points, where n is the number of bands between the left shoulder $a = 1690\,nm$ and the absorption maximum $b = 1750\,nm$. Both parameters include information from all wavelengths of the respective sensor between the left shoulder and the absorption maximum, which makes these shape parameters potentially more robust against random radiometric uncertainties that occur in single bands, compared to NDGI and CRAD parameters that only use two or three bands in their calculations. In imaging spectroscopy the analysis of shape-based parameters of absorption features is less common compared to the other types of parameterization, but nonetheless the concept shows promising results, e.g. for the estimation of soil components (Bayer et al., 2012).

2.4 Laboratory Prediction Models and Transfer to Remote Sensing Imagery

From the laboratory spectral library, the four absorption feature parameters were derived and their relationship to the gypsum content of the 49 soil samples were modelled using linear least squares regression and the performance was assessed by leave-one-out cross-validation and expressed by the standard performance indicators, explained variance (R^2) and Root Mean Square Error (RMSE). The calculation of absorption feature parameters as well (The MathWorks, Inc., 2016).

In the next step, the resulting prediction function based on the laboratory measurements spectrally resampled to each sensor was applied to the absorption feature parameters derived from the remote sensing imagery of the Hyperion, HySpex and simulated EnMAP sensor. For this purpose,

the image spectrum closest to each sample position was extracted. The predicted gypsum content of the transferred regression models were compared to the XRD measured gypsum content for the 16 sample locations that represent comparable surface conditions between remote sensing and field data acquisition. It is necessary that surface conditions between sample collection and remote sensing data acquisitions are the same or at least in a reasonable comparable state. In previous analysis of the test site's surface dynamic it was found that the gypsum crust's mineralogical composition at the pan border is mostly stable in the long term (the last ~30 years) (Milewski et al., 2017). However, in the short term the physical conditions fluctuate and can still have significant influence on the reflectance signal, e.g. through differences in surface roughness and moisture. These changes are mainly caused by rainfall events and to much lesser extent by wind erosion in the dry season. Therefore, only surface samples in dry conditions were selected for the model validation of the remote sensing data. Surface conditions during the 2014 and 2015 campaign were mostly dry with well-developed surface crusts that have been developed during the dry season with 3 and 1.5 months after the last heavy precipitation events respectively for 2014 and 2015. However, during the March 2016 field campaign the pan sediments were still wet from the last precipitation events (see **Figure 17**).

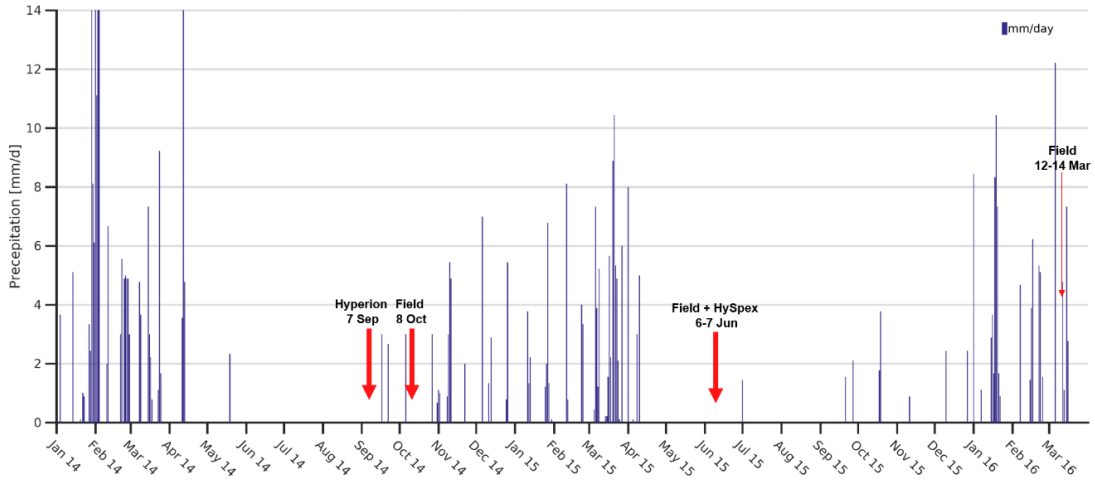

Figure 17. Precipitation estimates at the test site and dates of field sampling and remote sensing data acquisition (Precipitation estimates provided by TAMSAT (Maidment et al., 2014)).

This prevented the exclusive sampling of the upper surface crust in 2016 and lead to a mixture with the underlying mineralogy. These mixtures cannot be used to represent the surface condition during the air and spaceborne data acquisition. Therefore, these samples were excluded for model validation based on remote sensing data and they were only used for the laboratory model calibration. Furthermore, samples located in changing areas such areas affected by an episodically

active inflow channel at the north-eastern pan border were excluded from the validation data set. This leaves a limited data set of 16 samples for the validation of the remote sensing based gypsum models and the full set of 49 samples for the calibration of the laboratory gypsum model. The validation samples represent a well stratified range in gypsum values (0-60%) even with the limited sample size.

3. Results

3.1 Mineralogical Analysis of Field Samples

The XRD analysis of the 49 field samples from the Omongwa pan's topsoil shows a mixture of gypsum, halite, quartz, calcite and the clay mineral sepiolite (**Figure 18**) and a high variability in gypsum content (**Figure 19**) with a mean of 31% and a standard error of 28% (min. 0%, max. 85%). The sample distribution is positively skewed with half of the samples having a gypsum content below 30% and a quarter of the samples below 10%. Samples with mid-range gypsum values (40-70%) are more sparse and a cluster of high gypsum samples of 70-80% can be observed.

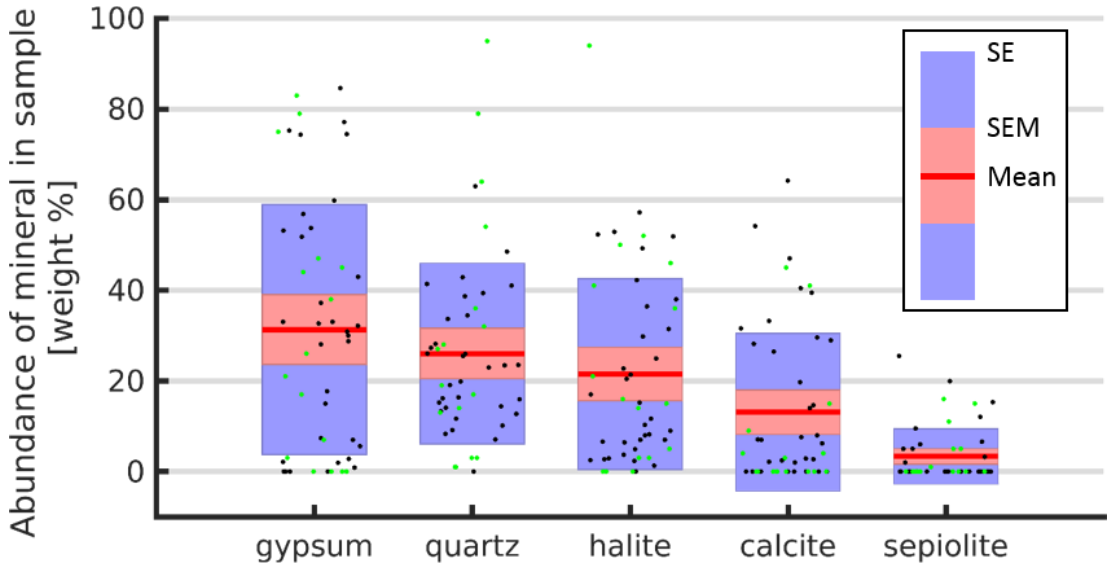

Figure 18. Ranges of the mineral abundance (wt. %) present in the 49 field samples (samples used for validation are shown in green). Mean, Standard Error of the Mean (SEM) and Standard Error (SE) are indicated.

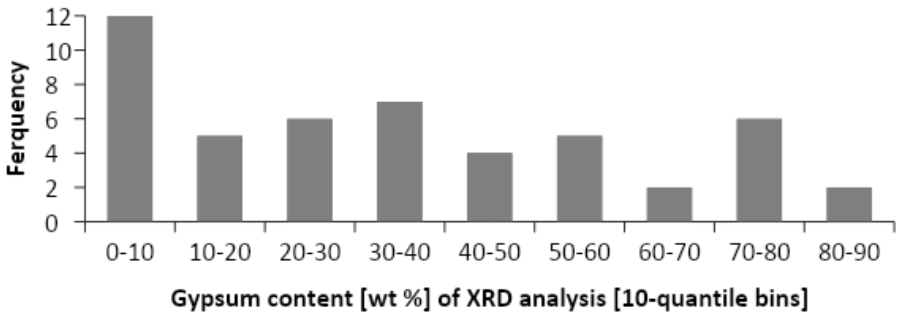

Figure 19. Distribution of gypsum content present in the 49 field samples.

3.2. Remote Sensing Data

Figure 20 shows a colour composite of SWIR bands from the three sensors tested for gypsum mapping. Spectral bands of the SWIR sensor are selected, because the data quality of this spectral range is most relevant for the gypsum estimation function. Main differences between images are diagonal spatial patterns that are oriented along the path of the data acquisition. For the Hyperion data, vertical stripes (~11°) and spatial noise of the 1.6 µm band (red dots) are observed that remained after the preprocessing. Such spectral miscalibrations are often found in low SNR push-broom sensors (Ducart, Silva, Toledo, & Assis, 2016; Rogass, Mielke, et al., 2014). For the HySpex airborne and the derived EnMAP imagery, a much higher radiometric contrast can be observed. The higher albedo of the pan centre in the Hyperion scene is mainly due to a more developed halite crust at time of acquisition. The surface validations samples are exclusively located at the pan border, which significantly reduces the risk of changes of the crust's mineral composition between image acquisitions, because the gypsum border region was found to be much more stable over time (Milewski et al., 2017). However, some minor changes, e.g., due to aeolian processes or minor precipitation events may influence the model results. For the HySpex airborne and the derived EnMAP imagery some boundary effects between individual flight lines remain after preprocessing. These effects were not sufficiently removed by the applied empirical BRDF correction of ATCOR-4 (Richter & Schläpfer, 2016). Although these effects influence the overall data quality and possibly the gypsum retrieval, a comparison of the remote sensing data with a reference field spectrum show similar behaviour between the sensors at the spectral range of interest around the gypsum absorption feature (**Figure 21**). The plot also shows the limitation in the useful spectral range to 1770 nm due to the influence of the atmospheric absorption centred at ~1950 nm. Especially the Hyperion spectrum show a reduction in reflectance already at a shorter wavelength (~1780) compared to the spectra of the other sensors that further increase reflectance for approximately 10-20 nm in direction of the right shoulder of the gypsum absorption feature.

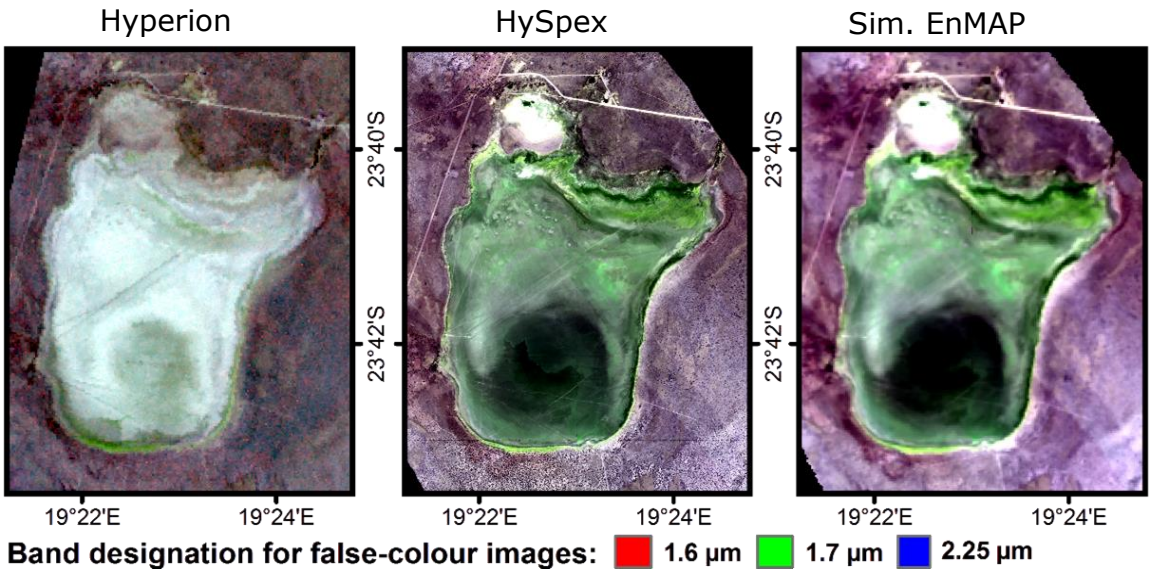

Figure 20. SWIR colour composite (R: 1.6 µm, G: 1.7 µm, B: 2.25 µm) of Hyperion, HySpex and simulated EnMAP image.

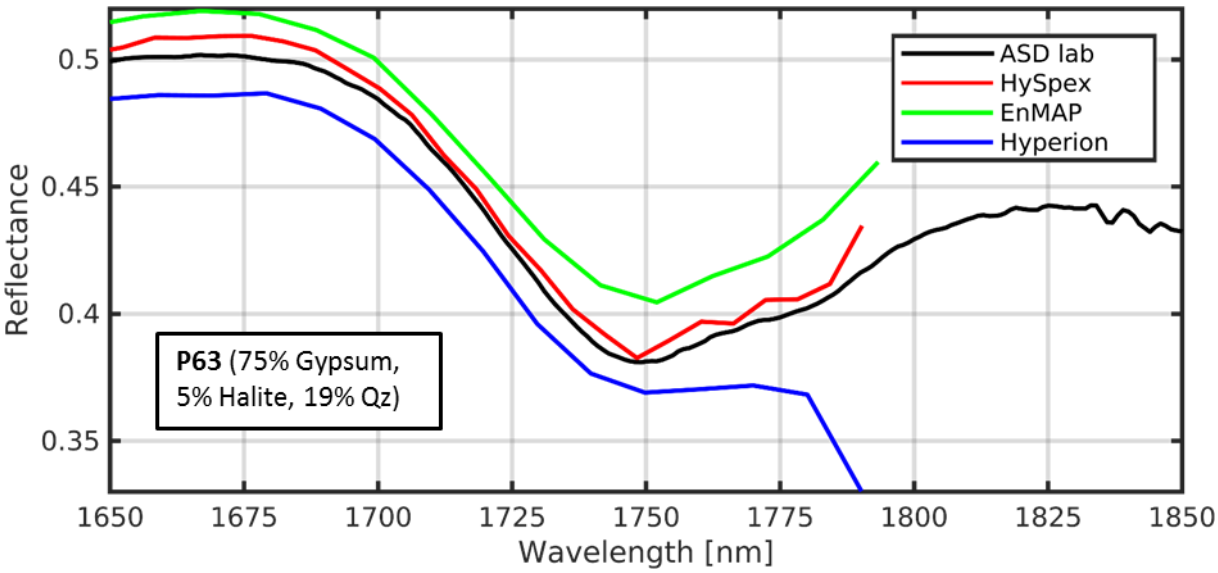

Figure 21. Reflectance of the ~1.75 µm gypsum absorption feature from Hyperion, HySpex and simulated EnMAP data at a selected ground-truth site.

3.3. Laboratory Prediction Models

Laboratory model performance statistics and regression plots are presented in Table 3 and **Figure 22**. The performance of the gypsum prediction models shows differences of up to 14% in explained model variance and 4% of RMSE between different absorption feature parameters used in the regression. The results show that the parameters CRAD and NDGI provide the strongest gypsum models with $R^2 > 0.8$ and RMSE of 11% compared to the shape-based parameters Slope an Half-

Area that have $R^2 \sim 0.7$ and RMSE of 15%. In general, the residual distributions of the laboratory models show no strong bias for a specific range of gypsum values. Spectral resampling of the laboratory spectra to the respective remote sensing sensors (binning by central wavelength position) did not lead to significant deviations in model performance compared to the full spectral resolution of the laboratory spectrometer (R^2 decreased by 1-2%).

Table 3. Performance of laboratory gypsum prediction models.

	NDGI	CRAD	Slope	Half-Area
R^2	0.84	0.86	0.73	0.72
RMSE	11%	11%	15%	15%

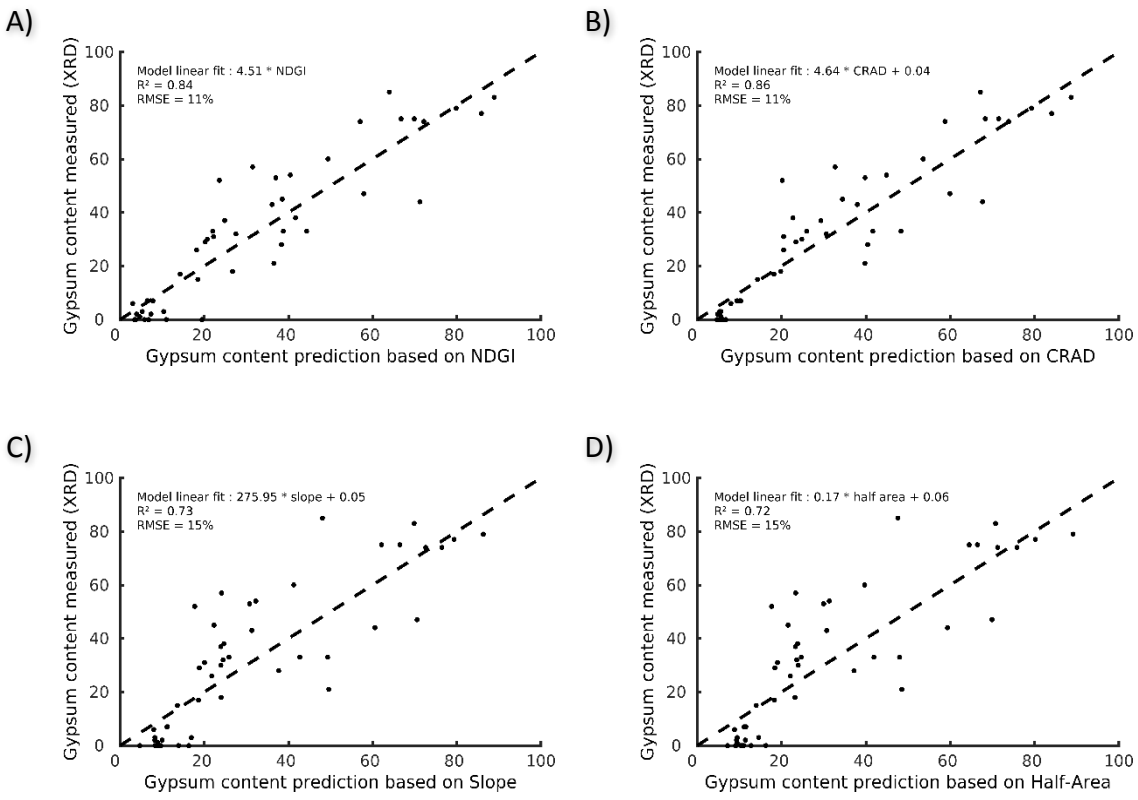

Figure 22. Plots of predicted vs. measured gypsum content [wt. %] based on laboratory ASD spectra for the absorption feature parameters: A) NDGI; B) CRAD; C) Slope; D) Half-Area. The dashed line is the 1:1 line of predicted vs. measured results.

3.3. Models Transfer to Remote Sensing Imagery

The gypsum prediction functions obtained by the laboratory models resampled to each sensor was applied to the remote sensing imagery and compared with mineralogical analysis at the 16 ground-truth locations that provide comparable surface conditions to the remote sensing acquisitions. The results are summarised in Table 4. Models based on NDGI have a high performance across all sensor with the highest validity reached for the HySpex data (R^2 = 0.79), compared to Hyperion (R^2 = 0.71) and Simulated EnMAP (R^2 = 0.68). On the other hand, across all sensors, CRAD based models have the lowest performance (R^2 between 0.34 and 0.64) and highest RMSE, unlike in laboratory models where CRAD model is the best predictor for gypsum content. The Slope and Half-Area parameters, in general, perform slightly less good, except in the case of Hyperion, where both perform slightly better than the NDGI with an R^2 of 0.75 and 0.74 respectively for Slope and Half-Area. The validation plots show the performance of the laboratory prediction functions transferred to the tested absorption feature parameter derived from the respective sensor (Hyperion in **Figure 23**; HySpex in **Figure 24**; Simulated EnMAP in **Figure 25**). In general gypsum models transferred to Hyperion and EnMAP absorption features seem to overestimate gypsum content of low gypsum samples, while underestimating high gypsum samples. The regression of the airborne HySpex predictions vs. measured gypsum content (**Figure 24**) is much closer and parallel to the 1:1 line compared to the models based on the spaceborne Hyperion (**Figure 23**) and simulated EnMAP data (**Figure 25**).

Table 4. Ground-truth validation of gypsum models applied to remote sensing data.

	NDGI		**CRAD**		**Slope**		**Half-Area**	
	R^2	**RMSE**	**R^2**	**RMSE**	**R^2**	**RMSE**	**R^2**	**RMSE**
Hyperion	0.71	14%	0.64	15%	0.75	13%	0.74	13%
HySpex	0.81	11%	0.65	15%	0.77	12%	0.76	12%
Sim. EnMAP	0.77	12%	0.58	17%	0.74	13%	0.73	13%

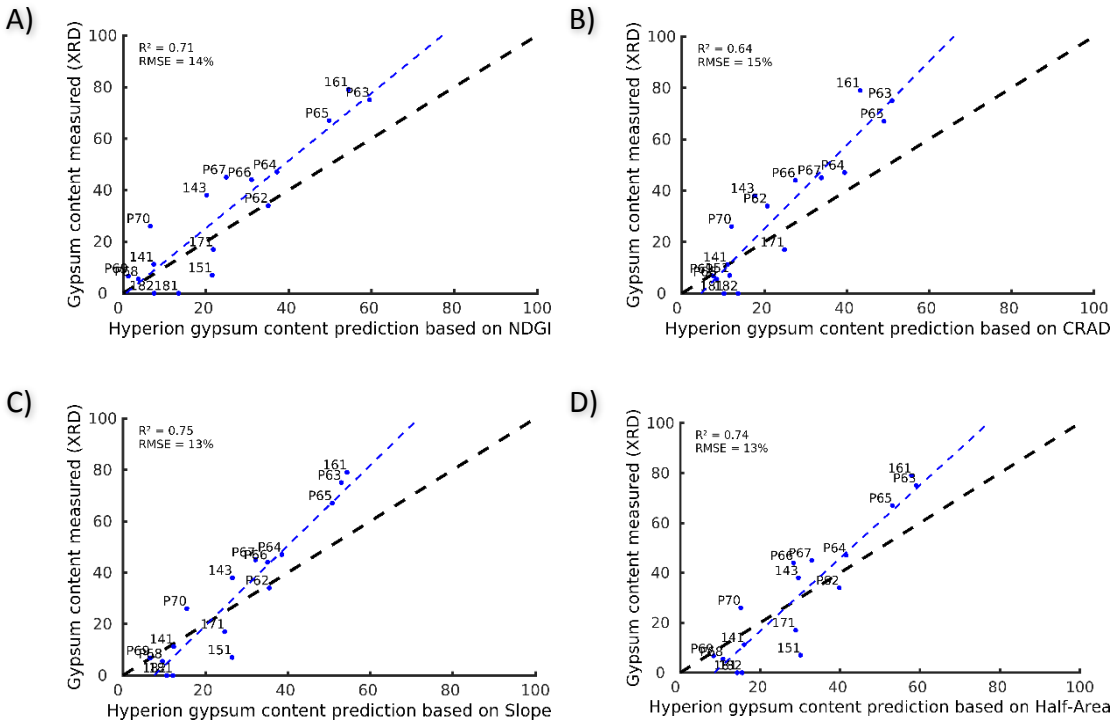

Figure 23. Plots of predicted vs. measured gypsum content [wt. %] based on laboratory prediction function applied to the EO-1 Hyperion derived absorption feature parameters: A) NDGI; B) CRAD; C) Slope; D) Half-Area. The blue line is the regression line and the black line is the 1:1 line.

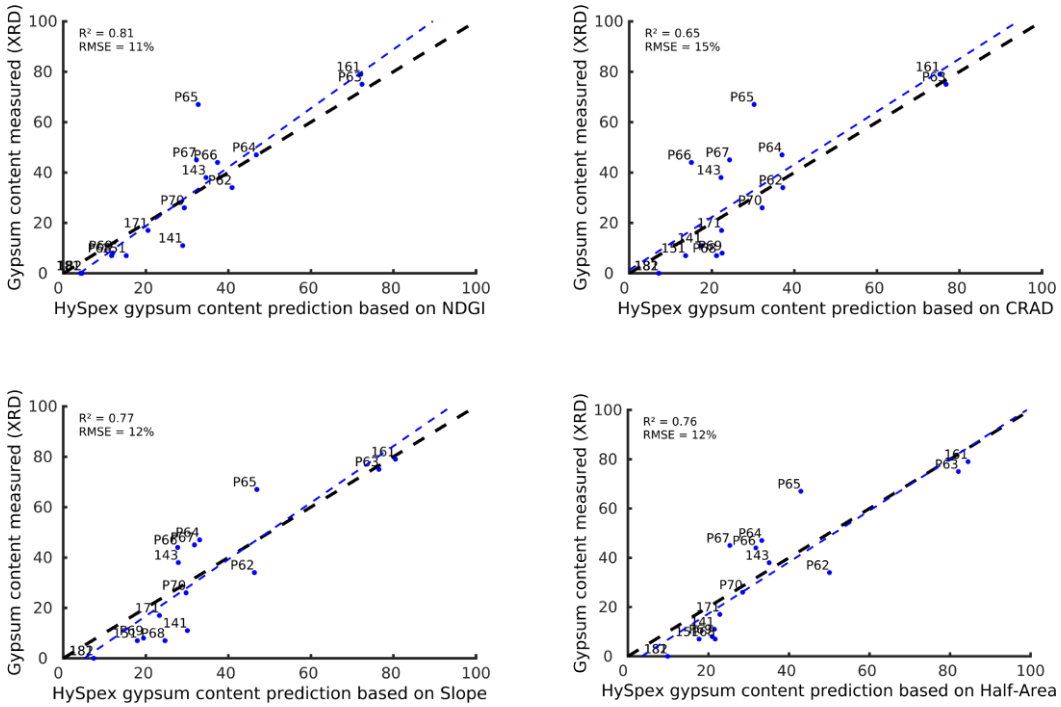

Figure 24. Plots of predicted vs. measured gypsum content [wt. %] based on laboratory prediction function applied to the HySpex derived absorption feature parameters: A) NDGI; B) CRAD; C) Slope; D) Half-Area. The blue line is the regression line and the black line is the 1:1 line.

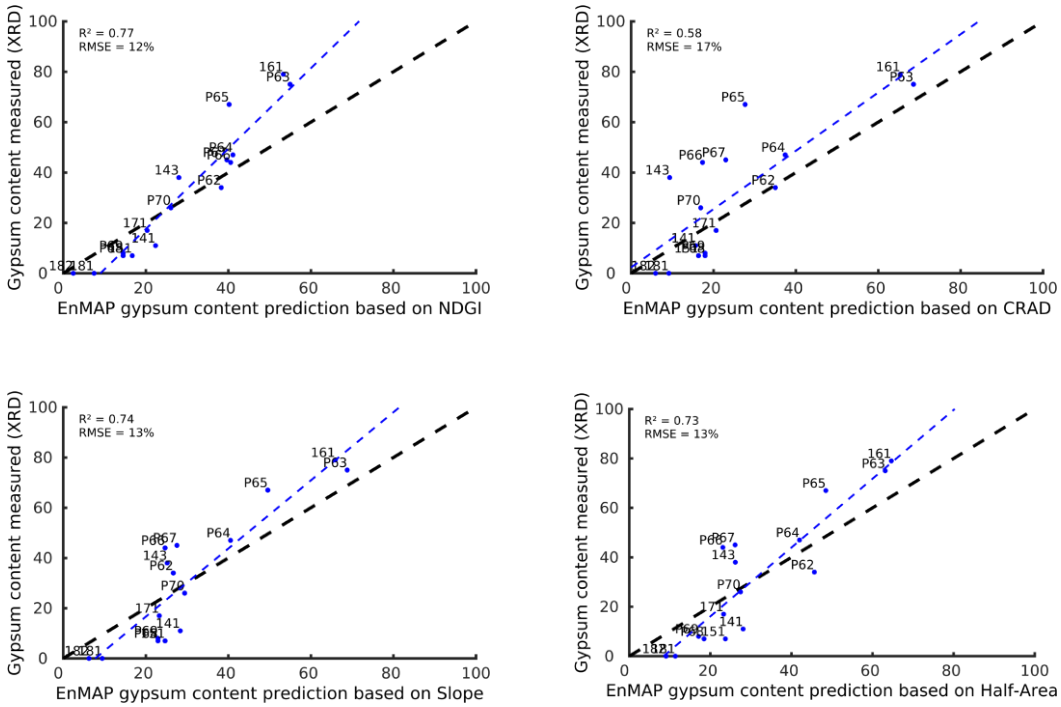

Figure 25. Plots of predicted vs. measured gypsum content [wt. %] based on laboratory prediction function applied to the simulated EnMAP derived absorption feature parameters: A) NDGI; B) CRAD; C) Slope; D) Half-Area. The blue line is the regression line and the black line is the 1:1 line.

Figure 26 shows the spatial distribution of the gypsum estimation based on the different absorption feature parameters and sensors. In general, strong differences are observed both, across sensors, as well as dependent on the parameter used for gypsum estimation. The spatial/spectral effects mentioned in section 3.2 are clearly visible. However, a more coherent spatial distribution is observed for the gypsum mapping between the highest performing model results of each sensor (Slope parameter for Hyperion and the NDGI of HySpex and Sim. EnMAP). Also, except for the highly dynamic area in the northeast corner of the pan that is associated with an ephemeral inflow channel to the salt pan (Milewski et al., 2017). The maps in **Figure 26** show similar spatial features across sensors and parameter definition such as: 1) high gypsum content at the southern, eastern and northern pan boundary, 2) mid-range values at the central circular pattern, 3) low values on the rest of the pan surface, and 4) only few false positives in the surroundings of the salt pan. In agreement with the model accuracies, the gypsum maps based on the CRAD models are of lower quality than the maps based on the other parameters. The regression models have shown that the CRAD models largely underestimates the gypsum content (**Figure 23-23**). Accordingly the CRAD gypsum maps show lower values compared to the other parameters across sensors. This is especially apparent for the circular shape at the pan centre that represent the low-medium range

of gypsum samples, which fits to the residuals of the regression model that also have the highest deviation in this range. However, for regions with very high gypsum content, which are mainly the border regions, the deviations to the gypsum maps based on other parameters is not as high. The Hyperion CRAD based gypsum map is also most affected by noise, which is indicated by many pixels that show no zero gypsum values outside of the salt pan. Because the reddish soils of the savanna landscape do not contain any gypsum, these mappings can be labelled as false positives. The isolated or randomly scattered distribution of these pixels also strengthens this interpretation as noise. The Slope and Half-Area parameters provide very similar mapping results.

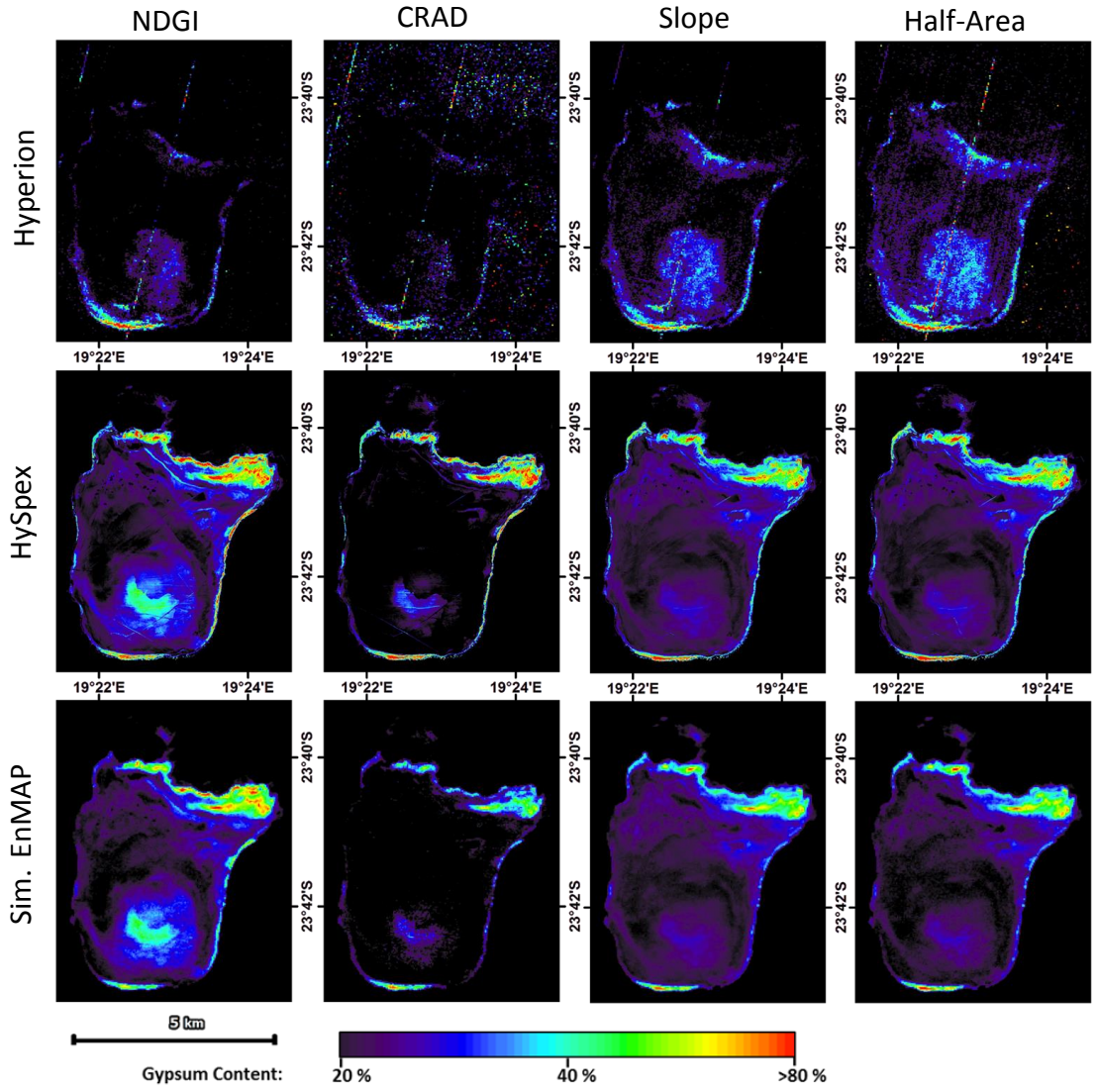

Figure 26. Gypsum maps based on different parameters for gypsum absorption feature (NDGI, CRAD, Slope, Half-Area) and sensors (Hyperion, HySpex, simulated EnMAP).

Figure 27 shows the gypsum mapping of the best performing parameter NDGI for the scene with the highest spatial resolution for the southern salt pan margin. The southern pan margin is most suitable for a detailed assessment, because most of the validation samples are located here and this area of the pan is most stable over time (Milewski et al., 2017). The centre of the subset show a sampling transect from the gypsum free, reddish sandy soil outside of the pan through the border slope region to the flat main pan area. Sample 181 in the reddish Kalahari sands outside of the pan area shows a gypsum content of 0%, which is consistent with the mapping result. The gypsum content increases to the north at the pan margin and varies there along patches with medium to high gypsum content (30-80%). More into the pan the gypsum content first decreases to about 20% (reflected at sample P66 with 24%), but increases at the beginning of the circular shape to >40%, which is reflected e.g. by sample 67 with 45% gypsum.

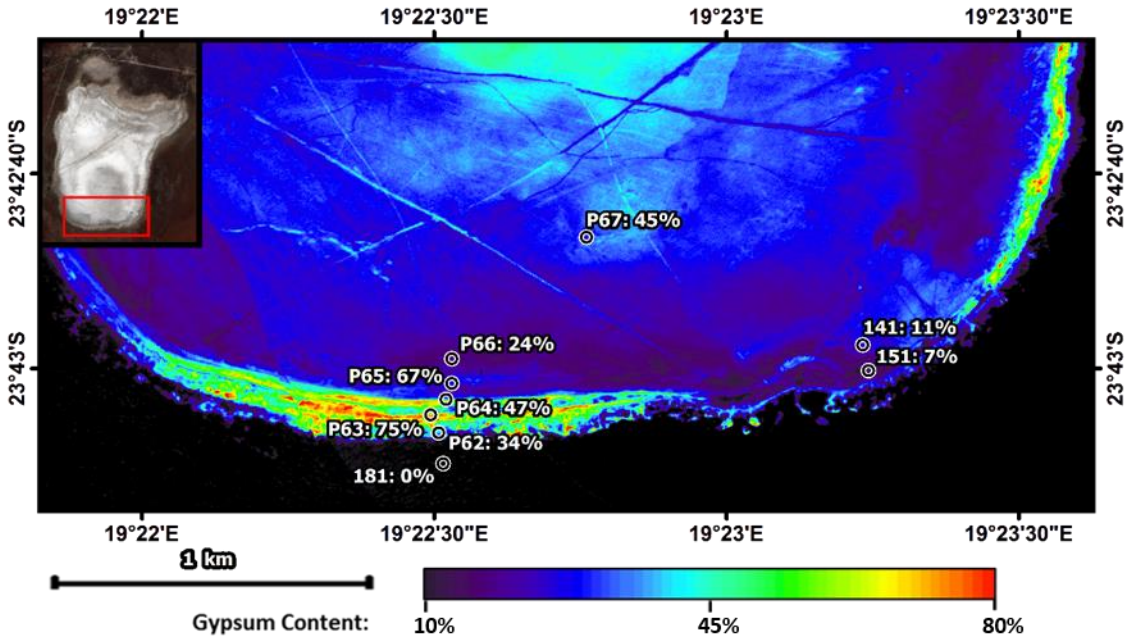

Figure 27: HySpex NDGI gypsum mapping of the southern pan border. Circles show location of validation samples and the respective gypsum content [wt. %] as analysed by XRD.

4. Discussion

The performance of the laboratory gypsum prediction models presented in this paper based on the 1.75 µm absorption feature (R^2 = 0.84 for NDGI and R^2 = 0.86 for CRAD) are comparable to previous studies where soil gypsum content was predicted using PLSR method (R^2 = 0.86) and CRAD parameter (R^2 = 0.85) (Khayamim et al., 2015). The comparison to PLSR modelling shows that the reduction of spectral information to absorption feature parameters causes only marginal decrease in model performance, while having the advantage of being more robust and less site specific. Weindorf (2016) (Weindorf et al., 2016) achieved much high model performances (R^2 = 0.95) for gypsum prediction by combining hyperspectral with X-ray fluorescence (XRF) data in penalized spline regression (PSR) and random forest (RF) selection. However, they note that the strong correlation of several highly ranked wavebands are probably caused by site specific effects or remain unexplained (Weindorf et al., 2016). The introduction of XRF data as an additional variable besides reflectance is only feasible for proximal sensing and not applicable to remote sensing.

This paper is the first study that is looking at the potential for the retrieval of gypsum content of soils based on hyperspectral remote sensing imagery that provides quantitative results, without the need for site specific endmember extraction. Most previous remote sensing studies provide the detection and mapping of gypsiferous soils, e.g. through spectral feature fitting (A. Dutkiewicz et al., 2009), spectral unmixing, Spectral Angle Mapper (SAM) (Shrestha et al., 2005) or Mixture Tuned Matched Filtering (MTMF) (Ghrefat & Goodell, 2011), but do not provide quantitative gypsum estimations that could be compared to this study. However, already in 1996 Bryant (Robert G. Bryant, 1996) correlated gypsum endmember abundances extracted from multispectral Landsat TM imagery to XRD mineralogy (R^2 = 0.9), based on low sample size (n = 12) and a regression model that strongly underestimates gypsum content of pure pixels (Robert G. Bryant, 1996). While such an approach on multispectral data would allow multitemporal monitoring, it relies on the site-specific extraction of image endmembers for the unmixing model.

The results of our study show that prediction models based on the 1.75 µm absorption feature can successfully be used to estimate gypsum abundances from hyperspectral imagery, with R^2 greater than 0.8 for airborne hyperspectral imagery (GSD 2.4 m) and R^2 greater than 0.75 for spaceborne hyperspectral imagery (GSD 30 m). The observed model performances vary strongly dependant on the parametrisation and sensors used. Across all sensor models based on NDGI show high performances, whereas CRAD based models have the lowest R^2 and highest RMSE, which is different from the laboratory model performance, where CRAD is the most performant parameter.

In contrast to NDGI and the shape-based parameters that that are directly calculated based on the reflectance value, the Continuum-Removed Absorption Depth (CRAD) needs to calculate the spectral continuum first. For this procedure it is necessary to know the reflectance values at the absorption centre, as well as the left and right shoulder positions of the absorption feature. For data acquired by airborne/satellite remote sensing the reflectance of the right shoulder of the gypsum feature (at ~1780 nm) is noisy, because it is very close to the absorption feature caused by atmospheric water vapour that reduces amounts of incident and reflected light so that information over these regions becomes unavailable (Clark, 1999) or at least highly affected by noise (Murphy, 2015). In spectroscopy the continuum removed reflectance is normally preferred because it isolates the spectral feature from background absorption caused by other components in the mixture (Clark & Roush, 1984). The gypsum estimation based on Hyperion data certainly is more strongly affected by the water vapour absorption. Compared to the other sensors the reflectance of Hyperion is already reduced at a ~20 nm shorter wavelength position (**Figure 21**). Accordingly, the resulting gypsum maps show the most noise in the Hyperion CRAD image. This effect is partly explained by the generally lower SNR of Hyperion sensor and also the longer atmospherically pathway of the spaceborne sensor. The proximity of the water vapour absorption at the 1.75 µm feature is most likely also the reason, why expert rule software systems like the Material Identification and Characterization Algorithm (MICA) (Kokaly et al., 2011) include the 2.2 µm feature to identify gypsum despite the conflicting clay absorption at this wavelength. Thus, while the CRAD is the preferable parameter for gypsum estimation in the laboratory, where atmospheric influence is minimal, only the left-hand side of the absorption feature should be used on the remote sensing level and parametrization such as the NDGI are recommended for the quantitative determination of gypsum content as they provide robust results. Another solution might be to reconstruct the absorption feature with information from the left half, e.g. by inverted Gaussian modelling (Sunshine, Pieters, & Pratt, 1990; Whiting, Li, & Ustin, 2004).

Concordant to the model performance from the laboratory analyses the Slope and Half-Area parameters perform slightly less good compared to the band ratio based NDGI, except in the case of Hyperion, where both perform slightly better than the NDGI (R^2 of 0.75 for Slope). Instead of the two bands that are used for the calculation of the NDGI (left shoulder and absorption maximum), the Slope and Half-Area include the information from 9 bands of the Hyperion sensor between 1.69-1.75 µm. The shape-based parameters, therefore, represent more averaged spectral information, which might be more suitable to estimate gypsum from lower SNR sensors like the Hyperion. Compared to the airborne measurements the Hyperion satellite sensor can register much less

irradiance and has a greater atmospheric pathway. The scene used in this study was also taken under less favourable acquisition conditions, e.g. 11° lower sun elevation and a 13° off nadir observation angle, which can have significant influence on data quality (F. A. Kruse, Boardman, Huntington, Mason, & Quigley, 2002; Mielke, Muedi, et al., 2016).

The prediction models based on the airborne HySpex data in general have the highest performances and the predictions vs. measured regression is much closer and parallel to the 1:1 line, and with high data quality, the NDGI parameter performs best. The models based on the spaceborne Hyperion and EnMAP data seem to overestimate gypsum content of low gypsum samples, while underestimating high gypsum samples. Although the salt pan surface is rather homogeneous on a small scale and changes are more gradual, it is possible that spatial effects contribute to the difference in model accuracy between air- and spaceborne data. The lower ground sampling distance of the spaceborne sensors (30 m) may include more mixed surfaces compared to the ground truth samples, which could contribute to the under- and overestimation of the gypsum content in the Hyperion and EnMAP gypsum models, whereas the airborne HySpex data matches the spatial ground sampling scheme more closely. The largest variations in model accuracy across sensors has to be attributed to different data quality and preprocessing.

The Hyperion sensor is also heavily affected by vertical stripes, which appear in the image along the direction of the push-broom acquisition resulting in false gypsum estimations. These radiometric artefacts also called “streaks” are often pronounced in the SWIR channels, where the incident energy and SNR is low (Jupp, 2001), which causes even small relative errors in miscalibration to have strong effects on the radiometry (Smara, 2015). No striping artefacts were observed for the estimations derived from the EnMAP dataset.

Another source of uncertainty may derive from the different data acquisition dates. Although only samples of surfaces in comparable physical conditions were used for validation, some changes to soil surface mineralogy between acquisition dates cannot be excluded. A very considerable difference between data acquisition is observed in the North Eastern part of the salt pan. In the Hyperion acquisition of 2014, no significant gypsum is mapped, whereas the HySpex airborne data of 2015 show 40-80% gypsum content. This area is located close to an ephemeral inflow channel to the salt pan (Milewski et al., 2017) that may have been active in the wet season between the data acquisition and caused a rapid and significant surface change by material transport. While this drastic change does not affect the model validation, as no ground truth sample from its vicinity is included in the validation data set, more subtle and less obvious changes may have occurred in the

southern pan margin, where most of the samples used for validation were collected. However, the pan margin is relative stable in the long term compared to the rest of the test site, as demonstrated in (Milewski et al., 2017).

In this study soils with a broad range of gypsum content are evaluated (0~85%) for gypsum estimation. The gypsum estimation of samples with zero to lower gypsum content (0~15%) have the tendency of being overestimated already by the laboratory models, which also translates to the remote sensing scale, whereas the models in general are most accurate in the mid-range (30-60%) of gypsum content. The results indicate that the presented approach is most suited for highly gypsiferous soils, e.g. for the Monegros agricultural area in Northeast Spain, where grain farming plots have 20 to 90% gypsum in the upper soil horizon (C. Castañeda, Mendez, Herrero, & Betran, 2010) and less accurate for lower gypsum soils. However, in only slightly gypsum affected soils gypsum tends to concentrate at the soil surface due to evaporation and precipitate processes and the relative high solubility of gypsum (Funakawa, Suzuki, Karbozova, Kosaki, & Ishida, 2000), thus exposing higher gypsum accumulations to optical remote sensing analysis.

5. Conclusion

Soils and sediments in arid regions can be strongly affected by the accumulation of the evaporite mineral gypsum. With the potential of regular monitoring through future hyperspectral satellite missions, soil quality studies would benefit from robust approaches that can estimate the abundance of gypsum in top-soils and are transferable and repeatable. Hyperspectral remote sensing has already demonstrated the potential to determine quantitative estimates of several soil components, but it has never been tested for the assessment of gypsum. This paper demonstrates the potential of the 1.75 µm absorption feature to be used as a surrogate for gypsum determination. This feature is found to be the most suitable for soil applications as it avoids the confusion with clay mineral absorption features at 2.2 µm as well as the increasing noise at the higher SWIR bands. However, due to its proximity to atmospheric water vapour absorption the parametrisation of the 1.75 mm gypsum feature was found to be critical for the accuracy of the quantification. For this, the spectral parameters Normalized Differenced Gypsum Index (NDGI), Slope, and Half-Area and Continuum Removed Absorption Depth (CRAD) were tested. Gypsum prediction functions were built based on laboratory spectral reflectance spectra and mineralogical ground truth data acquired over the Omongwa salt pan, Namibia. Best laboratory models performances were achieved using the NDGI and CRAD parameters ($R^2 = 0.84$ for NDGI and $R^2 = 0.86$ for CRAD). Subsequently, the established gypsum prediction functions were applied to spaceborne Hyperion, airborne HySpex, and simulated spaceborne EnMAP imagery from the test site.

Validation of the results with ground-truth data shows that the 1.75 µm spectral parameters are able to predict gypsum content with variable performances depending on sensors used and spectral parameters used. For most applications, the NDGI is recommended for use due to its robustness regarding minimalizing the influence of the neighbouring atmospheric absorption, while still being sensitive to gypsum variability. Also, the Slope and Half-Area parameters provide medium to good model performances and possibly are favourable for lower SNR data. The CRAD parameter is found to be ideal under laboratory conditions but is not suitable for remote sensing analysis due to the proximity of the continuum endpoint definition to the atmospheric water vapour absorption.

In general, this paper shows a new application for gypsum distribution mapping and abundance determination with the use of the 1.75 µm absorption feature and a robust parametrisation by the NDGI, which is independent of scene specific endmember definitions and provides reasonable results from imagery of current and future hyperspectral sensors.

Acknowledgments: This work was funded by the German Federal Ministry of Education and Research (BMBF) as part of the joint project “GeoArchives—Signals of Climate and Landscape Change preserved in Southern African GeoArchives” (No. 03G0838A) within the “SPACES Program—Science Partnerships for the Assessment of Complex Earth System Processes” research initiative. Project partners from GFZ, TUM and SaM are gratefully acknowledged for intensive joint field works and science discussions. Additionally, we wish to thank Robert Behling and Daniel Berger for help with the field work, Daniel Berger for support with the XRD analysis, as well as Hartmut Liep and Marina Ospald for sample preparation. The authors also thank Holger Eichstaedt, Klaus-Dieter Hanemann and the DIMAP team for their investment in a successful airborne survey, Karl Segl for performing the EnMAP image simulation and the USGS and NASA for providing Hyperion data, especially Stuart Frye and the EO-1 Science Team for support with Hyperion dataset acquisition.

Chapter IV - Analyses of Namibian Seasonal Salt Pan Crust Dynamics and Climatic Drivers Using Landsat 8 Time-Series and Ground Data

This is the final manuscript submitted as:

Milewski, R., Chabrillat, S., Bookhagen, B. (2020). Analyses of Namibian Seasonal Salt Pan Crust Dynamics and Climatic Drivers Using Landsat 8 Time-Series and Ground Data. Remote Sensing, 2020, 12(3), 474. https://doi.org/10.3390/rs12030474

Received: 31 December 2019 / Accepted: 28 January 2020 / Published: 3 February 2020

Abstract

Salt pans are highly dynamic environments that are difficult to study by in-situ and conventional methods because of their harsh climatic conditions and large spatial areas. Remote sensing can help to elucidate their environmental dynamics and provide important constraints on their sedimentological, mineralogical, and hydrological evolution. This study utilizes spaceborne multitemporal multispectral optical data combined with spectral endmembers to document spatial distribution of surface crust types over time on the Omongwa Pan located in the Namibian Kalahari. For this purpose, 49 surface samples have been collected for spectral and mineralogical characterization during three field campaigns (2014-2016) reflecting different seasons and surface conditions of the salt pan. An approach was developed to allow the spatio-temporal analysis of the salt pan crust dynamic in a dense time-series consisting of 77 Landsat 8 cloud-free scenes between 2014 and 2017, covering at least three major wet-dry cycles. The Sequential Maximum Angle Convex Cone (SMACC) extraction method was used to derive image endmembers from the Landsat time-series stack. Evaluation of the extracted endmember set revealed that the multispectral data allowed the differentiation of four endmembers associated with mineralogical mixtures of the crust's composition in dry conditions and three endmembers associated with flooded or muddy pan conditions. The dry crust endmember spectra have been identified in relation to Visible, Near-Infrared and Short-Wave Infrared (VNIR-SWIR) spectroscopy and X-ray diffraction (XRD) analyses of the collected surface samples. According these results the spectral endmembers are interpreted as efflorescent halite crust, mixed halite-gypsum crust, mixed calcite quartz sepiolite crust, and gypsum crust. For each Landsat scene the spatial distribution of these crust types was mapped with the Spectral Angle Mapper (SAM) method and significant spatio-temporal dynamic of the major surface crust types were observed. Further, the surface crust dynamic was analysed in comparison with the pan's moisture regime and other climatic parameters. The results show that the crust dynamic is mainly driven by flooding events in the wet season, but it is also influenced by temperature and aeolian activity in the dry season. The approach utilized in this study combines the advantages of multitemporal satellite data for temporal event characterization with advantages from hyperspectral methods for the image and ground data analyses that allow improved mineralogical differentiation and characterization.

1. Introduction

Salt pan evaporite surfaces are common features in arid regions where closed drainage basins and high evaporation rates favour the development of crusted surfaces mainly composed of evaporite minerals (James K. Crowley & Hook, 1996). Although globally these landforms occupy a limited proportion of the dryland area, they can appear numerous in certain environmental settings, e.g. along palaeodrainage lines or in interdune spaces. In parts of Namibia and Southern Africa, salt pans attain densities of up to 1.14 pans/km^2 (Goudie & Thomas, 1985) and regionally occupy 20% of the surface area (Goudie & Wells, 1995). The surface crust of such salt pans are highly dynamic sedimentary features affected by seasonal-to interannual changes in rainfall, temperature, and wind ablation (Smoot & Lowenstein, 1991).

Such salt pan environments have been recognized as a significant sources of mineral dust in arid regions (Prospero et al., 2002; Washington et al., 2003). The importance of their dust emissions is illustrated in studies from the western United States (Frie, Dingle, Ying, & Bahreini, 2017; Reynolds et al., 2007), Australia (Baddock, Bullard, & Bryant, 2009; Chappell, Strong, McTainsh, & Leys, 2007), central Asia (Ge, Abuduwaili, Ma, Wu, & Liu, 2016; Singer, Zobeck, Poberezsky, & Argaman, 2003), as well as north-central and southern Africa (Robert G Bryant, 2003; Robert G. Bryant, Bigg, Mahowald, Eckardt, & Ross, 2007; Frank D. Eckardt, Bryant, McCulloch, Spiro, & Wood, 2008; Todd et al., 2007; Vickery et al., 2013). The compositions of dust from these sources can have effects on the climate (Pratt et al., 2010), the degradation of groundwater (Wood & Sanford, 1995), soil and ocean fertilization (A. Bhattachan, D'Odorico, & Okin, 2015), as well as human (Plumlee & Ziegler, 2003) and ecosystem health (Field et al., 2010). Dust type and emissivity are related to the mineralogical and physical crust composition (Buck et al., 2011; Mees & Singer, 2006; Reynolds et al., 2007). The advances in understanding of these dust sources and for modelling dust emissions depend on the characterisation of the salt pan surface over time (Katra & Lancaster, 2008).

Compared to the surrounding Kalahari sands salt pans also contain a significant amount of carbon and can function as a sink or source, with its behaviour mainly coupled the flooding regime (A. D. Thomas et al. 2014). The pan sediments also archive to past environmental changes and can be used to derive palaeoenvironmental conditions (Steffi Genderjahn et al., 2017; M. W. Telfer, Thomas, Parker, Walkington, & Finch, 2009), but insights on the current surface dynamic and its variability are necessary to achieve this (Robert G. Bryant, 1996). Some salt pans e.g. in the United States or the South American Puna plateau are also renowned for economically relevant mineral

resources, like boron or lithium rich brines and evaporite minerals (Godfrey et al., 2013; Reath & Ramsey, 2013).

However, the ability to study salt pan surfaces with traditional field methods is limited by their large aerial extent and difficult access in many parts of the world, as well as by episodic surface flooding (Robert Gavin Bryant, 1993; Ghrefat & Goodell, 2011). Remote sensing has been used to overcome these problems with its potential to cover large areas and to provide multitemporal observations. A number of studies have applied different remote sensing techniques to study playas and have demonstrated the usefulness of optical sensors in the Visible Near-Infrared and Short-Wave Infrared (VNIR-SWIR) spectral region (400-2500 nm) for analysing the pan surface properties. E.g. (J.K. Crowley, 1993) showed in particular the potential value of high spectral resolution imagery as a tool for mapping playa evaporates in Death Valley using airborne hyperspectral AVIRIS data and (Kodikara, 2009) demonstrated the possibility of characterizing evaporate mineralogy and associated sediments in a salt pans using space-borne Hyperion data. Whereas hyperspectral remote sensing allows for an improved discrimination of the crusts mineralogy, which is recommended for complex evaporite mineral assemblages (Hubbard & Crowley, 2005), it currently lacks the temporal resolution needed for the analyses and monitoring of the highly dynamic processes of salt pan environments. Some studies demonstrated that it is possible to derive a number of useful mineralogical crust types (e.g. gypsum, carbonate, quartz and halite) for the classification of playa surface even with the broadband multispectral data, e.g. from Landsat 7 ETM (Epema, 1992, p. 2014; J. Li et al., 2014) or Landsat 8 OLI sensor (Flahaut et al., 2017). Nevertheless, a direct mineralogical characterization is not possible. A comparison study showed that Landsat data are able to identify general mineralogical land cover classes and produce similar mapping results compared to high spectral resolution spaceborne Hyperion and airborne AVIRIS data when linked to ground high-spectral resolution data. They point out that much of the additional information gained by hyperspectral data mostly account for variations in texture and moisture content opposed to mineral compositional variations (Ghrefat & Goodell, 2011). The main advantages of multispectral data for salt pan monitoring is that they are collected at a much higher temporal resolution compared to hyperspectral data and can cover larger areas. Newer systems like the Sentinel-2 satellites also provide higher spatial resolution of 10 m or less. This repeated coverage of such systems enables seasonal or even sub-monthly update of the surface conditions, which is especially useful for understanding the evaporite system dynamic and its link to climate drivers.

The scope of this study is to advance on the remote sensing analyses and process understanding of a highly dynamic salt pan in Namibia, based on the combination of multispectral remote sensing with ground-truth spectroscopic and mineralogical data, associated with the use of methods developed for hyperspectral remote sensing. In particular, we aim at 1) investigating the potential of a dense time-series of multispectral Landsat 8 acquisitions to differentiate surface crust types and map their development over multiple seasons, supported by VNIR-SWIR spectroscopy and XRD analysis for mineralogical interpretation; 2) the assessment of climate controls on crust formation. For this purpose, the influence of surface flooding, air temperature, as well as wind speed on the crust development is discussed. To the authors' knowledge this is the first study that utilised dense remote sensing time-series for the mineralogical interpretation of salt pan surface crusts, allowing for the analyses of the temporal evolution of surface spatial changes in a highly dynamic environment responding to local climatic conditions.

2. Study Area

2.1. Regional setting

The object of investigation in this study is the Omongwa salt pan, located in eastern Namibia near Aminuis, ~260 km south-east of Windhoek (**Figure 28**). The object of investigation in this study is the Omongwa salt pan, located in the south western Kalahari, approximately 260 km south-east of Windhoek, Namibia (Figure 1). The Omongwa salt pan has about an extent of 3 by 5 km, which makes it the largest in a group of regional pans that developed in calcretes of a palaeodrainage system. At the test site seasonal to ephemeral inundation events and subsequent drying and buildup of evaporite-rich sediments have been observed (Mees, 1999; Mees & Van Ranst, 2011).

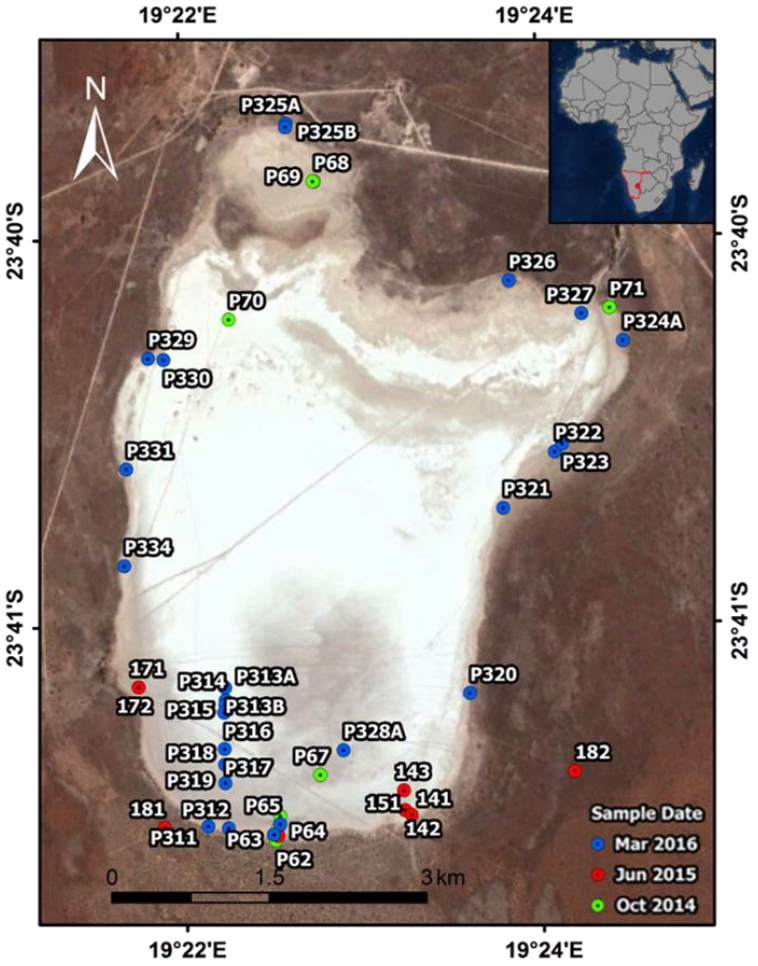

Figure 28. Omongwa pan test site and locations of surface samples (Basemap source: DigitalGlobe RGB image, September 2013, provided by Google Inc. (Mountain View, CA, USA)).

The mean annual rainfall of this area is 200–250 mm recorded for the period of 1982–2002 with high monthly, seasonal, and interannual variations and a mean annual temperature of about 21°C. The potential evapotranspiration (ETP) is of above 3000 mm for the region a, with a maximum in July and August, where the maximum temperature can reach 48 °C. With a precipitation to potential evaporation ratio (P/ETP) of about 0.08 it is classified as arid close to hyper-arid zone (Atlas of Namibia Project 2002) and classifies as BWh climate after the Köppen scheme (Köppen and Geiger 1930). The precipitation is highly seasonal with over 80% of the average yearly rainfall in the wet season from November to April (**Figure 29**). The surface temperature can rise above 40° C in the summer months and falls below the freezing point during the winter nights. The interannual precipitation variation is very high, resulting in occasional draught years with down to ~40% of the average amount (Atlas of Namibia Project 2002).

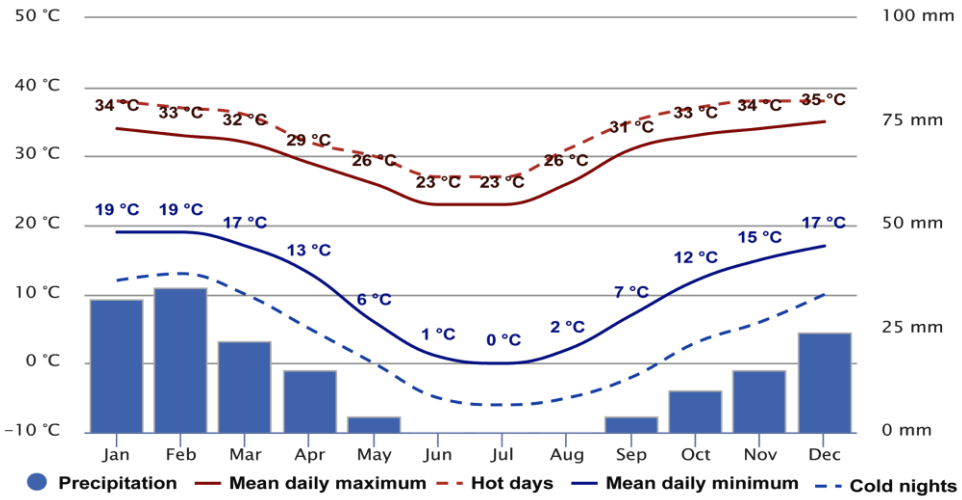

Figure 29. 30-year average temperatures and precipitation in the Aminuis region based on global NOAA Environmental Modeling System (NEMS) weather model with ~30 km resolution.

The topography of the salt pan is very flat with a mean elevation of ~1200 m above sea level. The surrounding Kalahari landscape is characterized by an undulating linear dune system typically in a NW-SE direction (as shaped by the prevailing winds) with elevation magnitudes of ~1-3 m between dune crest and interdune valley. South of the pan a lunette dune rises up to ~50 m above the pan floor level (Milewski, Chabrillat, and Behling 2017). A borehole transect of F. Mees (Mees 1999), recent sedimentary analysis by Schuller et al. (2018), as well as a previous remote sensing study by Milewski et al. (2017) provide detailed sedimentological and mineralogical description of the pan surface and sub-surface sediments. The upper part of the pan deposits are dominated by the sandy material that transitions to silt dominated grains in the first 5-10 cm (Schuller et al. 2018). This sedimentary unit contains a mixture dominated by the evaporite minerals halite, gypsum and calcite with minor content of clay and mica minerals sepiolite, muscovite, and smectite (Mees 1999; Milewski, Chabrillat, and Behling 2017). The lower units have a complex sedimentary structure that consist of a quartz dominated silicate matrix with distributed evaporite minerals that are highly concentrated along desiccation cracks and occur together with hydromorphic features. In the central pan area the calcite rich bedrock is met in a depth of 3 m below the pan surface (Mees 1999). The modern surface is mostly dry throughout the year except when surface flooding by seasonal rainfall turns the pan or parts of it into a shallow lake. Surface runoff from the surrounding savannah landscape is very minor due to restriction by lateral longitudinal dunes and a lunette dune at the southern pan margin (Milewski, Chabrillat, and Behling 2017; Lancaster 1986). At some locations small inflows channels locally impact the pan's surface hydrology and fluvial sediment influx. Most significant is an inflow channel located at the north-eastern pan margin that forms a

small drainage line that was dammed up into a small man-made water retention basin, from which the runoff occasionally drains into the pan and flows along the northern pan margin. Due to the low permeability of the calcareous mudstone, the pan deposits are likely to sustain a locally perched groundwater table that fluctuate between 25 cm and 150 cm below the pan surface (Mees 1999).

2.2 Seasonal surface dynamic

A general model for the process dynamic of salt pans and its effect on their surface composition is provided by the saline pan cycle (Lowenstein & Hardie, 1985). It describes that the episodic formation and dissolution of surface crust evaporites follows a cycle of flooding, evaporation, and desiccation of the playa surface (Chivas, 2007; Lowenstein & Hardie, 1985). These pan cycles are mainly driven by the surface water balance that effect evaporite sediment deposition and dissolution (Bowen et al., 2017; Warren, 2016), but are also influenced by air temperature, humidity and wind regime (Lowenstein & Hardie, 1985). During the flooding stage of the saline pan cycle a shallow, brackish lake is formed. At the Omongwa pan shallow saline ponds cover parts of the surface area episodically in the wet season from December to May (**Figure 30a**).

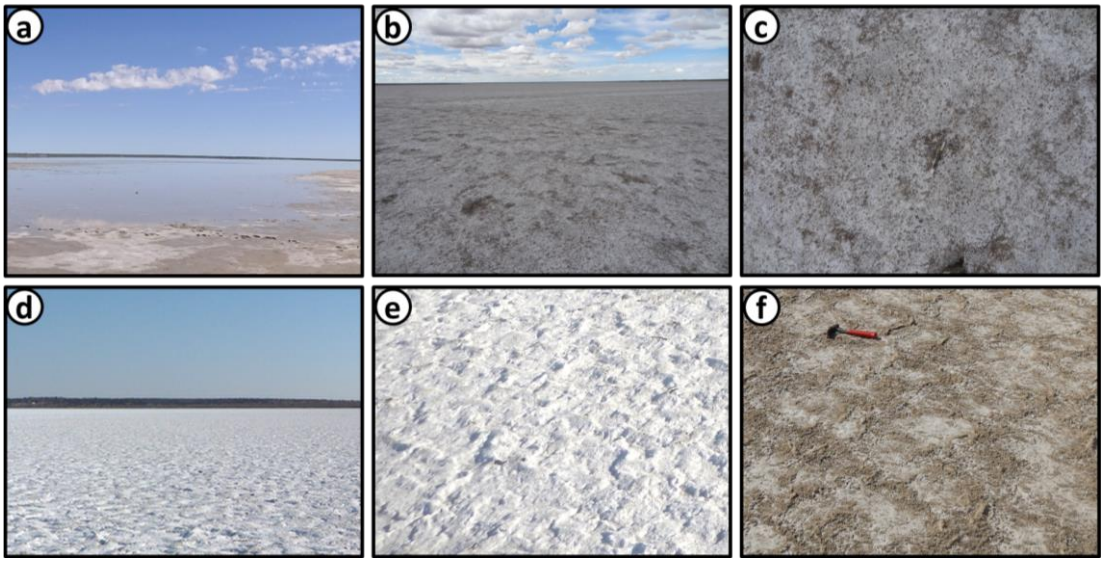

Figure 30. Field photos of the Omongwa pan surface in different stages of the saline pan cycle: (a) during a flooding event; (b) and (c) first thin crust formation shortly after evaporation of surface water; (d) and (e) thick efflorescent salt crust of the desiccation stage; (f) deflated surface of the late dry season.

In playa environments these surface waters commonly originate from meteoric water that falls directly onto the surface, but can also result from perched shallow saline groundwater. The undersaturated surface water dissolves the evaporites of the surface crust and increases the salinity

of the brine (Bowen et al., 2017). With decreasing rainfall the surface brine evaporates and a thin salt crust begins to form atop of moist muddy sediments (**Figure 30b** and **c**). Under persistent dry conditions the desiccation stage of the pan cycle is reached and the crust thickens through capillary evaporation of the shallow saline groundwater (**Figure 30d** and **e**). Morphological features such as salt blisters and irregular to polygonal pressure ridges are formed by the continuous halite crystallization and diurnal expansion / contraction cycles of the surface crust (Melvin, 1991). In the late dry season between August and October a halite deflated surface is observed (**Figure 30f**). In this period of prolonged aridity the groundwater table of the pan continues to fall and a concurrent increase in aeolian activity may remove the upper surface layers by deflating the efflorescent halite crust. Although this stage is characterised by a net surface deflation (Chivas, 2007), windblown material can also be introduced from the pan surroundings and adhered by hygroscopic films of the pan surface (Smoot & Castens-Seidell, 1994).

A previous remote sensing-based study on the Omongwa salt pan could identify and spatially map major mineralogical crust constituents (halite, gypsum, sepiolite and calcite) using EO-1 Hyperion hyperspectral imagery. Also, multitemporal remote sensing analyses showed that the Omongwa pan surface crusts are spatially heterogeneous and highly dynamic during the last 30 years (Milewski, Chabrillat, and Behling 2017). However, only the magnitude of change was characterized and no specific characterization on the type or direction of change was derived.

3. Material and Methods

3.1. Field and Laboratory Analysis

Three field campaigns for surface characterisation and sampling took place in October 2014, June 2015 and March 2016, which respectively represent the end and beginning of the dry season, as well as the end of the wet season. A total of 49 top surface crust (<2 cm) samples were collected in relative homogeneous areas. These samples were composed of 5 to 10 sub-samples collected at random locations within a 5 m wide square around the centre point for each site of interest. Mineralogical characterization was carried out using a PANalytical Empyrean powder X-ray diffractometer (XRD) with a theta-theta-goniometer, Cu-Kα radiation (λ = 0.15418 nm), automatic divergent and anti-scatter slits and a PIXcel3D detector. Diffraction data were recorded from 4.5° to 85° 2Θ with a step-size of 0.0131 and a step time of 60 s. The generator settings were 40 kV and 40 mA. All samples were crushed and powdered to a grain size of <62 micron. These samples were used for the qualitative and quantitative mineral analysis. A few samples were also powdered to

<10 micron, but no strong differences in intensities were observed. The qualitative phase composition was determined using the software DIFFRAC.EVA (Bruker), and the quantitative mineralogical composition of the samples (in weight %) was calculated using a Rietveld based method implemented in the program AutoQuan (GE SEIFERT; Taut, Kleeberg, and Bergmann 1998). Spectral properties of the field samples were measured in the laboratory under controlled environmental and illumination conditions simulating spaceborne observations (sensor nadir viewing, light source azimuth 35°) using an ASD (Analytical Spectral Devices) FieldSpec 3 spectroradiometer, covering the VNIR-SWIR spectral range with 3 to 10 nm spectral resolution and 2151 wavelengths resampled to 1 nm (ASD Inc., 2015). A spectral library associated with the optical signatures of the 49 soil samples were created using ENVI 5.3 (Harris Geospatial Solutions, 2015) after correcting the detector offset and averaging the 5 measurements per target.

3.2. Remote Sensing Analysis

For this study all available Landsat 8 Operational Land Imager (OLI) images of the study area at World Reference System-2 path/row 176/76 were acquired through the Google Earth Engine public data catalogue (Gorelick et al., 2017) that host the extensive USGS Tier 1 and 2 Landsat Collection. The OLI sensor has seven reflective bands (Coastal Blue: 443 nm, Blue: 482 nm, Green: 562 nm, Red: 655 nm, NIR: 865 nm, SWIR I: 1609 nm, SWIR II: 2201 nm) at a spatial resolution of 30 m (USGS, 2016). The time-series covers ~4.5 years (04/2013-10/2017) with a temporal resolution of 16 days. From the total 94 scenes 17 had to be excluded due to cloud cover over the salt pan. The cloud screening was manually performed as the automatic cloud detection CFMask resulted in many false positives, likely caused by detection issues over bright targets such as salt lakes (USGS, 2017). The level-2 data are pre-processed to surface reflectance (SR) with version 4.2 of the Landsat 8 Surface Reflectance Code (USGS, 2017) to minimize atmospheric signals for analysis of surface reflectance and spatially constraint to focus on the salt pan area.

Two established spectral analysis techniques are applied for the identification and mapping of the crust endmembers in the Landsat time-series of the Omongwa pan. First, spectral endmembers of the surface crust types are identified through the Sequential Maximum Angle Convex Cone (SMACC) algorithm (Gruninger, Ratkowski, & Hoke, 2004). Then the defined set of crust endmembers is used to derive the distribution of each crust type from the Landsat time-series by applying Spectral Angle Mapper (SAM) classification (F. Kruse et al., 1993). Both techniques have been used in a wide range of mineralogical and soil application(Shrestha et al., 2005; Zazi, Boutaleb, & Guettouche, 2017; Xiya

Zhang & Li, 2014), including mineralogical mapping of salt pan environments (Katra & Lancaster, 2008).

3.2.1 Salt Pan Crust Type Endmember Definition

The crust endmembers are identified by applying the SMACC method on the Landsat time-series. The SMACC algorithm uses a convex cone model (also known as Residual Minimization) with these constraints to identify image endmember spectra. Extreme points are used to determine a convex cone, which defines the first endmember. A constrained oblique projection is then applied to the existing cone to derive the next endmember. The cone is increased to include the new endmember. The process is repeated until a projection derives an endmember that already exists within the convex cone or lies in a specified tolerance to an already found endmember (Gruninger et al., 2004). The SMACC endmember extraction method implemented in ENVI 5.4 (Harris Geospatial Solutions, 2014) is applied on a generated pseudo image that contains the spectral information of all pixels of the pan surface, which allows the algorithm to derive the endmembers that are most descriptive for the spectral variability of the entire image time-series. The method is run with the constraint that the sum of the fraction of each found endmember does not exceed unity, so that a pixel cannot be more than 100% filled. The default coalesce value of a spectral angle of 0.1 is used to limit the extraction of very similar endmembers. The derived set of endmembers is then compared to the spectral measurements of the collected field samples to allow a thematic and mineralogical interpretation. For this comparison the laboratory ASD spectra measurements of the field samples are resampled to match the spectral characteristics of the multispectral OLI sensor and the reference spectra that most closely match the crust types are identified.

3.2.2 Salt Pan Crust Type Mapping and Validation

In the next step, set of crust endmembers established by the SMACC method is used to derive the distribution of each crust type from the Landsat time-series by applying Spectral Angle Mapper (SAM) classification, which was implemented to run in the Google Earth Engine (Gorelick et al., 2017). The implementation of the SAM function to the Google Earth Engine allows the extension of the time-series to new acquisitions as soon as they enter the collection without the need for local download or processing of the data, which is useful for fast and regular monitoring purposes. SAM compares the angle between a reference spectrum vector (the identified crust types) and each pixel vector in n-dimensional space, where smaller angles represent closer matches to the reference spectrum and pixels further away than the specified maximum angle threshold in radians are not classified (F. Kruse et al., 1993). SAM is an solid and rapid method for mapping the spectral similarity

of image spectra to reference spectra with a number of advantages over other commonly used spectral-based classifiers: (1) it is not affected by linear offsets, which makes it robust against differences in solar illumination and observation geometry (Tavin et al., 2008), because the angle between the reference and test spectra is the same regardless of their length (F. Kruse et al., 1993) (2) it represses the influence of shading effects to accentuate the target reflectance characteristics (Girouard, Bannari, El Harti, & Desrochers, 2004) and (3) other than spectral unmixing based methods, it does not require all endmembers in the scene to be identified (Jollineau & Howarth, 2008). The threshold angle for SAM classification is set to the default of 0.1 rad and any pixel that does not match any of the reference vectors within this angle is designated unclassified.

A validation of the extracted endmembers and spatial distribution mapped by the SAM is performed by comparing the result of one specific Landsat test scene to a previously published independent mineralogical mapping of the Omongwa pan that is based on spectral mixture analysis of a hyperspectral Hyperion dataset (Milewski et al., 2017) acquired on the same day as the Landsat test scene. Basic accuracy measures such as producer's and user's accuracy as well as overall accuracy and the kappa coefficient (Congalton & Green, 2008) are computed to assess the Landsat classification with respect to the independent reference.

3.2.3 Dynamic of Omongwa Pan Surface

The analysis of the climate controls on crust formation is performed by estimating the variations in multitemporal crust type mapping, and looking at the influence of surface wetness related to the flooding and desiccation cycles, and the influence of air temperature as well as wind speed on the crust development. For this purpose, the relative areal coverage of each crust type is calculated for each Landsat acquisition, so that a resulting areal abundance value between 0 and 1 is obtained for each crust type and all crust type together with the unclassified (wet/muddy) area sum up to 1. These relative areal coverages of each crust type are then compared with timely available data on derived surface wetness and climatic variables.

The surface wetness is directly derived from each image of the Landsat time-series using Xu's Normalized Difference Water Index (NDWI) (Xu, 2006), a band ratio using the green and first short-wave infrared (SWIR I) band. Xu's version of the NDWI (also termed Modified NDWI) has been successfully used to detect flooded areas from remotely sensed data and mostly outperformed water indices based on different band combinations for land/water differentiation (S. K. Jones et al., 2017; Kelly & Gontz, 2018; W. Li et al., 2013). The NDWI band ratio is dimensionless and mathematically varies from -1 to 1. In general, water surfaces show larger positive values in NDWI,

because they absorb more radiation in the SWIR than the visible range. Values close to 1 are observed over clear water areas (when all radiation of the Short-Wave Infrared is absorbed). Whereas smaller negative values are expected over soils or vegetated areas, because these surface types reflect more in the SWIR than the Green wavelength (Yang, Zhao, Qin, Zhao, & Liang, 2017). However, in a salt pan environment, where partial or shallow flooding frequently occurs the situation is more complex. Therefore, the crust type abundancy is directly compared to the NDWI values as an indicator for surface wetness and only classified as flooded pixel, when a very high threshold (NDWI > 0.6) is reached.

For the evaluation of wind and temperature influences on the pan crust dynamic, the needed climatic parameters are derived from the European Centre for Medium-Range Weather Forecasts' (ECMWF) ERA5 climate model. Modelled climate parameters had to be used, due to a lack of observed meteorological parameters in the vicinity of the study area. The ERA5 dataset is the most recent generation of ECMWF atmospheric reanalyses of the global climate. The model provides hourly estimates of a large number of atmospheric, land and oceanic climate variables with a horizontal resolution of about 31 km at the latitude of the study area. The first segment of the dataset from 2010 to present is already available free to public users, and the whole dataset, which will cover the period from 1979 to present is gradually released over the next years (Hersbach & Dee, 2016). From the dataset the u and v wind components in 10m height as well as temperature in 2m are extracted from the climate model. From the hourly u and v wind components the hourly wind speed is calculated. Hourly wind speed and temperature are then aggregated to monthly means.

4. Results

4.1. Crust-Type Endmember Definition

Seven endmembers were extracted by the Sequential Maximum Angle Convex Cone (SMACC) method based on the spectral variability of the Landsat time-series with a remaining maximum relative error of 0.048. Three of the derived endmembers (blue coloured spectra on **Figure 31**) show reflectances of < 5% in the SWIR band and are related to wet surfaces associated with liquid water, mix water-sediments or very muddy pan sediments.

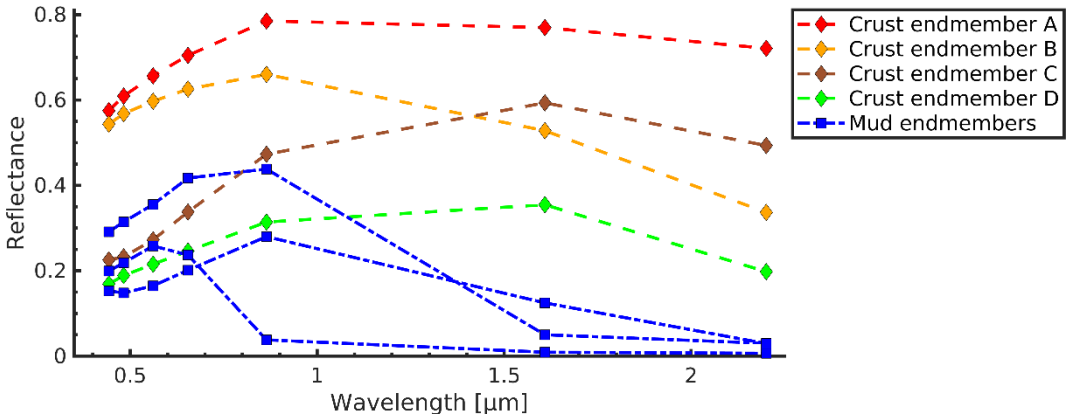

Figure 31. Spectra of dry crust and wet endmembers derived from SMACC analysis.

The wet endmembers were excluded from further analysis as they do not represent a developed surface crust that needs dry conditions. The remaining endmembers (A-D) represent the major surface crust types of the Omongwa salt pan during the time-series. The spectra are mineralogically interpreted through a comparison with the laboratory measured spectra resampled to Landsat OLI bandpass and the XRD results of the collected field samples, as shown in **Figure 32**. The spectrum of class A shows a general high reflectance close to 80% with increased absorption in the visible spectral range. This bright crust endmember is interpreted as a very dry efflorescent salt crust containing mostly halite and other chlorides. These minerals show little to no absorption features in the optical domain except for absorbed water features (J.K. Crowley, 1993; Drake, 1995), which is hidden by atmospheric water vapour absorption and outside of the Landsat band designation. Similar spectral shapes of halite crusts were reported for playa crust in Tunisia (Robert G. Bryant, 1996), Nevada USA (J.K. Crowley, 1993). Crust endmember B is of similar high reflectance as class A in the visible range but drops significantly in the NIR and SWIR bands. The comparison to ASD laboratory spectra shows sulphate related absorption at 1500 nm, 1750 nm and 2200 nm (**Figure 32b**).

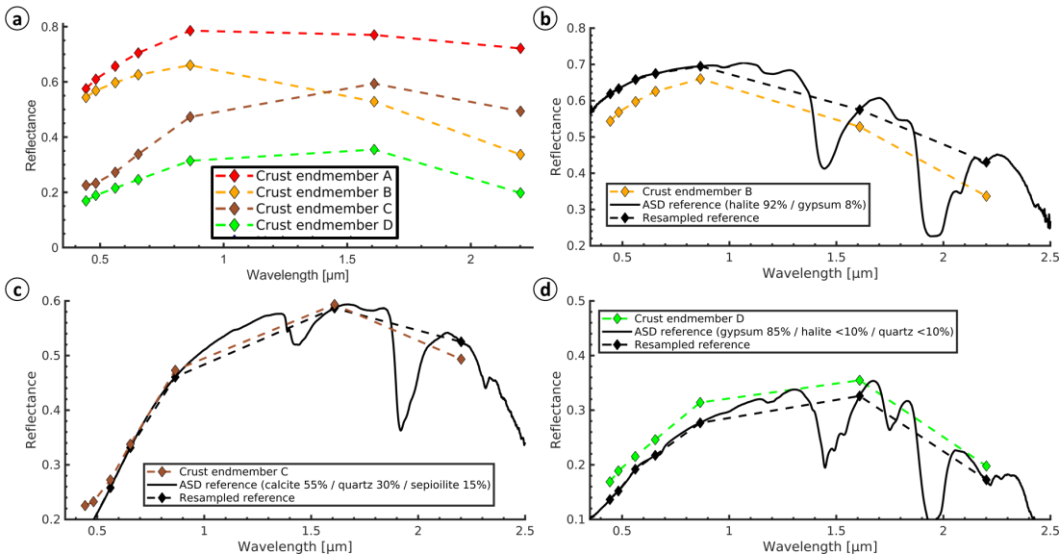

Figure 32. (a) Spectra of crust endmembers derived from SMACC analysis; (b) Endmember B: mixed halite-gypsum crust; (c) Endmember C: mixed calcite-quartz-sepiolite crust; (d) Endmember D: gypsum crust. Plots (b-c) additionally show the laboratory measured spectrum of the field sample with most similar reflectance to the endmember, as well as the mineralogical composition of the sample.

The absorption around 1500 nm is very smooth and does not have the distinct triple absorption of more concentrated gypsum, which is caused by the high halite content (90%) in the mixture in relation to gypsum (>10%) (Fares M. Howari, Goodell, & Miyamoto, 2002). Additionally, the laboratory spectrum shows an absorption feature at 2100 nm, which is likely caused by the presence of thenardite (Na_2SO_4). Thenardite can be formed in room temperature from gypsum in the presents of NaCl-saturated solution (Garrett, 2001). The endmember B spectrum resembles the shape of mixed halite, gypsum crust described by (Chapman et al., 1989) for a playa in the Atacama desert, and thus is interpreted as mixed halite-gypsum crust. The reflectance curve of crust endmember C starts much lower in the visible bands with about 20% reflectance at 500 nm and increases to about 50% in the SWIR I and drops in the SWIR II band. The ASD reference spectrum that best matched the Landsat reflectance shows a distinct absorption feature at ~2300 nm (**Figure 32c**), which is diagnostic for carbonates as well as the sepiolite clay mineral (Hunt et al., 1971). The XRD result confirms the presence of sepiolite with 15% in the calcite dominated sediment (55% calcite content), as well as the large quartz component (30%). This mixed crust type was sampled at the border of the salt pan and represents the allochthone influence of the Kalahari sands that are mostly composed of quartz, as well as the calcite host rock of the pan that outcrops at the pan border and which are known to have sepiolite coatings (Mees & Van Ranst, 2011). Crust

endmember D overall has the lowest reflectance with ~20% in the visible and SWIR II bands and a peak of 35% in the SWIR II (**Figure 32d**). The best matched reference ASD spectrum shows the pronounced absorption triplet around 1500 nm, as well as further weaker features at 1200 nm, 1750 nm and 2200 nm characteristic for gypsum (Fares M. Howari et al., 2002; Khayamim et al., 2015) that are all related to the bending and stretching overtones of the water in the gypsum crystal structure (J.K. Crowley, 1993). The matched field sample has the highest gypsum content (85%) of all collected samples alongside minor halite and quartz components (<10%), and this endmember is thus interpreted as gypsum crust.

4.2. Crust-Type Mapping and Validation

The Landsat SAM classification is validated with a mineralogical mapping result based on a hyperspectral Hyperion image that was acquired on the same day as the Landsat 8 OLI scene (7th of September 2014). For this purpose the quantitative spectral unmixing result of the Omongwa pan published in Milewski et al. (2017) (**Figure 33b**) was discretized to match the SAM crust type classes (**Figure 33c**). Owing to the lower spectral resolution and spectral range of Landsat OLI, the Hyperion calcite/sepiolite crust type cannot be differentiated from the featureless disturbed crust endmember described in Milewski et al. (2017). Consequently, these classes are merged for comparison with Landsat OLI. The mixed halite-gypsum crust is defined where at least 40% of a pixel was unmixed to halite and gypsum in the Hyperion based result. All other pixels were classified according to their dominating mineralogical fraction. In general, the Landsat based SAM classification of that date (**Figure 33d**) agrees very well with the independent mapping based on hyperspectral data (**Figure 33c**). The overall classification accuracy is 90% with the corresponding overall Kappa coefficient of 0.8 (Tab. 1), which demonstrates the very high, substantial agreement of the classification to the reference according to Landis and Koch (1977). The spatial distribution of the classification differences, where the Landsat OLI SAM does not match the independent mapping based on hyperspectral data, are shown in **Figure 33e**. Most mismatched pixels are registered at the class borders, which may be due to the fact that the Hyperion reference scene was geometrically transformed during the processing (Milewski et al., 2017). Respectively the largest errors of omission (28%) as well as commission (27%) are attributed to the mixed halite-gypsum class, which has the largest boundary in relation to its total mapped area.

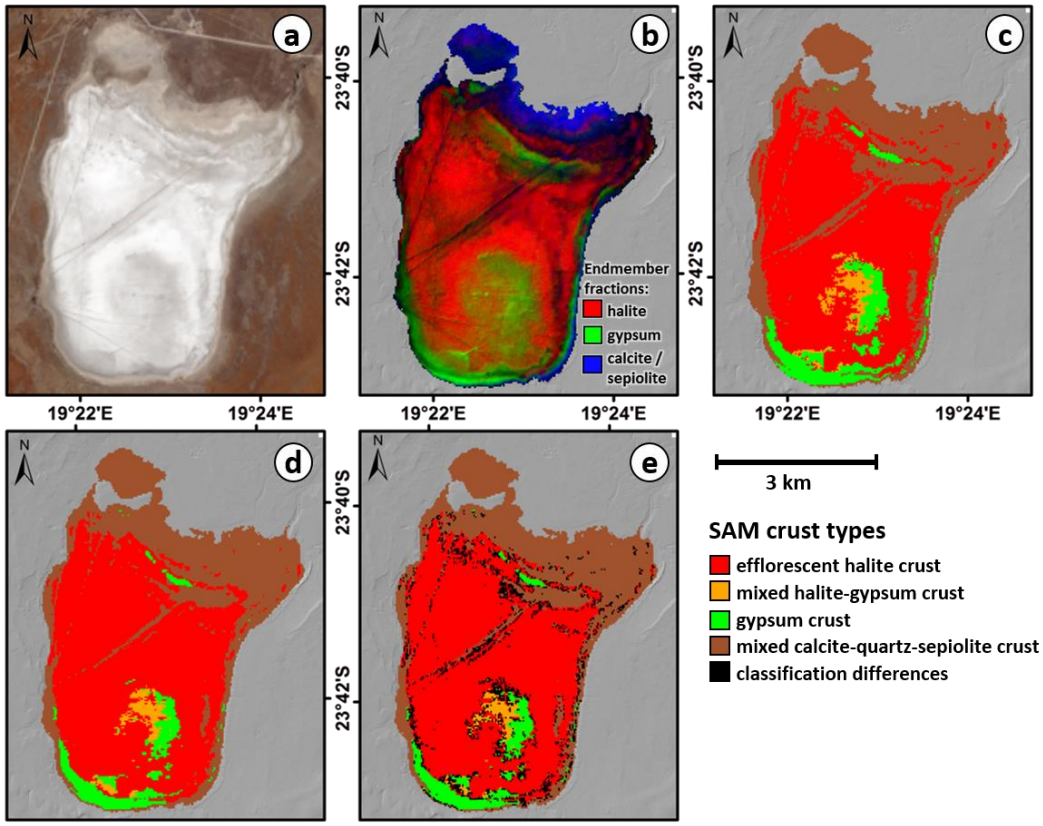

Figure 33. Comparison of Landsat 8 SAM result to classified Hyperion based unmixing of Milewski et al. (2017): a) Landsat RGB image from 09/07/2014; b) Hyperion based mineralogical unmixing of Milewski et al. (2017); c) Reclassified (discretised) mapping based on the Hyperion unmixing; d) Landsat OLI SAM result; e) Map of differences between Landsat OLI and Hyperion based classification.

Table 5 Comparison of crust type mapping between Landsat SAM classes and Hyperion based spectral unmixing of Milewski et al 2017: Producer's accuracy (PA), User's accuracy (UA), Overall Accuracy and Kappa coefficient

SAM crust type		
Efflorescent halite crust	PA (%)	96%
	UA (%)	87%
Gypsum crust	PA (%)	74%
	UA (%)	90%
Mixed halite and gypsum crust	PA (%)	72%
	UA (%)	73%
Quartz, calcite, sepiolite mixed crust	PA (%)	86%
	UA (%)	93%
Overall Accuracy		90%
Kappa		0.8

4.3. Dynamic of Omongwa Pan Surface

Figure 34 shows the multitemporal analyses of the crust type mapping related to surface wetness computed from the cloud-free Landsat time-series from April 2013 to October 2017. In that period, at least three major flooding events are observed, with simultaneously significant seasonal as well as intra-annually variations in the surface crust mineralogy of the salt pan at dry conditions. The most common and longest exposed surface crust type identified is the mixed halite-gypsum crust (in orange in **Figure 34**). This crust type reaches its maximum areal extent (up to 60-80%) in the more moist periods of the year and is the first crust composition that develops after flooding events, which are indicated by increased NDWI. These high NDWI events not only represent surface flooding, but also relative wet pan surface conditions that are spectrally very different compared to the dry crust endmembers. With the exception of the relatively dry year of 2014, each season between 2015-2017 contains at least one wet event with up to 60-80% of the surface area flooded in the period between the end of October and the middle of May. The areas that remain dry during the flooding events are mostly mapped as gypsum crust (green in **Figure 34**) with an aerial coverage that seems to be more or less stable, and increases toward the end of the dry season. With receding surface flooding and in periods between rainfall events the mixed halite-gypsum crust (re-)develops fast in only two to four weeks.

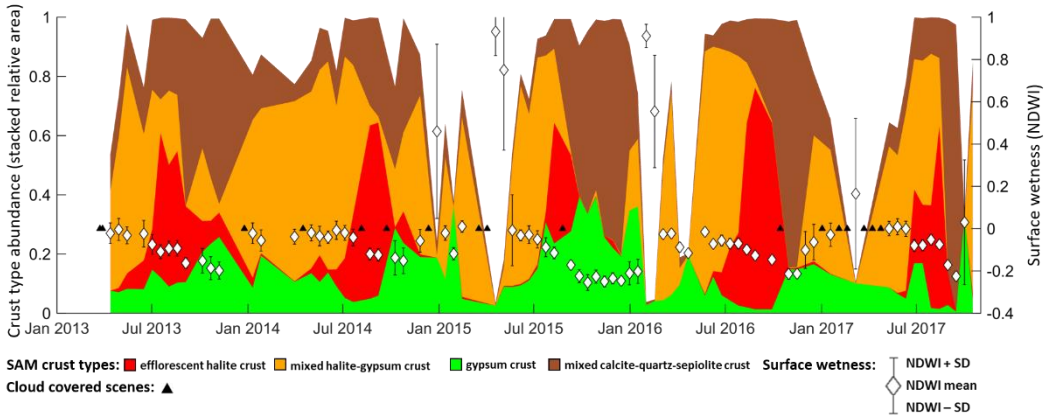

Figure 34. Areal crust type relative abundances (stacked) and surface wetness (NDWI) of the Omongwa pan based on Landsat time-series (2013 – 2017); triangle marker indicate cloud covered scenes.

The analyses show that further into the dry season, between July and September, after several months of dry conditions, the bright efflorescent halite crust appears (red in in **Figure 34**) and covers 40 to 70% of the pan surface area at its peak. In the late dry season between August and October the surface area becomes increasingly classified as mixed calcite-quartz-sepiolite crust (brown **Figure 34**) while the bright efflorescent halite crust disappears. The mixed calcite-quartz-sepiolite crust has the highest variability between the years with the smallest extent of 40% in 2014 and up to 90% in 2017.

5. Discussion

The results show the salt pan surface status following flooding and desiccation events in terms of the seasonal and inter-annual evolution of surface evaporites and surface wetness. The methodology developed allows to interpret the mineralogical endmembers based on Landsat data combined with spectroscopy and mineralogical laboratory analyses, which can thus be used for spatio-temporal analyses of the surface processes of the Omongwa salt pan. The methodology is validated with independent observations from field knowledge and hyperspectral remote sensing that confirms the accuracy of the spectral Landsat identification and the spatial mapping.

5.1 Inter-annual surface flooding-desiccation cycle characterization

For a more detailed yearly analysis of processes observed at the surface of the pan, the exemplary season of 2017 which is characterized by a unique major flooding event in March shown in **Figure 35** including the spatial development of surface crust types in time slices together with the surface wetness and the true-colour images of the pan area. Time slices are selected for their

representativity 3 times during the wet season, and 3 times during the dry season. The first time slice (7th of March) shows the peak of the flooded pan stage, where only the gypsum crust (green) remains at the pan margin and the central parts are completely flooded (**Figure 35a**). In the second time slice from the 10th of May the mixed gypsum-halite crust (orange) has developed at the least moist parts at the pan borders, but the most central parts are still in a more wet state.

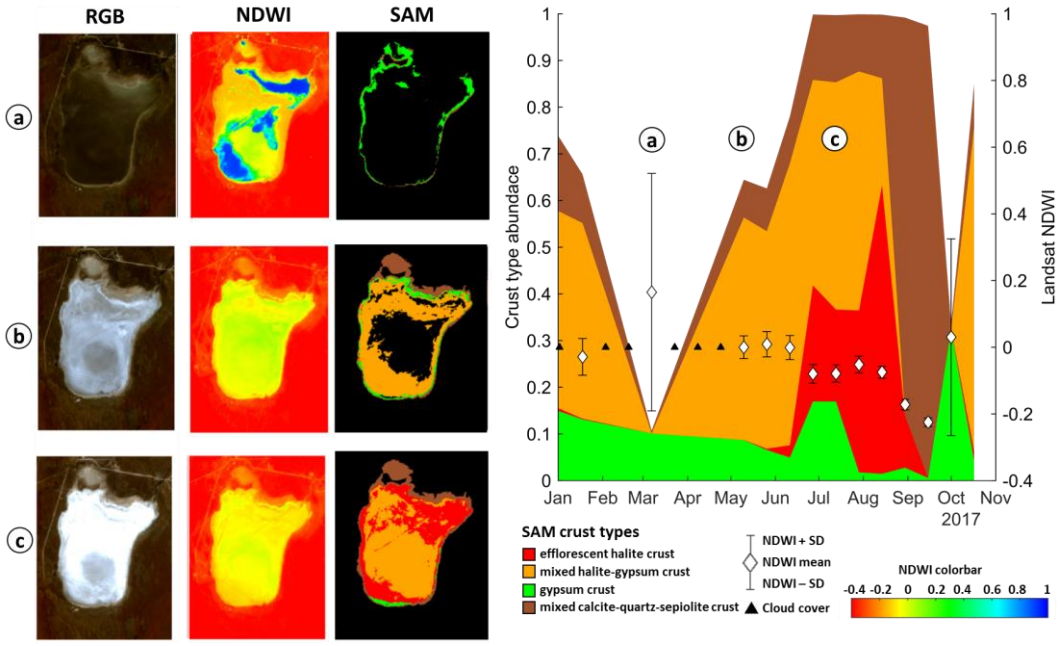

Figure 35. Surface dynamic of the Omongwa pan in 2017. Left: Landsat True colour (RGB), surface wetness (NDWI) and crust type mapping (SAM) of (a) 7 March; (b) 10 May; (c) 29 July.

Figure 35c and **Figure 36a** show the successive transition of the mixed gypsum-halite (orange) to the bright efflorescent halite crust (red) endmember between the end of July and mid-August. All of the pan surface is dry by now as the efflorescent halite crust gradually develops from the pan margin to the more central area. Only ~4weeks later in the time slice of mid-September (**Figure 36b**) almost all of the pan area is mapped as the mixed calcite-quartz-sepiolite crust endmember (brown), the evaporite crust endmembers have disappeared and the pan surface appears less bright. In the last time slice (**Figure 36c**) from the beginning of October the pan is flooded again with only some marginal areas of gypsum crust remain and the next flooding/desiccation cycle begins.

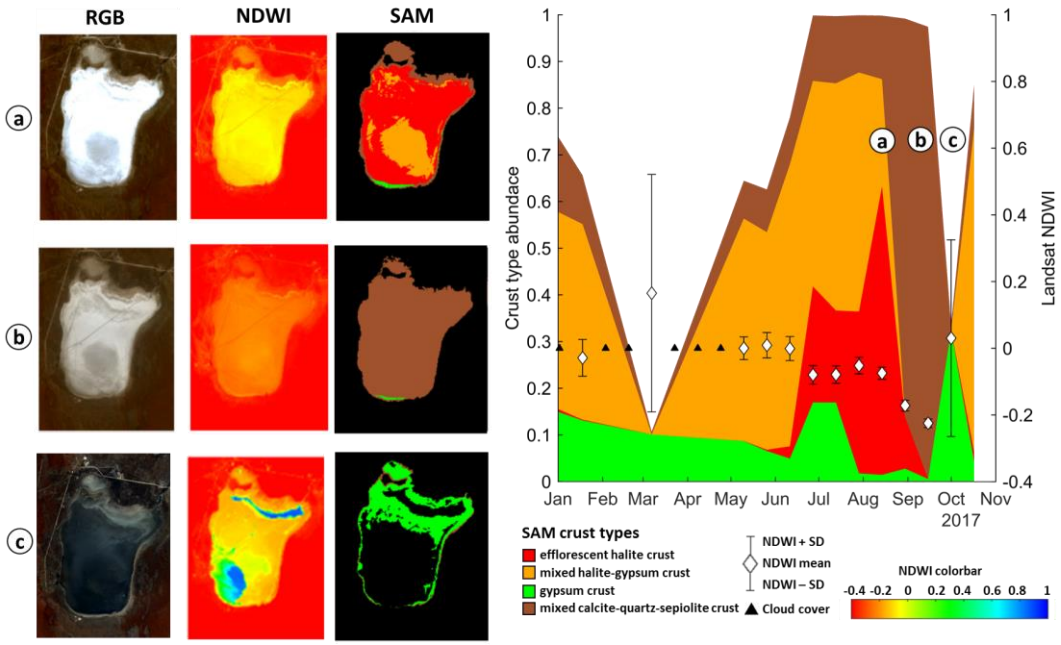

Figure 36. Surface dynamic of the Omongwa pan in 2017. Left: Landsat True colour (RGB), surface wetness (NDWI) and crust type mapping (SAM) of (a) 14 August; (b) 15 September; (c) 1 October.

5.2 Influence of climatic variables on multiannual crust type dynamic

Previous studies on the surface dynamic of evaporite environments suggests that interaction of water and wind are major drivers for the varying surface properties such as crust mineralogy and morphology (Bowen et al., 2017; Millington et al., 1987; Shaw & Bryant, 2011). For the Omongwa salt pan, we evaluated further the seasonal influence of surface flooding, wind speed and temperature on the dynamic of the surface crust over multiple years (**Figure 37**).

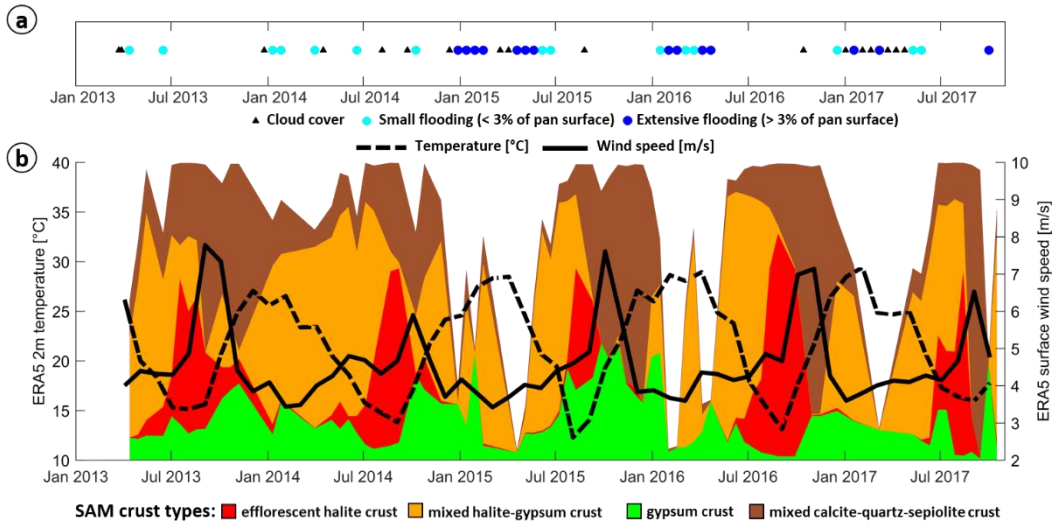

Figure 37. Pan surface dynamic and climatic parameters: (a) flooding dynamic based on surface wetness (NDWI > 0.6); (b) temperature [°C] at 2m and (dashed line) and wind speed [m/s] at 10m (solid line). Climate variables are derived from ERA5 and plotted over the multitemporal crust type areal coverage mapping (scaling is the same as in the previous figures).

In the winter months (December to March) the pan surface dynamic is driven by the occurring rainfall events that dissolve most of the pan's surface crust that either by surface flooding or more temporary ponding associated with very muddy sediments. In the spring/summer month (May to July) as evaporation and mineral crystallisation continue, and less or no rainfall event occur, the muddy pan surface dries out and the desiccation stage is reached. Several extensive flooding events are observed in 2015-2017. In the season of 2014 only minor flooding events occur (**Figure 37a**). However, the development of the crust from mainly mixed calcite-quartz-sepiolite surface to the more evaporite rich halite-gypsum crust is also observed in this year. This indicates that the build-up of mixed halite-gypsum crust after the wet season does not rely on an extensive flooding event to redistribute the salt minerals, but results from the combined effect of evaporation and capillary rise to develop these crusts from subsurface brines. The development of the halite-gypsum crust coincides with the period of increased solar radiation indicated by the higher ambient temperature (**Figure 37b**) that also increases sediment and brine temperature, which leads to higher evaporation rates (Turk, 1970), as well as increased soil water diffusivity (Grant & Bachmann, 2013). The calcareous mudstone layer along the palaeodrainage that lies below the Kalahari sands in this region (Mees, 1999) may also support groundwater flow from the pan surroundings that concentrates at the local pan depression and further promotes capillary rise and subsequent evaporation processes from the shallow groundwater table.

During the winter months the atmospheric conditions are very dry and temperature decreases to the lowest monthly average <15° C in July to September (**Figure 37b**). In this period the pan crust shifts from the mixed halite-gypsum crust to much higher concentration of halite at the surface. This development to a very bright, halite rich surface is observed for each year. The formation of such efflorescent salt crust in the cold winter months can be explained by a wetting process driven by an increase in relative humidity amplified by the hygroscopic nature of halite. Within the pore space of halite rich sediments water vapour already condenses at relative humidity levels that otherwise hinder the occurrence of liquid water in the surrounding environment (Davila et al., 2008). This process is mainly driven by the large temperature oscillations of the diurnal cycle. When the temperature on the pan surface drops during the night (even below the freezing point in winter), the relative humidity of the air increases. At 75% relative humidity the deliquescence point of halite is reached (Greenspan 1977). At that point the amount of moisture absorbed from the air is enough for the dissolution of the hygroscopic salt and the formation of local brines. As the temperature on the salt pan surface increases after sunrise (up to 30°C in winter) the brine that has accumulated during the night will tend to move upwards driven by capillarity and evaporation processes (Artieda et al. 2015). As water migrates towards the surface, the brine becomes successively concentrated and salts are deposited, when their solubility coefficients are exceeded. Carbonates are potentially deposited first, followed by sulphates, and finally halides that form a fresh efflorescent crust on top the more mixed sediment layers (Finstad et al. 2016). A similar process is described for halite efflorescence in saltpans of the hyperarid Atacama Desert (Davila et al. 2008; Wierzchos et al. 2012; Artieda et al. 2015). Once patches purer in NaCl form, they are preferentially wetted during subsequent nights, which leads to a further enrichment and the development of apparent bright salt crust over multiple diurnal cycles (Finstad et al. 2016). **Figure 38** show exemplary daily variation of air temperature and relative humidity in winter at the study site. Immediately after sunset, relative humidity increases with decrease in temperature. Throughout the night and early morning relative humidity reaches the deliquescence humidity point of halite (dotted grey line). Increasing temperatures during the day result in low humidity and increase in evaporation throughout the rest of the day. In the summer months, relative humidity is low (**Figure 38a**) with the exception of rainfall events, in which the air reaches saturation, which explains the lack of formation of halite and is confirmed by the presented results

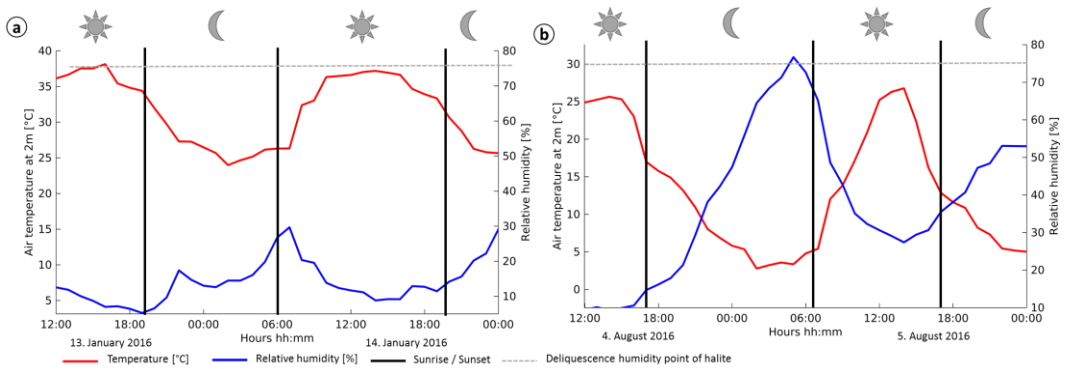

Figure 38. Typical daily variation of temperature and relative humidity in a) summer and b) winter season (data from ERA 5 climate model).

Wind data show strong seasonality, with the strongest winds occurring in the Late Summer Early Autumn month (August to October) in between the end of the dry season and the start of the new wet season (**Figure 38c**). Mean monthly wind velocities of 6-8 m/s are registered in these month, whereas during the rest of the year monthly wind speed averages around 4 m/s. In parallel to the stronger winds more surface area is classified as the mixed calcite-quartz-sepiolite crust endmember and less as bright efflorescent halite crust. This observation in crust developments can have two general causes: (1) the removal of efflorescent halite crust by wind erosion and (2) the accumulation of windblown material originating from the pan surroundings. Wind speed is considered a main driver for dust emission (Csavina et al., 2014; Lu & Shao, 2001), but to initiate particle movement a threshold in shear velocity (a measure of momentum transfer from the wind to the surface) has to be met that exceeds the cohesive force or "binding energy" of the surface particles (King, Etyemezian, Sweeney, Buck, & Nikolich, 2011). The magnitude of this binding energy is highly variable and dependent on the several physical and chemical soil parameters, e.g. particle size, mineralogy, moisture and organic content. Accounting for all these factors has proven very difficult and is generally unrealistic for a predictive model (King et al., 2011; Shao & Lu, 2000). However several studies on salt pan emissivity have gathered empirical data on shear velocity or friction velocities thresholds (u_t) necessary for particle movement in these settings. The lower end of the reported shear velocities thresholds are in the range of 0.3-0.5 m/s (King et al., 2011; Roney & White, 2004; Sweeney, McDonald, & Etyemezian, 2011), but thresholds can also exceed 1.5 m/s for undisturbed clay and salt crusted playa surfaces (Gillette, Adams, Endo, Smith, & Kihl, 1980). The shear velocities at the surface can be estimated from the wind speed data in 10m height using the Prandtl-von Kármán equation (Nickling & Ecclestone, 1981): $u = \frac{u}{6.13 * log\left(\frac{z}{z_0}\right)}$, where u is the wind speed at height z and z_0 is the roughness length for surface open flat terrain (0.03 m) (WMO,

2008). Based on this equation, we calculated that the shear velocity threshold of 0.4 is reached by winds speeds of about 14.5 m/s in 10 m height. **Figure 39** shows the hours per month that exceed this wind speed threshold and enable dust emission. The windiest months are September and October, with wind speeds exceeding 50 hours per month, with the exception of the 2014 season, where less than half of average hours per month are recorded. For this year with significant lower wind speed the endmember fraction of mixed calcite-quartz-sepiolite also covers less of the pan area (only 20% compared to the other years with 60-80% coverage). On the other hand the accumulation of windblown dust particles originating from the pan surrounding is also possible, since moist playas are effective dust traps, where moisture films bind the deposited particles by surface tension (Pye, 2015). Dust particles that settle on a bare, smooth surface are susceptible to re-suspension, which results in no net deposition. However, if the dust cloud passes over a moist ground the particles which fall to the surface may be permanently trapped (Pye, 1995). In the dry season this moisture can be provided by the deliquesce effect explained above.

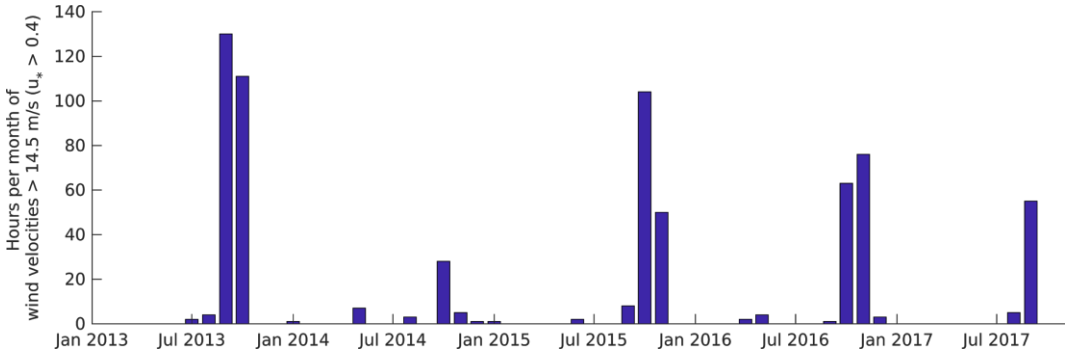

Figure 39. Monthly hours of high wind speed exposure that exceed the emission threshold of pan surface sediments (data from ERA 5 climate model).

Overall, our results on the mapping of spatio-temporal crust developments at the surface of the Omongwa pan, linked with data on surface wetness, temperature, and wind, allow to develop new insights on salt pan surface processes and on drivers of Omongwa flooding/desiccation cycles, such as:

1) After wet conditions at the surface of the pan due to major flooding or smaller rain events, first a mixed gypsum halite crust appears in less moist parts of the surfaces. Further in the dry season, a successive transition of mixed gypsum-halite to bright efflorescent halite crust is observed, where the aerial coverage of bright halite crust can reach up to 80% of the total pan surface after several months of dry conditions. Then a transition of bright halite to mixed calcite-quartz-sepiolite crust type is observed at the end of the dry season that can be depending on the years

more or less strong. This transition precedes the arrival of wet conditions that is depending on the magnitude and occurrence of rain events and can lead to increased or shortened periods of flooding coupled with the disappearance of surface crust.

2) After the wet season, the build-up of mixed halite gypsum crust is observed independent of the occurrence of big or small flooding events. Thus, the build-up of mixed halite gypsum crust at the beginning of the desiccation stage does not rely on an extensive flooding event to redistribute the salt minerals, but results from the combined effect of evaporation and capillary rise to develop these crusts from subsurface brines. Driven by lower temperature in the cold winter month an extensive efflorescent halite crust develops, due to higher relative humidity at night-time.

3) In the strong wind season, of the late summer to early autumn months (August to October) associated with the end of the dry season and the start of the new wet season, the areal coverage of crust types is changing from bright efflorescent halite crust to a more mixed calcite-quartz-sepiolite crust endmember. This change in crust development is more or less observed depending on the years. Nevertheless, the amount of change seems to be mainly driven by wind speed and exposure. This change is mostly attributed to the removal of efflorescent halite crust by wind erosion processes. In this time period, an increased dust emission could thus be expected.

6. Conclusions

This study has investigated the potential of multitemporal Landsat dense time-series to spectrally differentiate surface crust types of variable evaporite compositions and to subsequently map their multi- and inter-annual changes of the Omongwa salt pan in the Namibian Kalahari region. Furthermore, we assessed the climatic influences on the pan surface crust during repeated flooding and desiccation cycles.

A multiannual analysis of the spatio-temporal distribution of salt pan crust types was developed including an adapted methodology that uses Sequential Maximum Angle Convex Cone (SMACC) endmember selection and Spectral Angle Mapper (SAM) classification. A time-series of 77 cloud-free Landsat 8 OLI scenes was analysed covering several pan cycles during a time period of four and a half years (04/2013-10/2017). The spectral interpretation of the crust types derived from Landsat OLI was performed based on essential information provided by laboratory spectroscopy, as well as mineralogical XRD analysis of 49 field samples collected during three field campaigns (2014-2016) reflecting different seasons and surface conditions of the salt pan. Through the implementation of the endmember definition and mapping code in the Google Earth Engine this time-series can be extended with future Landsat acquisitions to support a regular monitoring of pan processes.

During the observation period, seasonal transitions in the surface crust were identified and related to the environmental process of the pan's flooding and desiccation cycles:

1) After a pan flooding event, a mixed halite-gypsum crust develops at the beginning of the drying process, which is driven by higher temperatures and capillary rise of subsurface brine.

2) This stage is followed by a successive transition to bright efflorescent halite crust during an extended period of dry conditions that is mainly driven by the large temperature drop during winter nights and a successive rise in relative humidity that exceeds the deliquescence point of halite.

3) At the end of the seasonal cycle, a transition of the bright halite crust to a mixed calcite-quartz-sepiolite crust is observed, which correlates to increasing aeolian activity that exceed the friction velocities thresholds of the surface and might indicate an increase in dust emissions from the salt pan.

Overall, this study shows that remote sensing analyses allow to accurately map and monitor spatio-temporal pan surface processes in a highly dynamic environment of a large Namibian salt pan. Further, new insights related to the seasonal and inter-annual evolution of salt pans surfaces could

be revealed. These new insights were linked to surface wetness, temperature and wind magnitude and could provide an assessment of climate controls on the spatial extent of salt crust formation. With the increasing availability of repeated global multispectral satellite data, the presented approach can be applied to study similar pan environments and increase our knowledge on their spatio-temporal development and the processes that drive their evolution. Furthermore, these analyses can help to assess the dust emissivity of these environments and bring progress to the impact assessment of climate changes and land surface responses of arid environments.

Acknowledgments: This work was funded by the German Federal Ministry of Education and Research (BMBF) as part of the joint project “GeoArchives—Signals of Climate and Landscape Change preserved in Southern African GeoArchives'' (No. 03G0838A) within the “SPACES Program—Science Partnerships for the Assessment of Complex Earth System Processes” research initiative. Project partners from GFZ, TUM and SaM are gratefully acknowledged for intensive joint field works and science discussions. Ansgar Wanke, Kombada Mhopjeni and the Namibian Geological Survey are gratefully acknowledged for sample handling and clearance, science discussions, and support of our research. We also wish to thank Robert Behling and Daniel Berger for help with the field work, and Anja Maria Schleicher for support with the XRD analysis, as well as Hartmut Liep and Marina Ospald for the sample preparation. Further thanks to Aleksandra Wolanin and the Google Earth Engine Developers Group for their advice on coding with the Google Earth Engine. The authors also thank the USGS and NASA for providing the Landsat data used in this study.

Chapter V - Synthesis and Outlook

The overall goal of this thesis is to give an assessment of the potential of optical remote sensing for the analysis of salt pan environments. In the previous chapters, this potential was investigated by a detailed analysis of the Omongwa salt pan regarding the characterisation of its depositional environment (chapter II), the estimation and quantification of a key crust component (chapter III), as well as the interpretation of its seasonal dynamic and climatic drivers (chapter IV). The integrated approach of combining hyperspectral as well as multi-temporal analysis provided numerous scientific outcomes that will be discussed in the following sections with respect to the overarching key questions defined in chapter I.

1. Discussion of main results

(1) What can optical remote sensing contribute to the characterisation of the salt pan depositional environment?

Mapping depositional environments of playas by remote sensing techniques has been done in the past mainly either using monotemporal hyperspectral or few multispectral scenes as outlined in chapter II. In this thesis, information from hyperspectral satellite data for the identification and mapping of major crust types was combined with 30 years of archived multispectral data to evaluate the temporal stability of the pan surface and linked to accurate morphological information provided by an airborne LIDAR survey. The results show that the main mineralogical constituents of the top layer of the Omongwa pan deposits namely: quartz, halite, gypsum, calcite and sepiolite could be identified using laboratory analyses and successfully translated into spectral classes of major crust types that could be mapped using Hyperion hyperspectral satellite imagery. This mineralogical mapping of the surface crust appears to be well correlated to the areas of surface change, as well as to the pan's morphology. Areas associated with high change magnitudes are located in the central part of the pan, which is dominated by halite mineralogy and lower topographical areas. The high change magnitudes of the central halite area are linked to the solubility of halite compared to the other evaporite minerals, its location in the lowest part of the pan, as well as to the strong radiometric contrast between bright efflorescent halite crust and muddy pan sediments in time of minor rainfall events. Gypsum crust is the second most abundant crust type of the Omongwa pan. Unlike the halite crust, the gypsum area mapped with Hyperion is associated with more stable or intermediately dynamic surface regions in the multitemporal analysis and slightly higher topography. Although the difference in pan height of 10–15 cm between halite dominated and gypsum mixed crust is rather small, it seems to be enough to affect the

surface mineralogy. Such topographic lows are known as the geochemical centre of the playa environment. Here, the evaporation is most intense as it is the final receptacle of runoff after rainfall that has acquired a heavy solute load by dissolution of preciously built crusts (Eugster & Hardie, 1978). For an interpretation of the depositional environment the hydrological and morphological context, as well as the sub-surface deposits have to be included in the analysis. From a hydrological and morphological point of view the Omongwa pan is part of an inland basin with ephemeral channel and groundwater inflow. The suspended and soluble material in those waters along with evaporation and condensation processes of the brine collectively have led to the formation of chemical and clastic sediments found in the pan depression. The evaporite minerals include calcite, gypsum and halite in addition to the clastic minerals, such as quartz, feldspar and to a minor degree muscovite, and clays (sepiolite and montmorillonite) introduced to the playa mainly through fluvial and aeolian processes. Horizontally the calcite abundance decreases from margin to the playa centre, followed by a gypsum rich facies and halite abundance that increases in direction to the pan centre. **Figure 40** presents the interpretation of the depositional environment based on the remote sensing results, following the general concept of Eugster & Hardie (1978)

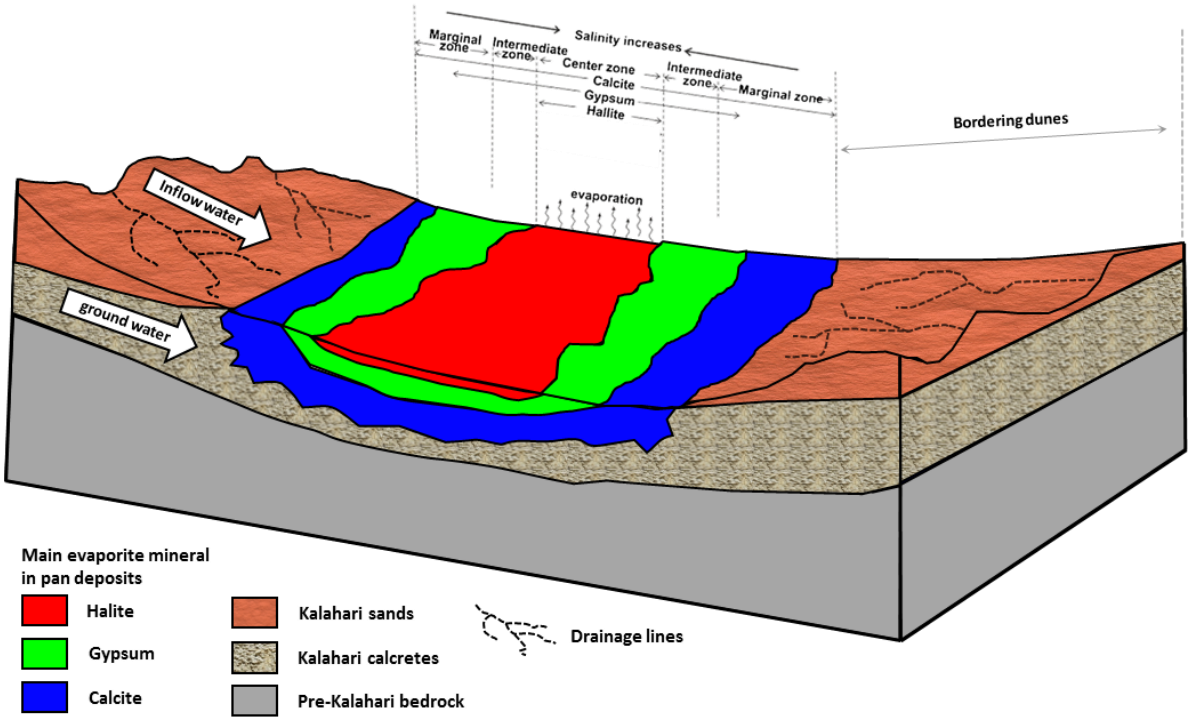

Figure 40. Model of the depositional environment / evaporative facies of the Omongwa Pan.

This observed distribution of depositional facies is consistent with the general zonation typical of other playas, which resembles a bull's eye pattern (Shaw & Bryant, 2011; Soltaninejad, Ranjbar, Honarmand, & Dargahi, 2018).

Considering not only the horizontal distribution mapped by remote sensing, but information about the sub-surface attributes of the pan deposits described in previous studies by Genderjahn et al. (2018) and Mees (1999) an attempt for the reconstruction of the evolutional pathway of the brine can be made. Data from 1-4 m deep sediment cores show that the fraction of calcite in the pan deposits is increasing with depth. In the top 50 cm 10-15% in the top 50 cm and 45-70% >2 m depth, opposed to gypsum and halite that are most abundant in the top layer and in general decrease with depth. The vertical distribution can be attributed to the calcrete bedrock, in which the pan has evolved, the groundwater inflow and subsequent brine saturation and formation of evaporite minerals. Although the sediments structure is much more complex on a fine scale regarding the distribution of evaporite material in the silicate matrix, e.g. along desiccation cracks and the occurrence of other hydromorphic features (Mees, 1999), the general distribution of the main mineralogical component is strongly linked to the hydrology and of the playa basin (Hardie, 1968; Rosen, 1994) and can therefore be used to infer on the brine evolution. The distribution of the depositional facies of the Omongwa pan (**Figure 40**) base on the remote sensing analysis suggests a typical evolution pathway of brine concentration and evaporite formation, in which the brine becomes progressively depleted in carbonate and sulphates from the margins to the centre of the pan. In the general model of geochemical behaviour of brine evolution described by Eugster & Hardie (1978) the chemistry of the brine undergoes a succession of geochemical divides. Successive water types depend on initial water chemistry and ratios of principal ions found in the brine (James I. Drever, 1997). According to combined information on the evaporite assemblage from the spatial mapping based on the remote sensing analysis and sub-surface core data is likely that the brine evolution of the Omongwa pan has followed the path of a $CaCO_3$ - Na-$CaSO_4$ - NaCl brine described in the model of Eugster & Hardie (1978). **Figure 41** shows the general brine evolution model of Eugster & Hardie (1978) and highlights the suggested brine evolution path for the Omongwa salt pan that results in the observed evaporite minerals assemblage. This path of brine evolution and crystallization path begins with the precipitation of calcite ($CaCO_3$) and other carbonates like dolomite ($CaMg(CO_3)_2$)or magnesite ($MgCO_3$), as well as the Mg-silicate sepiolite ($Mg_4Si_6O_{15}(OH)$) that mainly depend on a high Mg/Ca ratio of the brine. At the Omongwa pan calcite is the main carbonate mineral, which is explained by the already high calcite content of the calcrete bedrock of the pan. However, dolomite and sepiolite were also found in some surface samples up to

abundances of 30% in some locations. As carbonates precipitates and solutions becomes progressively more concentrated, either the CO_3^{2-} or the cations (Ca^{2+}, Na^{+}, Mg^{2+}) are depleted first. If the carbonate-ions in the brines are depleted first sulphates are the next precipitating phase due to their solubility (Deocampo & Jones, 2014).

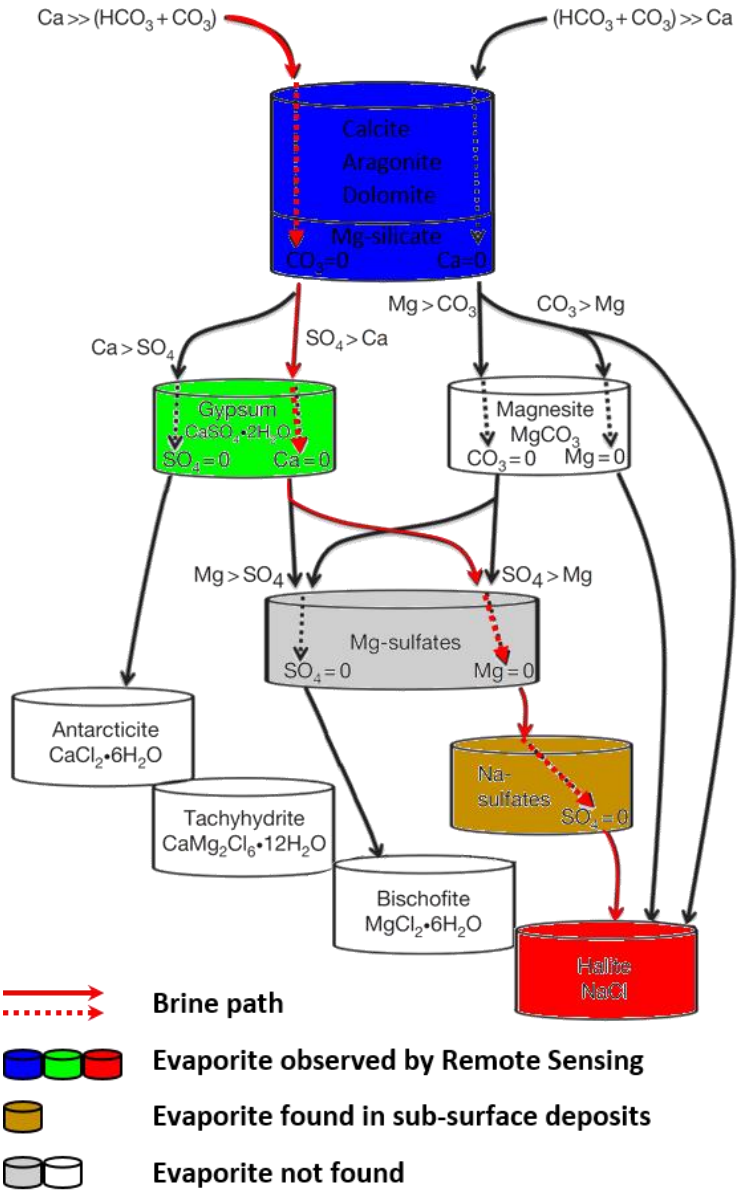

Figure 41. Brine evolution model after Eugster & Hardie (1978) for the geochemical evolution of non-marine waters and major evaporite minerals associated with the brine types (figure after Deocampo & Jones (2014) modified). The brine evolution path of the Omongwa pan is highlighted by red arrows and mineralogical assemblages found at the test site are coloured.

Such is the case for the Omongwa pan with extensive gypsum ($CaSO_4 \cdot 2H_2O$) abundance in the pan sub-surface deposits, as well as in the surface crust. A new natural Na-Ca-sulphate, the so called

Omongwaite ($Na_2Ca_4(SO_4)_6 \cdot 3H_2O$), was found for the first time at the test site by Florias Mees et al. (2008), as inclusion in gypsum crystals in the upper part of the pan deposits.The mineral represents an end-member of a series of possible compositions, in which Na substitutes Ca in basanite ($Ca_6(SO_4)_6 \cdot 3H_2O$), which happens under rapid brine concentration and saturated NaCl solutions (Mees et al., 2008). After carbonate and sulphate late precipitation products such as halite and bitter salts form by the further removal of water by evaporation from highly concentrated brines. At the Omongwa pan halite is found throughout pan sediments, as well as concentrated in efflorescent surface crust. The lack of trona in the deposits indicates very rapid brine concentration, as its formation is limited by the kinetics of CO_2 addition to the brine (Eugster & Hardie, 1978). This described crystallisation sequence would be observed as a temporal successive layers in a closed standing water system. However, at many playa environments it was observed that the crystallization steps take place at different spatial positions as a result of a concentration gradient from the pan margin, where dilute water enters the system to highly concentrated brine at its centre leading to the concentric zonation of evaporite minerals. This concentration gradient was established by continuous sub-surface flow of brine in toward the centre of the pan coupled with continuous evaporation (Hardie, 1968).

The applied approach of mapping depositional environments with the aid of remote sensing data and methods is transferable to a wide range of evaporite environments. However, the specific model of the depositional environment is built on information gained through remote sensing analyse, such as the spectral unmixing procedure. For this step most of the mineralogical components need to be identifiable by remote sensing. The use of hyperspectral data greatly increases the number of minerals that can be discriminated compared to multispectral analyses, but some minerals like halite or sylvite do not have diagnostic absorption features in the VNIR-SWIR spectral range and can only be indirectly assessed. Furthermore, overlapping spectral features may challenge an approach solely based on remote sensing data. It also has to be noted that field observations and in particular sedimentary analysis of the sub-surface layers provided by previous and concurrent studies (S. Genderjahn et al., 2018; Mees, 1999; Schuller, Belz, Wilkes, & Wehrmann, 2018) have been essential to confidentially differentiate the zones of the pan depositional environment, as well as the reconstruction of the brine evolution and hydrological setting. As optical remote sensing data can only provide information on the surface properties and status, a comprehensive understanding on the specific evaporite environment can only be achieved in the combination with the integration of these additional information.

(2) Can mineralogical crust components of salt pan environments be robustly mapped and quantified by current and upcoming hyperspectral sensors?

Only a very limited number of studies explore the potential to quantify mineralogical crust components in salt pans. However, the quantification and monitoring of the salt crust's mineralogy is highly relevant e.g. to elucidate the contribution and yet uncertain role of mineral dust emissions in the radiative forcing of the atmosphere (Ramaswamy et al., 2001). The discrimination and quantification of playa surface minerals is dependent on their spectral properties. While most of the salt minerals that constitute various playa environments do not have diagnostic absorption features in the optical spectral region, it has been shown that the abundance of gypsum can be estimated in soil mixtures via reflectance spectroscopy in the laboratory (Khayamim et al., 2015; Weindorf et al., 2016). As shown in chapter II crust types of salt pan environments associated with many other minerals like halite, sepiolite, calcite and sepiolite can be differentiated and mapped by hyperspectral remote sensing. However, these represent mixtures consisting of multiple mineralogical and sedimentological attributes that have been spectrally characterised through the selection of endmembers that are specific to these mixtures and less transferable to other settings. The direct quantification through the parametrisation of spectral absorption features allows for a more general and less site specific estimation of a mineral from the pan surface crust. Therefore the potential for gypsum estimation of current and upcoming hyperspectral sensors has been evaluated by testing robust approaches for the parametrisation of its characteristic spectral properties. Prediction functions for the gypsum component have been determined in the laboratory and subsequently transferred to the remote sensing scale. Overall, the model results at the laboratory scale were well within range of results obtained by previous studies, e.g. Khayamim et al. (2015) that used PLSR on the total spectral range. The Continuum Removed Absorption Depth (CRAD) parametrisation shows that most relevant information for gypsum estimation is included in the 1.75 region and that the method works very well in a mixture of common evaporite and silicate minerals often found in salt pan settings. Validation of the results with ground-truth data shows that the simple normalized differenced based NDGI parametrisation provides the most robust results for hyperspectral remote sensing application, as it minimizes the influence of the neighbouring atmospheric absorption, while still being sensitive to gypsum variability. The presented approach does not need the SWIR II spectral region for gypsum estimation, but exploits a feature located in the SWIR I. The solar spectral irradiance of this region more than doubles the irradiance in the SWIR II (Eismann, 2012). Therefore more photons reach the detectors of hyperspectral sensors, which leads to increased signal-to-noise levels (Guanter et al., 2015), as well

as more reliable quantitative analysis of surface properties (E. Ben-Dor, 2002). Furthermore, the developed approach is expected to also perform reasonably well for soil mixtures in an agricultural setting, as it does not rely on the ~2.2 µm gypsum feature that can be confused with the overlapping absorption features such as clay minerals, which was often included in previous studies (Gleeson et al., 2010; Shrestha et al., 2005) and mapping frameworks (Kokaly et al., 2011).

(3) What processes can be characterised by multitemporal remote sensing regarding seasonal pan changes and their link to the climatic drivers?

Salt pans have been described as one of the most dynamic environments with high variation in surface features on daily, weekly, monthly, and annual basis (Bowen et al., 2017; Robert G. Bryant & Rainey, 2002). Currently, the characterisation and monitoring of playa environments is problematic, due to the lack of records about their surface conditions, including times of inundation and the formation of different evaporite during the pan's desiccation. Remotely sensed data can surrogate ground observations, if spectral or other features of the satellite image allow reliable interpretation. In this frame chapter IV describes a detailed assessment of the seasonal variation using dense time series of 70 multispectral images that cover a period of 4 years. This increase in data availability allowed to observe the pan dynamic on a sub-monthly scale, whereas previous studies on salt pan dynamic only provided monthly to seasonal information (Bowen et al., 2017) or even yearly temporal resolution for periods before the year 2000 (Carmen Castañeda et al., 2005). However, compared to the analysis of pan surface crust composition based on the hyperspectral data shown in chapter II, the reduced spectral resolution of multispectral data does not allow to discriminate distinct minerals and made it necessary to simplify and merge spectral classes. Specifically, the distinction between the crust type dominated by sepiolite and calcite had to be merged with surfaces that are mainly composed of quartz and feldspar, as their mixture could not be differentiated by the spectral analysis based on multispectral data. Yet, the much denser temporal resolution allows a more detailed process observation of salt pan environments, such as the solution and build-up of evaporite surface crusts, and provides the potential to link these surface changes to its climatic drivers. One of the most important processes that determines the pan dynamic involves the wetting and drying cycles and the precipitation–dissolution of surface crusts (J. I. Drever, 2005). A model of these processes of modern pan systems called the saline pan cycle has been developed by Lowenstein & Hardie (1985). It describes that the episodic formation and dissolution of surface crust evaporites follows a cycles of flooding, evaporation, and desiccation of the playa surface (Chivas, 2007; Lowenstein & Hardie, 1985). In chapter IV, we showed that over

four seasons of reoccurring key stages of the saline pan cycle could be observed and identified through major changes in the surface reflectance properties (**Figure 42**):

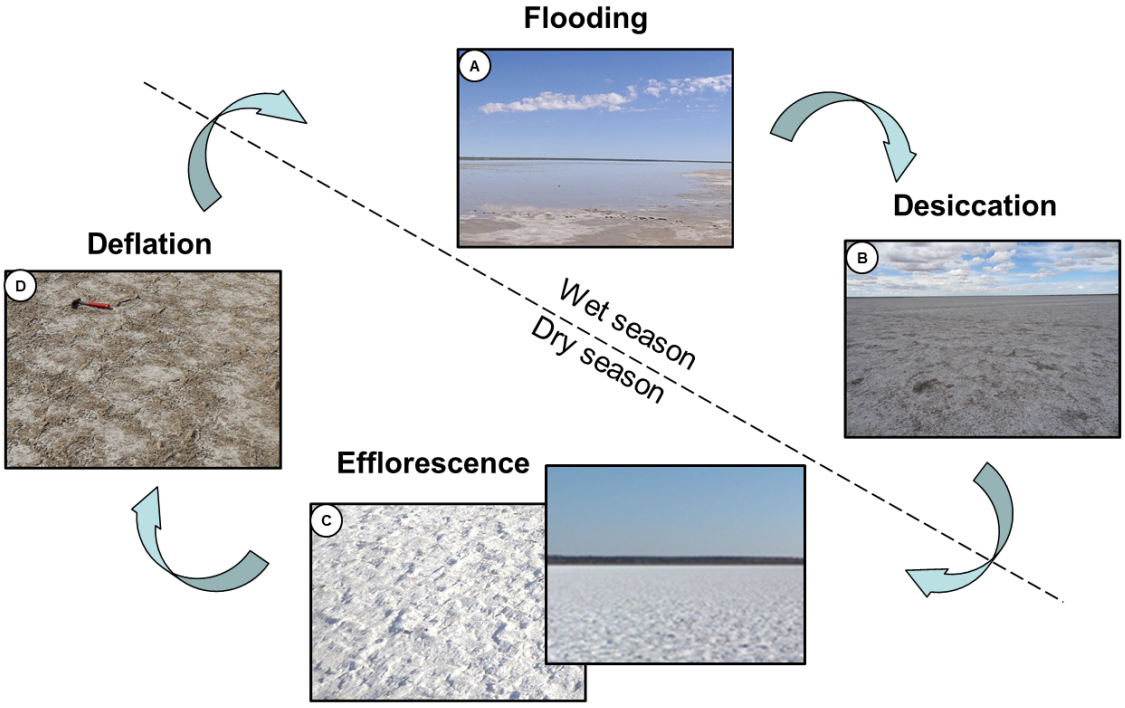

Figure 42. Field characterisation of the seasonal pan stages for the Omongwa pan, following the modified model of the saline pan cycle of Lowenstein & Hardie (1985).

1 - Flooding stage (**Figure 42A**): A shallow and brackish lake or smaller pools may form after flooding of the dry pan with meteoric water either directly precipitated on the pan surface, by runoff from the bordering dunes, or by groundwater flow through the Kalahari sands or calcrete layers. The dilute waters dissolve the evaporite (mostly halite rich) surface crust, as it ponds in the topographically low areas of the pan. Dissolution of crust depends on the degree of undersaturation of the inflow water, minor influxes are enough for the dissolution of halite, but the solubility of gypsum is at least 30 times lower (Klimchouk, 1996), which makes the sulphate mineral more resistant to small precipitation events. The higher stability of the gypsum rich pan regions has also been observed in the analysis of long-term (1984-2015) surface change magnitude (chapter 2). This fractional dissolution of surface crust returns preferably the most soluble constituents to solution, leaving behind the less soluble evaporites such as sulphates, carbonates and silicate minerals (J. I. Drever, 2005). In the four seasons of remote sensing data at the Omongwa pan, flooding events with up to 60-80% of the surface area flooded have been observed during the wet season in 3 out of the 4 years and one very dry year with ponding below 3% of the pan surface. During the major inundation events at the Omongwa pan only the gypsum and calcite rich crust types remain at the

pan margin surrounding a shallow water body. The monitoring of frequency and magnitude of inundation events is of great relevance, because it drives the pan cycle and has been recognised as the most important parameter for the evolution of the pan deposits and its mass budget over longer periods (Shaw & Bryant, 2011; Yechieli & Wood, 2002).

2 - Desiccation stage (**Figure 42B**): Driven by higher temperatures and capillary rise of the sub-surface brine an initial surface crust is formed under dry conditions. Complete evaporation of the ephemeral lake can occur within days in small, shallow lakes or can take years in large, deeper lakes (Smoot & Lowenstein, 1991). With the exception of the relative dry year of 2014, the flooding of each season between 2015 and 2017 3-4 month are needed for complete evaporation of the water pools and re-building of surface crust. At the test site the initial crust mainly contains a mixture of gypsum and halite that spatially grows form the pan margin into the more moist pan centre.

3 - Efflorescence stage (**Figure 42C**): After the complete desiccation of the ephemeral water body, and prolonged dryness in the winter season the initial surface layer gets heavily enriched in halite. This change to very bright surface is very notable already in the visible reflectance of the pan surface (**Figure 42C**). Salt efflorescence is very common process among different evaporite environment, where primarily halite overgrowths the initial surface layer. Most commonly this observation is attributed to the continuous evaporative pumping of sub-surface brines under very high temperatures, e.g. for Lake Magadi, Kenya or Saline Valley, USA (Smoot & Lowenstein, 1991). However, at the Omongwa pan test site the transition to bright efflorescent halite crust appears in the winter month with moderate to cold temperatures. Driven by the large temperature drop during winter nights and a successive rise in relative humidity the very hygroscopic halite binds water vapour form the air and forms a saturated solution, when the so called deliquescence point of halite is exceeded (Greenspan, 1977). The repeated halite re-solution from the surface and re-precipitation during the day leads to the build-up of pure halite crust at the surface crust. A similar process is described for halite efflorescence in saltpans of the hyperarid Atacama Desert (Artieda et al., 2015; Davila et al., 2008; Wierzchos et al., 2012).

4 - Deflation or degradation stage (**Figure 42D**): At the end of the seasonal cycle, a transition of the bright halite crust to a much darker mixed crust composed of mainly quartz and or calcite is observed. The strength of this transition in the late winter month (August to October) correlates to the magnitude in aeolian activity at the test site and might be attributed to the removal of efflorescent halite crust by wind erosion. In this time period, increased dust emissions are also observed from the dunelands of the southern Kalahari (Abinash Bhattachan, D'Odorico, Okin, & Dintwe, 2013). Therefore, it is also possible that the surface changes are caused by a mixed effect

from (1) the removal of efflorescent halite crust by wind erosion and (2) the accumulation of windblown material originating from the pan surroundings.

2. Directions of future research

In the frame of this thesis, the potential of current and upcoming optical remote sensing for the analysis of evaporite environments have been evaluated. The results showed that the recent advances in technology and data availability have driven the development of methods that make use of this increase in data amount and of analytical potential, especially for the characterisation of mineralogical composition, as well as for the temporal dynamic and surface processes. It can be expected that future research will again be driven by new developments and the combination of existing technologies in synergetic use with optical remote sensing. For example, the availability of multispectral data greatly increased after the launch of Landsat 8 in 2013 with a revisiting time of 16 days to just under two acquisitions per month with a swath of 185 km (D. P. Roy et al., 2014). More recently the European Space Agency (ESA) launched the two satellites of the Sentinel 2 constellation that since 2017 provide optical images in 13 spectral bands with a 5-day revisit period combined with an unprecedented ground resolution of 10 to 20 m for most bands with a large swath covering 290 km (Drusch et al., 2012). The combination of Landsat 8 and Sentinel 2 potentially can provide up to 8 acquisitions per month and therefore significantly will also increase the potential for monitoring of salt pan processes.

Looking towards the future, this trend of increased data availability will continue with a wide range of new hyperspectral satellite systems in the VNIR-SWIR spectral range that will be launched in the next years. Advances in sensor technology are expected to improve spectral sampling and the radiometric performance of these upcoming imaging spectroscopy systems, which will yield higher signal-to-noise ratios at a higher spatial resolution (Rast & Painter, 2019). The PRISMA (PRecursore IperSpettrale della Missione Applicativa) satellite mission just launched and is currently in its final testing phase before operational acquisition (Lopinto, Daraio, Guarini, & Loizzo, 2019). PRISMA will be a pre-operational system and a technology demonstrator, which will focus with its acquisition on the Euro-Mediterranean Regions (Rast & Painter, 2019). The system covers the VNIR-SWIR spectral range with 237 spectral bands at a variable spectral bandwidth between 6 and 12 nm, and a 30 m spatial resolution over a 30 km swath (Pignatti et al., 2015). Subsequently, towards the end of 2020 to early 2021, the German Environmental Mapping and Analysis Program (EnMAP) is expected to be launched (Pinnel, 2019). The system provides similar hyperspectral capabilities as PRISMA. Although primarily science-driven, the EnMAP mission will also address applications beyond scientific issues (Guanter et al., 2015). PRISMA and EnMAP will co-exist with other comparable and complementary missions, such the Italian-Israeli Spaceborne Hyperspectral Applicative Land and Ocean Mission SHALOM, which is planned for launch in 2022 with increased

spatial resolution of 10 m (Rast & Painter, 2019). The mission will focus on commercial use and on application for ecosystems primarily of the coastal zone (Feingersh & Ben-Dor, 2015). Another important mission with a focus on the observation of arid environments is the Earth surface Mineral dust source InvesTigation (EMIT) scheduled for 2021. EMIT is a VNIR-SWIR imaging spectrometer to be mounted on the international space station (ISS) with the main objective to determine the mineral composition of natural sources that produce dust aerosols around the world (R. Green, 2018). The low orbit of the ISS leads to about 16 orbits per day with an approximate repeat cycle of every 3 days. The specific revisiting time depends on the latitude of the target with potential of diurnal coverage (Cynthia, Evans, & Robinson, 2019). With its explicit mission objective to study sources of dust emission, it can be expected to prioritize image acquisition of playa environments. Currently under discussion are also the next generation of hyperspectral satellite missions for the mid-2020s like ESA'S new Sentinel candidate the Copernicus Hyperspectral Imaging Mission (CHIME) (Nieke & Rast, 2018), as well as NASA's Biology and Geology (SBG) satellite that will be designed to operationally acquire hyperspectral imagery over larger areas (e.g. SBG with a swath of 160 km) and much more frequently than the previous listed tasking missions (Pinnel, 2019). The technical developments of these sensors and platforms will provide new opportunities for improved characterisation and monitoring of complex salt pan environments and their dynamics in the context of climate change and anthropogenic impact.

Future research also has great potential in the synergistic use of non-optical remote sensing, such as the thermal Infrared (TIR) or Synthetic Aperture Radar (SAR). The thermal infrared electromagnetic spectrum opens the analytical potential of remote sensing for a wide range of silicate minerals that are common in playa settings that cannot be accurately discriminated by optical remote sensing (Ramsey, Christensen, Lancaster, & Howard, 1999). Furthermore, the many evaporite minerals have additional features in the thermal infrared (J.K. Crowley, 1993) that can increase the detection in difficult mineralogical mixtures, when VNIR-SIWR and TIR information are combined. Until now, a very limited number of studies explored the thermal infrared region for the analysis of evaporite environment (e.g. James K. Crowley & Hook, 1996; Katra & Lancaster, 2008), and none explored the synergetic potential of both the solar reflective and the thermal emissive spectral domain in this context. Since mid-2018 the 6-band multispectral thermal ECOSTRESS (ECOsystem Spaceborne Thermal Radiometer Experiment on Space Station) camera has been installed on the ISS. It provides data with 38-m in-track by 69-m cross-track spatial resolution with potential diurnal coverage and a swath greater than 300 km (Hook, 2019), which makes it very interesting for large scale process monitoring of evaporite environments and should be tested.

The combined use of optical remote sensing and Synthetic Aperture Radar (SAR) technology also has great potential. Several studies showed that SAR is highly sensitive to temporal variations in properties like surface roughness (Archer & Wadge, 2001; Liu et al., 2016) and soil moisture of salt pans (Tansey & Millington, 2001). Such information on roughness and brine moisture changes can help e.g. for a better understanding of processes like halite efflorescence (Wadge & Archer, 2003), especially in combination with the spectral information from optical remote sensing. For the monitoring of larger test sites of at least 25 km², the passive SAR based Global Precipitation Measurement (GPM) mission launched in 2014 can provide precipitation estimates at high temporal (0.5–3.0 h), which is especially useful for less populated remote regions, where systematic surface measurements of precipitation are missing (Skofronick-Jackson et al., 2016).

Regarding the methodological development, it is likely that the trend of big data analysis in conjunction with machine learning (L. Ma et al., 2019) will further grow and that parallelisation and cloud computing will facilitate the processing of the ever-growing volume in data (Cavallaro, Erlingsson, & Memon, 2018). Cloud infrastructures can provide the required flexibility to manage huge amounts of data and to efficiently process them, thus making possible to apply analysis on a global scale. One cloud-based platform that becomes increasingly popular is the Google Earth Engine (GEE) that makes the petabytes of free multi-temporal remote sensing data available on its webservice (Mutanga & Kumar, 2019). GEEs concept of integrated data visualization, processing and analysing may open the field of remote sensing to a wider community of non-remote sensing experts. Although this new potential of global analysis holds great promises, careful testing is necessary before research approaches of a specific evaporite environments can be transferred to other settings.

3. Conclusion

This thesis provides new insights into the capabilities of optical remote sensing for the characterisation of salt pan environments by combining information from hyperspectral data with the increased temporal coverage of multispectral observations for a more complete understanding of spatial and temporal complexity of salt pan environments. This research has been able to show that optical remote sensing can be used to map the mineralogy of salt pan surfaces both quantitatively and semi quantitatively. It further highlights the importance of robust and adapted methods that can deal with imperfect remote sensing data that often is affected by atmospheric and radiometric noise or has been collected under none-ideal acquisition conditions. The combination of mineralogical mapping with long-term change analysis and morphological information enabled the developed of a spatial model of the test site's depositional environment. The further integration of information about the sub-surface deposits with the remote sensing results allowed to reconstruct the path of brine evolution of this evaporite environment and improve the knowledge of the local hydrological and sedimentological processes. The dense seasonal and inter-annual remote sensing observation provided the basis to understand the specific seasonal cycle of inundation and desiccation stages of the playa environment, including the climate driving forces and their impact on surface changes. Besides the academic motivation of this research, the understanding of playa environments is a prerequisite for sound and sustainable management decisions in these regions. Although the spectral unmixing and mapping models, as well as the multitemporal characterisation performed in the frame of this thesis cannot directly be transferred to other sites of interest, the general approach and the developed framework could be well transferred and applied for the study of arid landscapes and salt pans of others regions of the world that become increasingly threatened by changing climate and anthropogenic impact.

Many more advances in senor technology and data availability are expected throughout the next decade that will further improve the capabilities of optical remote sensing and will call for additional refinement of methods, data storage and computational solutions. E.g. the transition to big data analysis and cloud computing will be a major step for the scientific and applied remote sensing community, especially for time-series data. Furthermore, the combination with information from other remote sensing data, e.g. from the long-wave infrared spectral region, as well as SAR holds great potential that still need to be assessed in the context of salt pan environments.

References

Abbas, K., Deroin, J.-P., & Bouaziz, S. (2018). Monitoring of playa evaporites as seen with optical remote sensing sensors: Case of Chott El Jerid, Tunisia, from 2003 to present. *Arabian Journal of Geosciences*, *11*(5), 92. https://doi.org/10.1007/s12517-018-3410-0

Adams, J. B., Smith, M. O., & Johnson, P. E. (1986). Spectral mixture modeling: A new analysis of rock and soil types at the Viking Lander 1 Site. *Journal of Geophysical Research: Solid Earth*, *91*(B8), 8098–8112. https://doi.org/10.1029/JB091iB08p08098

Aghamohamadnia, M., & Abedini, A. (2014). A morphology-stitching method to improve Landsat SLC-off images with stripes. *Geodesy and Geodynamics*, *5*(1), 27–33. https://doi.org/10.3724/SP.J.1246.2014.01027

Alanazi, H. A., & Ghrefat, H. A. (2013). Spectral Analysis of Multispectral Landsat 7 ETM + and ASTER Data for Mapping Land Cover at Qurayah Sabkha, Northern Saudi Arabia. *Journal of the Indian Society of Remote Sensing*, *41*(4), 833–844. https://doi.org/10.1007/s12524-013-0291-2

Alexandridis, T. K., Cherif, I., Kalogeropoulos, C., Monachou, S., Eskridge, K., & Silleos, N. (2013). Rapid error assessment for quantitative estimations from Landsat 7 gap-filled images. *Remote Sensing Letters*, *4*(9), 920–928. https://doi.org/10.1080/2150704X.2013.815380

Alphen, J. G. van, & Romero, F. de los R. (1971). *Gypsiferous Soils: Notes on Their Characteristics and Management*. International Institute for Land Reclamation and Improvement.

Archer, D. J., & Wadge, G. (2001). Modeling the backscatter response due to salt crust development. *IEEE Transactions on Geoscience and Remote Sensing*, *39*(10), 2307–2310. https://doi.org/10.1109/36.957294

Artieda, O., Davila, A., Wierzchos, J., Buhler, P., Rodríguez-Ochoa, R., Pueyo, J., & Ascaso, C. (2015). Surface evolution of salt-encrusted playas under extreme and continued dryness: Surface Evolution of Salt-Encrusted Playas. *Earth Surface Processes and Landforms*, *40*(14), 1939–1950. https://doi.org/10.1002/esp.3771

ASD Inc. (2015). Field Spec—User manual. Retrieved 1 December 2015, from http://support.asdi.com/Document/Viewer.aspx?id=162

Aspinall, R. J., Marcus, W. A., & Boardman, J. W. (2002). Considerations in collecting, processing, and analysing high spatial resolution hyperspectral data for environmental investigations. *Journal of Geographical Systems*, *4*(1), 15–29. https://doi.org/10.1007/s101090100071

Atlas of Namibia Project. (2002). Atlas of Namibia Project (2002) Directorate of Environmental Affairs, Minitry of Environment and Tourism. Retrieved 24 November 2015, from http://www.uni-koeln.de/sfb389/e/e1/download/atlas_namibia/e1_download_climate_e.htm

Baddock, M. C., Bullard, J. E., & Bryant, R. G. (2009). Dust source identification using MODIS: A comparison of techniques applied to the Lake Eyre Basin, Australia. *Remote Sensing of Environment*, *113*(7), 1511–1528. https://doi.org/10.1016/j.rse.2009.03.002

Baddock, M. C., Zobeck, T. M., Van Pelt, R. S., & Fredrickson, E. L. (2011). Dust emissions from undisturbed and disturbed, crusted playa surfaces: Cattle trampling effects. *Aeolian Research*, *3*(1), 31–41. https://doi.org/10.1016/j.aeolia.2011.03.007

Bartholomeus, H. M., Schaepman, M. E., Kooistra, L., Stevens, A., Hoogmoed, W. B., & Spaargaren, O. S. P. (2008). Spectral reflectance based indices for soil organic carbon quantification. *Geoderma*, *145*(1), 28–36. https://doi.org/10.1016/j.geoderma.2008.01.010

Bayer, A., Bachmann, M., Kaufmann, H., & Mueller, A. (2012). A Comparison of Feature-Based MLR and PLS Regression Techniques for the Prediction of Three Soil Constituents in a Degraded South African Ecosystem. *Applied and Environmental Soil Science*, *2012*, e971252. https://doi.org/10.1155/2012/971252

Bayer, A., Bachmann, M., Rogge, D., Müller, A., & Kaufmann, H. (2016). Combining Field and Imaging Spectroscopy to Map Soil Organic Carbon in a Semiarid Environment. *IEEE Journal of Selected Topics in Applied Earth Observations and Remote Sensing*, *9*(9), 3997–4010. https://doi.org/10.1109/JSTARS.2016.2585674

Bédard, F., Reichert, G., Dobbins, R., & Trépanier, I. (2008). Evaluation of segment-based gap-filled Landsat ETM+ SLC-off satellite data for land cover classification in southern Saskatchewan, Canada. *International Journal of Remote Sensing*, *29*(7), 2041–2054. https://doi.org/10.1080/01431160701281064

Ben-Dor, E. (2002). Quantitative remote sensing of soil properties. In *Advances in Agronomy* (Vol. 75, pp. 173–243). https://doi.org/10.1016/S0065-2113(02)75005-0

Ben-Dor, E., Chabrillat, S., Demattê, J. A. M., Taylor, G. R., Hill, J., Whiting, M. L., & Sommer, S. (2009). Using Imaging Spectroscopy to study soil properties. *Remote Sensing of Environment*, *113, Supplement 1*, S38–S55. https://doi.org/10.1016/j.rse.2008.09.019

Ben-Dor, E., Levin, N., Singer, A., Karnieli, A., Braun, O., & Kidron, G. J. (2006). Quantitative mapping of the soil rubification process on sand dunes using an airborne hyperspectral sensor. *Geoderma*, *131*(1–2), 1–21. https://doi.org/10.1016/j.geoderma.2005.02.011

Ben-Dor, Eyal, Irons, J. R., & Epema, G. F. (1999). Soil Reflectance. In A. N. Rencz & R. A. Ryerson (Eds.), *Manual of Remote Sensing, Remote Sensing for the Earth Sciences* (pp. 111–188). John Wiley & Sons.

Bergström, R., & Skarpe, C. (1999). The abundance of large wild herbivores in a semi-arid savanna in relation to seasons, pans and livestock. *African Journal of Ecology*, *37*(1), 12–26. https://doi.org/10.1046/j.1365-2028.1999.00165.x

Bharti, R., Kalimuthu, R., & Ramakrishnan, D. (2015). Spectral pathways for exploration of secondary uranium: An investigation in the desertic tracts of Rajasthan and Gujarat, India. *Advances in Space Research*, *56*(8), 1613–1626. https://doi.org/10.1016/j.asr.2015.07.015

Bhattachan, A., D'Odorico, P., & Okin, G. S. (2015). Biogeochemistry of dust sources in Southern Africa. *Journal of Arid Environments*, *117*, 18–27. https://doi.org/10.1016/j.jaridenv.2015.02.013

Bhattachan, Abinash, D'Odorico, P., Okin, G. S., & Dintwe, K. (2013). Potential dust emissions from the southern Kalahari's dunelands. *Journal of Geophysical Research: Earth Surface*, *118*(1), 307–314. https://doi.org/10.1002/jgrf.20043

Bioucas-Dias, J. M., Plaza, A., Camps-Valls, G., Scheunders, P., Nasrabadi, N., & Chanussot, J. (2013). Hyperspectral Remote Sensing Data Analysis and Future Challenges. *IEEE Geoscience and Remote Sensing Magazine*, *1*(2), 6–36. https://doi.org/10.1109/MGRS.2013.2244672

Boardman, Joseph W. (1993, October 25). *Automating spectral unmixing of AVIRIS data using convex geometry concepts*. Retrieved from http://ntrs.nasa.gov/search.jsp?R=19950017428

Boardman, Joseph W., Kruse, F. A., & Green, R. O. (1995). *Mapping target signatures via partial unmixing of AVIRIS data*. Retrieved from http://ntrs.nasa.gov/search.jsp?R=19950027316

Boardman, J.W., & Kruse, F. A. (1994). Automated spectral analysis: A geological example using AVIRIS data, northern Grapevine Mountains, Nevada. *Proceedings of the 10th Thematic Conference on Geologic Remote Sensing*, 1407–1418. Ann Arbor, Michigan.

Bowen, B. B., Bernau, J., Kipnis, E. L., Lerback, J., Wetterlin, L., & Kleba, B. (2018). The Making of a Perfect Racetrack at the Bonneville Salt Flats. *The Sedimentary Record*, *16*(2), 4–11. https://doi.org/10.2110/sedred.2018.2.4

Bowen, B. B., Kipnis, E. L., & Raming, L. W. (2017). Temporal dynamics of flooding, evaporation, and desiccation cycles and observations of salt crust area change at the Bonneville Salt Flats, Utah. *Geomorphology*, *299*(Supplement C), 1–11. https://doi.org/10.1016/j.geomorph.2017.09.036

Brell, M., Rogass, C., Segl, K., Bookhagen, B., & Guanter, L. (2016). Improving Sensor Fusion: A Parametric Method for the Geometric Coalignment of Airborne Hyperspectral and Lidar Data. *IEEE Transactions on Geoscience and Remote Sensing*, *54*(6), 3460–3474. https://doi.org/10.1109/TGRS.2016.2518930

Brown, D. J., Bricklemyer, R. S., & Miller, P. R. (2005). Validation requirements for diffuse reflectance soil characterization models with a case study of VNIR soil C prediction in Montana. *Geoderma*, *129*(3), 251–267. https://doi.org/10.1016/j.geoderma.2005.01.001

Bryant, Robert G. (1996). Validated linear mixture modelling of Landsat TM data for mapping evaporite minerals on a playa surface: Methods and applications. *International Journal of Remote Sensing*, *17*(2), 315–330. https://doi.org/10.1080/01431169608949008

Bryant, Robert G. (1999). Application of AVHRR to monitoring a climatically sensitive playa. case study: Chott El Djerid, Southern Tunisia. *Earth Surface Processes and Landforms*, *24*(4), 283–302. https://doi.org/10.1002/(SICI)1096-9837(199904)24:4<283::AID-ESP950>3.0.CO;2-9

Bryant, Robert G. (2003). Monitoring hydrological controls on dust emissions: Preliminary observations from Etosha Pan, Namibia. *The Geographical Journal*, *169*(2), 131–141. https://doi.org/10.1111/1475-4959.04977

Bryant, Robert G., Bigg, G. R., Mahowald, N. M., Eckardt, F. D., & Ross, S. G. (2007). Dust emission response to climate in southern Africa. *Journal of Geophysical Research: Atmospheres*, *112*(D9), D09207. https://doi.org/10.1029/2005JD007025

Bryant, Robert G., & Rainey, M. P. (2002). Investigation of flood inundation on playas within the Zone of Chotts, using a time-series of AVHRR. *Remote Sensing of Environment*, *82*(2–3), 360–375. https://doi.org/10.1016/S0034-4257(02)00053-6

Bryant, Robert Gavin. (1993). *The sedimentology and geochemistry of non-marine evaporites on the Chott el Djerid, using both ground and remotely sensed data* (University of Reading). Retrieved from http://www.robert-bryant.staff.shef.ac.uk/Bryant_thesis_OCR.PDF

Buck, B. J., King, J., & Etyemezian, V. (2011). Effects of Salt Mineralogy on Dust Emissions, Salton Sea, California. *Soil Science Society of America Journal*, *75*(5), 1971–1985. https://doi.org/10.2136/sssaj2011.0049

Bultman, M. W., Fisher, F. S., & Pappagianis, D. (2013). The ecology of soil-borne human pathogens. In *Essentials of Medical Geology* (pp. 477–504). Springer.

Burden, R. L., & Faires, J. D. (2011). *Numerical analysis* (9th ed). Boston, MA: Brooks/Cole, Cengage Learning.

Canty, M. J. (2014). *Image Analysis, Classification and Change Detection in Remote Sensing: With Algorithms for ENVI/IDL and Python, Third Edition* (3 edition). CRC Press.

Canty, M. J., & Nielsen, A. A. (2012). Linear and kernel methods for multivariate change detection. *Computers & Geosciences*, *38*(1), 107–114. https://doi.org/10.1016/j.cageo.2011.05.012

Carpenter, G. A., Wallace, G. J., & Hamre, S. (2002). *Great Salt Lake: An overview of change. The U.S. Bureau of Land Management's role in resource management of the Bonneville Salt Flats* (p. 10). Salt Lake City, Utah, United States.

Castañeda, C., Mendez, S., Herrero, J., & Betran, J. (2010). Investigating Soils for Agri-Environmental Protection in an Arid Region of Spain. In P. Zdruli, M. Pagliai, S. Kapur, & A. F. Cano (Eds.), *Land degradation and desertification: Assessment, mitigation and remediation*. Berlin: Springer-Verlag Berlin.

Castañeda, Carmen, Herrero, J., & Casterad, M. A. (2005). Facies identification within the playa-lakes of the Monegros desert, Spain, from field and satellite data. *CATENA*, *63*(1), 39–63. https://doi.org/10.1016/j.catena.2005.05.011

Cavallaro, G., Erlingsson, E., & Memon, A. (2018). *High Performance and Cloud Computing for Remote Sensing Data*.

Chabrillat, S., Eisele, A., Guillaso, S., Rogass, C., Ben-Dor, E., & Kaufmann, H. (2011). HYSOMA: An easy-to-use software interface for soil mapping applications of hyperspectral imagery. *7th EARSeL SIG Imaging Spectroscopy Workshop, Edinburgh, Scotland*.

Chabrillat, S., Goetz, A. F. H., Krosley, L., & Olsen, H. W. (2002). Use of hyperspectral images in the identification and mapping of expansive clay soils and the role of spatial resolution. *Remote Sensing of Environment*, *82*(2–3), 431–445. https://doi.org/10.1016/S0034-4257(02)00060-3

Chabrillat, S., Guillaso, S., Rabe, A., Foerster, S., & Guanter, L. (2016). From HYSOMA to ENSOMAP-A new open source tool for quantitative soil properties mapping based on hyperspectral imagery from airborne to spaceborne applications. *EGU General Assembly Conference Abstracts*, *18*, 14697. Retrieved from http://adsabs.harvard.edu/abs/2016EGUGA..1814697C

Chabrillat, S., Pinet, P. C., Ceuleneer, G., Johnson, P. E., & Mustard, J. F. (2000). Ronda peridotite massif: Methodology for its geological mapping and lithological discrimination from airborne hyperspectral data. *International Journal of Remote Sensing*, *21*(12), 2363–2388. https://doi.org/10.1080/01431160050030510

Chander, G., Markham, B. L., & Helder, D. L. (2009). Summary of current radiometric calibration coefficients for Landsat MSS, TM, ETM+, and EO-1 ALI sensors. *Remote Sensing of Environment*, *113*(5), 893–903. https://doi.org/10.1016/j.rse.2009.01.007

Chapman, J. E., Rothery, D. A., Francis, P. W., & Pontual, A. (1989). Remote sensing of evaporite mineral zonation in salt flats (salars). *International Journal of Remote Sensing*, *10*(1), 245–255. https://doi.org/10.1080/01431168908903860

Chappell, A., Strong, C., McTainsh, G., & Leys, J. (2007). Detecting induced in situ erodibility of a dust-producing playa in Australia using a bi-directional soil spectral reflectance model. *Remote Sensing of Environment*, *106*(4), 508–524. https://doi.org/10.1016/j.rse.2006.09.009

Chen, J., Zhu, X., Vogelmann, J. E., Gao, F., & Jin, S. (2011). A simple and effective method for filling gaps in Landsat ETM+ SLC-off images. *Remote Sensing of Environment*, *115*(4), 1053–1064. https://doi.org/10.1016/j.rse.2010.12.010

Chivas, A. R. (2007). Chapter 10 Terrestrial Evaporites. In D. J. Nash & S. J. McLaren (Eds.), *Geochemical sediments and landscapes* (pp. 330–364). Malden, MA: Blackwell Pub.

Clark, R. N. (1983). Spectral properties of mixtures of montmorillonite and dark carbon grains: Implications for remote sensing minerals containing chemically and physically adsorbed water. *Journal of Geophysical Research: Solid Earth*, *88*(B12), 10635–10644. https://doi.org/10.1029/JB088iB12p10635

Clark, R. N. (1999). Spectroscopy of rocks, and minerals and principles of spectroscopy. In *Remote sensing for the earth sciences, manual of remote sensing* (pp. 3–58). New York: John Wiley & Sons.

Clark, R. N., King, T. V. V., Klejwa, M., Swayze, G. A., & Vergo, N. (1990). High spectral resolution reflectance spectroscopy of minerals. *Journal of Geophysical Research: Solid Earth*, *95*(B8), 12653–12680. https://doi.org/10.1029/JB095iB08p12653

Clark, R. N., & Roush, T. L. (1984). Reflectance spectroscopy: Quantitative analysis techniques for remote sensing applications. *Journal of Geophysical Research: Solid Earth*, *89*(B7), 6329–6340. https://doi.org/10.1029/JB089iB07p06329

Clark, R. N., Swayze, G. A., Wise, R., Livo, E., Hoefen, T. M., Kokaly, R. F., & Sutley, S. J. (2007). USGS digital spectral library splib06a: U.S. Geological Survey, Digital Data Series 231. Retrieved from http://speclab.cr.usgs.gov/spectral.lib06

Colditz, R. R., Llamas, R. M., Gebhardt, S., Wehrmann, T., & Equihua, J. (2015). Comparison of change detection techniques for the Yucatan peninsula using Landsat image time series. *2015 IEEE International Geoscience and Remote Sensing Symposium (IGARSS)*, 1650–1653. https://doi.org/10.1109/IGARSS.2015.7326102

Congalton, R. G., & Green, K. (2008). *Assessing the Accuracy of Remotely Sensed Data: Principles and Practices, Second Edition* (2 edition). Boca Raton: CRC Press.

Cooke, R. U., Cooke, R. U., & Warren, A. (1973). *Geomorphology in Deserts*. University of California Press.

Coppin, P., Jonckheere, I., Nackaerts, K., Muys, B., & Lambin, E. (2004). Digital change detection methods in ecosystem monitoring: A review. *International Journal of Remote Sensing*, *25*(9), 1565–1596. https://doi.org/10.1080/0143116031000101675

Crowley, J. K., Hubbard, B. E., & Mars, J. C. (2003). Analysis of potential debris flow source areas on Mount Shasta, California, by using airborne and satellite remote sensing data. *Remote Sensing of Environment*, *87*(2–3), 345–358. https://doi.org/10.1016/j.rse.2003.08.003

Crowley, James K. (1991). Visible and near-infrared (0.4–2.5 µm) reflectance spectra of Playa evaporite minerals. *Journal of Geophysical Research: Solid Earth*, *96*(B10), 16231–16240. https://doi.org/10.1029/91JB01714

Crowley, James K., Brickey, D. W., & Rowan, L. C. (1989). Airborne imaging spectrometer data of the Ruby Mountains, Montana: Mineral discrimination using relative absorption band-depth images. *Remote Sensing of Environment*, *29*(2), 121–134. https://doi.org/10.1016/0034-4257(89)90021-7

Crowley, James K., & Hook, S. J. (1996). Mapping playa evaporite minerals and associated sediments in Death Valley, California, with multispectral thermal infrared images. *Journal of Geophysical Research: Solid Earth*, *101*(B1), 643–660. https://doi.org/10.1029/95JB02813

Crowley, J.K. (1993). Mapping playa evaporite minerals with AVIRIS data: A first report from death valley, California. *Remote Sensing of Environment*, *44*(2–3), 20.

Csavina, J., Field, J., Félix, O., Corral-Avitia, A. Y., Sáez, A. E., & Betterton, E. A. (2014). Effect of Wind Speed and Relative Humidity on Atmospheric Dust Concentrations in Semi-Arid Climates. *The Science of the Total Environment*, *487*, 82–90. https://doi.org/10.1016/j.scitotenv.2014.03.138

Cynthia, A., Evans, A., & Robinson, J. A. (2019). ISS Space Station Orbit. Retrieved 24 August 2019, from https://eol.jsc.nasa.gov/Tools/orbitTutorial.htm

Datt, B., McVicar, T. R., Niel, T. G. V., Jupp, D. L. B., & Pearlman, J. S. (2003). Preprocessing EO-1 Hyperion hyperspectral data to support the application of agricultural indexes. *IEEE Transactions on Geoscience and Remote Sensing*, *41*(6), 1246–1259. https://doi.org/10.1109/TGRS.2003.813206

Davila, A. F., Gomez-Silva, B., de los Rios, A., Ascaso, C., Olivares, H., Mckay, C. P., & Wierzchos, J. (2008). Facilitation of endolithic microbial survival in the hyperarid core of the Atacama Desert by mineral deliquescence. *Journal of Geophysical Research-Biogeosciences*, *113*(G1), G01028. https://doi.org/10.1029/2007JG000561

Dehaan, R. L., & Taylor, G. R. (2001). Mapping irrigation-induced salinity with hyperspectral imagery. *IGARSS 2001. Scanning the Present and Resolving the Future. Proceedings. IEEE 2001 International Geoscience and Remote Sensing Symposium (Cat. No.01CH37217)*, *1*, 293–295 vol.1. https://doi.org/10.1109/IGARSS.2001.976135

Dennison, P. E., & Roberts, D. A. (2003). Endmember selection for multiple endmember spectral mixture analysis using endmember average RMSE. *Remote Sensing of Environment*, *87*(2–3), 123–135. https://doi.org/10.1016/S0034-4257(03)00135-4

Deocampo, D. M., & Jones, B. F. (2014). Geochemistry of Saline Lakes. In *Treatise on Geochemistry* (pp. 437–469). https://doi.org/10.1016/B978-0-08-095975-7.00515-5

DeVries, B., Verbesselt, J., Kooistra, L., & Herold, M. (2015). Robust monitoring of small-scale forest disturbances in a tropical montane forest using Landsat time series. *Remote Sensing of Environment*, *161*, 107–121. https://doi.org/10.1016/j.rse.2015.02.012

Dowling, R., & Newsome, D. (2018). *Handbook of Geotourism*. Edward Elgar Publishing.

Drake, N. A. (1995). Reflectance spectra of evaporite minerals (400-2500 nm): Applications for remote sensing. *International Journal of Remote Sensing*, *16*(14), 2555–2571. https://doi.org/10.1080/01431169508954576

Drake, N. A., Bryant, R. G., Millington, A. C., & Townshend, J. R. G. (1994). Playa Sedimentology and Geomorphology: Mixture Modelling Applied to Landsat Thematic Mapper Data of Chott El Djerid, Tunisia. In R. W. Renaut & W. M. Last (Eds.), *Sedimentology and Geochemistry of Modern and Ancient Saline Lakes*. Retrieved from https://doi.org/10.2110/pec.94.50.0125

Drever, J. I. (2005). *Surface and Ground Water, Weathering, and Soils: Treatise on Geochemistry, Second Edition*. Elsevier.

Drever, James I. (1997). *The Geochemistry of Natural Waters: Surface and Groundwater Environments* (3rd ed.). Upper Saddle River, N.J: Prentice Hall.

Drusch, M., Del Bello, U., Carlier, S., Colin, O., Fernandez, V., Gascon, F., … Bargellini, P. (2012). Sentinel-2: ESA's Optical High-Resolution Mission for GMES Operational Services. *Remote Sensing of Environment*, *120*, 25–36. https://doi.org/10.1016/j.rse.2011.11.026

Ducart, D. F., Silva, A. M., Toledo, C. L. B., & Assis, L. M. de. (2016). Mapping iron oxides with Landsat-8/OLI and EO-1/Hyperion imagery from the Serra Norte iron deposits in the Carajás Mineral Province, Brazil. *Brazilian Journal of Geology*, *46*(3), 331–349. https://doi.org/10.1590/2317-4889201620160023

Dutkiewicz, A., Lewis, M., & Ostendorf, B. (2009). Evaluation and comparison of hyperspectral imagery for mapping surface symptoms of dryland salinity. *International Journal of Remote Sensing*, *30*(3), 693–719. https://doi.org/10.1080/01431160802392612

Dutkiewicz, Anna, Lewis, M., & Ostendorf, B. (2008). The Suitability of Airborne Hyperspectral Imagery for Mapping Surface Indicators of Salinity in Dryland Farming Area. In D. G. Metternicht & D. A. Zinck, *Remote Sensing of Soil Salinization: Impact on Land Management* (pp. 93–112). CRC Press.

Eckardt, F. D., Drake, N. A., Goudie, A. S., White, K., & Viles, H. (2001). The role of playas in pedogenic gypsum crust formation in the Central Namib Desert: A theoretical model. *Earth Surface Processes and Landforms*, *26*(11), 1177–1193. https://doi.org/10.1002/esp.264

Eckardt, Frank D., Bryant, R. G., McCulloch, G., Spiro, B., & Wood, W. W. (2008). The hydrochemistry of a semi-arid pan basin case study: Sua Pan, Makgadikgadi, Botswana. *Applied Geochemistry*, *23*(6), 1563–1580. https://doi.org/10.1016/j.apgeochem.2007.12.033

Eismann, M. (2012). *Hyperspectral Remote Sensing*. Bellingham, Wash: SPIE Press.

Epema, G. F. (1992). *Spectral reflectance in the Tunesian desert | Wda* (PhD thesis). Retrieved from http://library.wur.nl/WebQuery/wda/561145

Etesami, H., Halajian, L., & Jamei, M. (2012). A qualitative land suitability assessment in gypsiferous soils of Kerman Province, Iran. *Australian Journal of Basic and Applied Sciences*, *6*(3), 60–64.

Eugster, H., P., & Hardie, L. A. (1978). Saline Lakes. In A. Lerman (Ed.), *Lakes: Chemistry, Geology, Physics* (pp. 237–293).

FAO (Food and Agriculture Organization of the United Nations) (Ed.). (2006). *World Reference Base for Soil Resources, 2006*. Retrieved from https://books.google.de/books/about/World_Reference_Base_for_Soil_Resources.html?hl=de&id=1ORkZtTHYBsC

Farifteh, J., Meer, F. van der, & Carranza, E. J. M. (2007). Similarity measures for spectral discrimination of salt-affected soils. *International Journal of Remote Sensing*, *28*(23), 5273–5293. https://doi.org/10.1080/01431160701227604

Farifteh, J., van der Meer, F., van der Meijde, M., & Atzberger, C. (2008). Spectral characteristics of salt-affected soils: A laboratory experiment. *Geoderma*, *145*(3–4), 196–206. https://doi.org/10.1016/j.geoderma.2008.03.011

Feingersh, T., & Ben-Dor, E. (2015). SHALOM - A Commercial Hyperspectral Space Mission. In S.-E. Qian (Ed.), *Optical Payloads for Space Missions* (pp. 247–263). https://doi.org/10.1002/9781118945179.ch11

Ferrier, G., & Wadge, G. (1996). The application of imaging spectrometry data to mapping alteration zones associated with gold mineralization in southern Spain. *International Journal of Remote Sensing*, *17*(2), 331–350. https://doi.org/10.1080/01431169608949009

Field, J. P., Belnap, J., Breshears, D. D., Neff, J. C., Okin, G. S., Whicker, J. J., … Reynolds, R. L. (2010). The ecology of dust. *Frontiers in Ecology and the Environment*, *8*(8), 423–430. https://doi.org/10.1890/090050

Finstad, K., Pfeiffer, M., McNicol, G., Barnes, J., Demergasso, C., Chong, G., & Amundson, R. (2016). Rates and geochemical processes of soil and salt crust formation in Salars of the Atacama Desert, Chile. *Geoderma*, *284*, 57–72. https://doi.org/10.1016/j.geoderma.2016.08.020

Flahaut, J., Martinot, M., Bishop, J. L., Davies, G. R., & Potts, N. J. (2017). Remote sensing and in situ mineralogic survey of the Chilean salars: An analog to Mars evaporate deposits? *Icarus*, *282*, 152–173. https://doi.org/10.1016/j.icarus.2016.09.041

Fookes, P. G., & Lee, E. M. (2018). The engineering geology of playas, salt playas and salinas. *Quarterly Journal of Engineering Geology and Hydrogeology*, *51*(2), 287–298. https://doi.org/10.1144/qjegh2017-084

Franks, S., Neigh, C. S. R., Campbell, P. K., Sun, G., Yao, T., Zhang, Q., … Frye, S. W. (2017). EO-1 Data Quality and Sensor Stability with Changing Orbital Precession at the End of a 16 Year Mission. *Remote Sensing*, *9*(5), 412. https://doi.org/10.3390/rs9050412

Frie, A. L., Dingle, J. H., Ying, S. C., & Bahreini, R. (2017). The Effect of a Receding Saline Lake (The Salton Sea) on Airborne Particulate Matter Composition. *Environmental Science & Technology*, *51*(15), 8283–8292. https://doi.org/10.1021/acs.est.7b01773

Funakawa, S., Suzuki, R., Karbozova, E., Kosaki, T., & Ishida, N. (2000). Salt-affected soils under rice-based irrigation agriculture in southern Kazakhstan. *Geoderma*, *97*(1), 61–85. https://doi.org/10.1016/S0016-7061(00)00026-4

Gao, B. (1996). NDWI—A normalized difference water index for remote sensing of vegetation liquid water from space. *Remote Sensing of Environment*, *58*(3), 257–266. https://doi.org/10.1016/S0034-4257(96)00067-3

Garcia-Haro, F. J., Gilabert, M. A., & Melia, J. (1996). Linear spectral mixture modelling to estimate vegetation amount from optical spectral data. *International Journal of Remote Sensing*, *17*(17), 3373–3400.

Garrett, D. E. (2001). *Sodium Sulfate: Handbook of Deposits, Processing, & Use* (1 edition). San Diego: Academic Press.

Ge, Y., Abuduwaili, J., Ma, L., Wu, N., & Liu, D. (2016). Potential transport pathways of dust emanating from the playa of Ebinur Lake, Xinjiang, in arid northwest China. *Atmospheric Research*, *178*, 196–206. https://doi.org/10.1016/j.atmosres.2016.04.002

Genderjahn, S., Alawi, M., Wagner, D., Schüller, I., Wanke, A., & Mangelsdorf, K. (2018). Microbial Community Responses to Modern Environmental and Past Climatic Conditions in Omongwa Pan, Western Kalahari: A Paired 16S rRNA Gene Profiling and Lipid Biomarker Approach. *Journal of Geophysical Research: Biogeosciences*. https://doi.org/10.1002/2017JG004098

Genderjahn, Steffi, Alawi, M., Kallmeyer, J., Belz, L., Wagner, D., & Mangelsdorf, K. (2017). Present and past microbial life in continental pan sediments and its response to climate variability in the southern Kalahari. *Organic Geochemistry*, *108*, 30–42. https://doi.org/10.1016/j.orggeochem.2017.04.001

German Institute for Standardization (Ed.). (1997, June). *Soil quality—Determination of the specific electrical conductivity (ISO 11265:1994 + ISO 11265:1994/Corr.1:1996)*. Retrieved from https://www.beuth.de/de/norm/din-iso-11265/2965336

German Institute for Standardization (Ed.). (2002, August). *Soil quality—Determination of particle size distribution in mineral soil material—Method by sieving and sedimentation (ISO 11277:1998 + ISO 11277:1998 Corrigendum 1:2002)*. Retrieved from https://www.beuth.de/en/standard/din-iso-11277/53934894

Ghosh, G., Kumar, S., & Saha, S. K. (2012). Hyperspectral Satellite Data in Mapping Salt-Affected Soils Using Linear Spectral Unmixing Analysis. *Journal of the Indian Society of Remote Sensing*, *40*(1), 129–136. https://doi.org/10.1007/s12524-011-0143-x

Ghrefat, H. A., & Goodell, P. C. (2011). Land cover mapping at Alkali Flat and Lake Lucero, White Sands, New Mexico, USA using multi-temporal and multi-spectral remote sensing data. *International Journal of Applied Earth Observation and Geoinformation*, *13*(4), 616–625. https://doi.org/10.1016/j.jag.2011.03.009

Gillette, D. A., Adams, J., Endo, A., Smith, D., & Kihl, R. (1980). Threshold velocities for input of soil particles into the air by desert soils. *Journal of Geophysical Research*, *85*(C10), 5621. https://doi.org/10.1029/JC085iC10p05621

Girouard, G., Bannari, A., El Harti, A., & Desrochers, A. (2004). Validated spectral angle mapper algorithm for geological mapping: Comparative study between QuickBird and Landsat-TM. *XXth ISPRS Congress, Geo-Imagery Bridging Continents, Istanbul, Turkey*, 12–23.

Gleeson, D. F., Pappalardo, R. T., Grasby, S. E., Anderson, M. S., Beauchamp, B., Castaño, R., … Wagstaff, K. L. (2010). Characterization of a sulfur-rich Arctic spring site and field analog to Europa using hyperspectral data. *Remote Sensing of Environment*, *114*(6), 1297–1311. https://doi.org/10.1016/j.rse.2010.01.011

Godfrey, L. V., Chan, L.-H., Alonso, R. N., Lowenstein, T. K., McDonough, W. F., Houston, J., … Jordan, T. E. (2013). The role of climate in the accumulation of lithium-rich brine in the Central Andes. *Applied Geochemistry*, *38*, 92–102. https://doi.org/10.1016/j.apgeochem.2013.09.002

Gorelick, N., Hancher, M., Dixon, M., Ilyushchenko, S., Thau, D., & Moore, R. (2017). Google Earth Engine: Planetary-scale geospatial analysis for everyone. *Remote Sensing of Environment*. https://doi.org/10.1016/j.rse.2017.06.031

Goudie, A. S., & Thomas, D. S. G. (1985). Pans in southern Africa with particular reference to South Africa and Zimbabwe. *Zeitschrift Für Geomorphologie*, *29*(1), 1–19.

Goudie, A. S., & Wells, G. L. (1995). The nature, distribution and formation of pans in arid zones. *Earth-Science Reviews*, *38*(1), 1–69. https://doi.org/10.1016/0012-8252(94)00066-6

Grant, S. A., & Bachmann, J. (2013). Effect of Temperature on Capillary Pressure. In *Environmental Mechanics* (pp. 199–212). https://doi.org/10.1029/129GM18

Green, A. A., Berman, M., Switzer, P., & Craig, M. D. (1988). A transformation for ordering multispectral data in terms of image quality with implications for noise removal. *IEEE Transactions on Geoscience and Remote Sensing*, *26*(1), 65–74. https://doi.org/10.1109/36.3001

Green, R. (2018). *The Earth Surface Mineral Dust Source Investigation (EMIT)*. Presented at the 2018 HyspIRI Science and Applications Workshop, Washington, DC. Retrieved from https://hyspiri.jpl.nasa.gov/downloads/2018_Workshop/day1/13_HyspIRI_EMIT_Overview_20180815b.pdf

Green, R., Mahowald, N., Thompson, D., Clark, R., Ehlmann, B., Ginoux, P., … Dor, E. B. (2019). The Earth Surface Mineral Dust Source Investigation Planned for the International Space Station. *Geophysical Research Abstracts*, 1. Vienna.

Green, R. O., Pavri, B. E., & Chrien, T. G. (2003). On-orbit radiometric and spectral calibration characteristics of EO-1 Hyperion derived with an underflight of AVIRIS and in situ measurements at Salar de Arizaro, Argentina. *IEEE Transactions on Geoscience and Remote Sensing*, *41*(6), 1194–1203. https://doi.org/10.1109/TGRS.2003.813204

Greenspan, L. (1977). Humidity fixed points of binary saturated aqueous solutions. *Journal of Research of the National Bureau of Standards Section A: Physics and Chemistry*, *81A*(1), 89. https://doi.org/10.6028/jres.081A.011

Gruninger, J. H., Ratkowski, A. J., & Hoke, M. L. (2004, August 12). *The sequential maximum angle convex cone (SMACC) endmember model*. *5425*, 1–15. https://doi.org/10.1117/12.543794

Guanter, L., Brell, M., Chan, J. C.-W., Giardino, C., Gomez-Dans, J., Mielke, C., … Yokoya, N. (2018). Synergies of Spaceborne Imaging Spectroscopy with Other Remote Sensing Approaches. *Surveys in Geophysics*. https://doi.org/10.1007/s10712-018-9485-z

Guanter, L., Kaufmann, H., Segl, K., Foerster, S., Rogass, C., Chabrillat, S., … Sang, B. (2015). The EnMAP Spaceborne Imaging Spectroscopy Mission for Earth Observation. *Remote Sensing*, *7*(7), 8830–8857. https://doi.org/10.3390/rs70708830

Guanter, L., Richter, R., & Kaufmann, H. (2009). On the application of the MODTRAN4 atmospheric radiative transfer code to optical remote sensing. *International Journal of Remote Sensing*, *30*(6), 1407–1424. https://doi.org/10.1080/01431160802438555

Guanter, L., Segl, K., Sang, B., Alonso, L., Kaufmann, H., & Moreno, J. (2009). Scene-based spectral calibration assessment of high spectral resolution imaging spectrometers. *Optics Express*, *17*(14), 11594. https://doi.org/10.1364/OE.17.011594

Hardie, L. A. (1968). The origin of the Recent non-marine evaporite deposit of Saline Valley, Inyo County, California. *Geochimica et Cosmochimica Acta*, *32*(12), 1279–1301. https://doi.org/10.1016/0016-7037(68)90029-X

Harris Geospatial Solutions. (2014). *Using SMACC to Extract Endmembers* (p. 12) [Tutorial]. Retrieved from http://www.harrisgeospatial.com/portals/0/pdfs/envi/SMACC.pdf

Harris Geospatial Solutions. (2015). Linear Spectral Unmixing (Using ENVI). Retrieved 4 February 2016, from http://www.exelisvis.com/docs/LinearSpectralUnmixing.html

Haubrock, S.-N., Chabrillat, S., Kuhnert, M., Hostert, P., & Kaufmann, H. (2008). Surface soil moisture quantification and validation based on hyperspectral data and field measurements. *Journal of Applied Remote Sensing*, *2*(1), 023552-023552–26. https://doi.org/10.1117/1.3059191

Herrero, J., Artieda, O., & Hudnall, W. H. (2009). Gypsum, a Tricky Material. *Soil Science Society of America Journal*, *73*(6), 1757–1763. https://doi.org/10.2136/sssaj2008.0224

Hersbach, H., & Dee, D. (2016). *ERA5 reanalysis is in production* (No. 147). Retrieved from ECMWF website: https://www.ecmwf.int/en/newsletter/147/news/era5-reanalysis-production

Hoja, D., Krauss, T., & Reinartz, P. (2013). Detailed damage assessment after the Haiti earthquake. In *Earth Observation of Global Changes (EOGC)* (pp. 193–204). Retrieved from http://link.springer.com/chapter/10.1007/978-3-642-32714-8_13

Hook, S. (2019). ECOSTRESS. Retrieved 24 August 2019, from https://ecostress.jpl.nasa.gov

Howari, F. M., Goodell, P. C., & Miyamoto, S. (2002). Spectral properties of salt crusts formed on saline soils. *Journal of Environmental Quality*, *31*(5), 1453–1461.

Howari, Fares M., Goodell, P. C., & Miyamoto, S. (2002). Spectroscopy of Salts Common in Saline Soils. In R. S. Muttiah (Ed.), *From Laboratory Spectroscopy to Remotely Sensed Spectra of Terrestrial Ecosystems* (pp. 1–20). https://doi.org/10.1007/978-94-017-1620-8_1

Hubbard, B. E., & Crowley, J. K. (2005). Mineral mapping on the Chilean–Bolivian Altiplano using co-orbital ALI, ASTER and Hyperion imagery: Data dimensionality issues and solutions. *Remote Sensing of Environment*, *99*(1–2), 173–186. https://doi.org/10.1016/j.rse.2005.04.027

Hunt, G. R., Salisbury, J. W., & Lenhoff, C. J. (1971). Visible and near infrared spectra of minerals and rocks, IV Sulphides and sulphates. *Modern Geology*, *3*, 121–132.

JICA STUDY TEAM. (2002). *The Study on the Groundwater Potential Evaluation and Management Plan in the Southeast Kalahari(Stampriet) Artesian Basin in the Republic of Namibia: Final Report : Data Book*. Pacific Consultants International.

Jollineau, M. Y., & Howarth, P. J. (2008). Mapping an inland wetland complex using hyperspectral imagery. *International Journal of Remote Sensing*, *29*(12), 3609–3631. https://doi.org/10.1080/01431160701469099

Jones, B. F. (1965). *The hydrology and mineralogy of Deep Springs Lake, Inyo County, California* (USGS Numbered Series No. 502-A). Retrieved from U.S. Govt. Print. Off., website: http://pubs.er.usgs.gov/publication/pp502A

Jones, S. K., Fremier, A. K., DeClerck, F. A., Smedley, D., Ortega Pieck, A., & Mulligan, M. (2017). Big Data and Multiple Methods for Mapping Small Reservoirs: Comparing Accuracies for Applications in Agricultural Landscapes. *Remote Sensing*, *9*(12), 1307. https://doi.org/10.3390/rs9121307

Ju, J., & Roy, D. P. (2008). The availability of cloud-free Landsat ETM+ data over the conterminous United States and globally. *Remote Sensing of Environment*, *112*(3), 1196–1211. https://doi.org/10.1016/j.rse.2007.08.011

Jupp, D. L. B. (2001). Discussion around Hyperion Data. *CSIRO Office of Space Science & Applications Earth Observation Centre, Canberra*, 9.

Katra, I., & Lancaster, N. (2008). Surface-sediment dynamics in a dust source from spaceborne multispectral thermal infrared data. *Remote Sensing of Environment*, *112*(7), 3212–3221. https://doi.org/10.1016/j.rse.2008.03.016

Kaufman, Y. J., Wald, A. E., Remer, L. A., Gao, B.-C., Li, R.-R., & Flynn, L. (1997). The MODIS 2.1- mu;m channel-correlation with visible reflectance for use in remote sensing of aerosol. *IEEE Transactions on Geoscience and Remote Sensing*, *35*(5), 1286–1298. https://doi.org/10.1109/36.628795

Kautz, K., & Parada, H. (1976). Sepiolote formation in a pan of the Kalahari, South West Africa. *Journal of Mineralogy and Geochemistry*, *12*, 545–559.

Kavanagh, L., Keohane, J., Garcia Cabellos, G., Lloyd, A., & Cleary, J. (2018). Global Lithium Sources—Industrial Use and Future in the Electric Vehicle Industry: A Review. *Resources*, *7*(3), 57. https://doi.org/10.3390/resources7030057

Kelly, J. T., & Gontz, A. M. (2018). Using GPS-surveyed intertidal zones to determine the validity of shorelines automatically mapped by Landsat water indices. *International Journal of Applied Earth Observation and Geoinformation*, *65*, 92–104. https://doi.org/10.1016/j.jag.2017.10.007

Khayamim, F., Wetterlind, J., Khademi, H., Robertson, J., Faz Cano, A., & Stenberg, B. (2015). Using visible and near infrared spectroscopy to estimate carbonates and gypsum in soils in arid and subhumid regions of Isfahan, Iran. *Journal of Near Infrared Spectroscopy*, *23*(3), 155. https://doi.org/10.1255/jnirs.1157

King, J., Etyemezian, V., Sweeney, M., Buck, B. J., & Nikolich, G. (2011). Dust emission variability at the Salton Sea, California, USA. *Aeolian Research*, *3*(1), 67–79. https://doi.org/10.1016/j.aeolia.2011.03.005

Klimchouk, A. (1996). The dissolution and conversion of gypsum and anhydrite. *International Journal of Speleology*, *25*(3). https://doi.org/ http://dx.doi.org/10.5038/1827-806X.25.3.2

Kodikara, G. R. L. (2009). *Hyperspectral mapping of surface mineralogy in the Lake Magadi area in Kenya* (Master Thesis, ITC). Retrieved from https://www.itc.nl/library/papers_2009/msc/aes/loku.pdf

Kodikara, G. R. L., Woldai, T., van Ruitenbeek, F. J. A., Kuria, Z., van der Meer, F., Shepherd, K. D., & van Hummel, G. J. (2012). Hyperspectral remote sensing of evaporate minerals and associated sediments in Lake Magadi area, Kenya. *International Journal of Applied Earth Observation and Geoinformation*, *14*(1), 22–32. https://doi.org/10.1016/j.jag.2011.08.009

Kokaly, R. F., & Clark, R. N. (1999). Spectroscopic Determination of Leaf Biochemistry Using Band-Depth Analysis of Absorption Features and Stepwise Multiple Linear Regression. *Remote Sensing of Environment*, *67*(3), 267–287. https://doi.org/10.1016/S0034-4257(98)00084-4

Kokaly, R. F., King, T. V., & Hoefen, T. M. (2011). Mapping the distribution of materials in hyperspectral data using the USGS Material Identification and Characterization Algorithm (MICA). *Geoscience and Remote Sensing Symposium (IGARSS), 2011 IEEE International*, 1569–1572.

Köppen, W. P., & Geiger, R. (1930). *Handbuch der Klimatologie in fünf bänden*. Berlin: Verlag von Gebrüder Borntraeger.

Kruse, F. A., Boardman, J. W., & Huntington, J. F. (2003). Comparison of airborne hyperspectral data and EO-1 Hyperion for mineral mapping. *IEEE Transactions on Geoscience and Remote Sensing*, *41*(6), 1388–1400. https://doi.org/10.1109/TGRS.2003.812908

Kruse, F. A., Boardman, J. W., Huntington, J. F., Mason, P., & Quigley, M. A. (2002). Evaluation and validation of EO-1 Hyperion for geologic mapping. *Geoscience and Remote Sensing Symposium, 2002. IGARSS'02. 2002 IEEE International*, *1*, 593–595. Retrieved from http://ieeexplore.ieee.org/abstract/document/1025115/

Kruse, F., Lefkoff, A., & Dietz, J. (1993). Expert System-Based Mineral Mapping in Northern Death-Valley, California Nevada, Using the Airborne Visible Infrared Imaging Spectrometer (aviris). *Remote Sensing of Environment*, *44*(2–3), 309–336. https://doi.org/10.1016/0034-4257(93)90024-R

Kühn, F., Oppermann, K., & Hörig, B. (2004). Hydrocarbon Index – an algorithm for hyperspectral detection of hydrocarbons. *International Journal of Remote Sensing*, *25*(12), 2467–2473. https://doi.org/10.1080/01431160310001642287

Lancaster, N. (1978). The Pans of the Southern Kalahari, Botswana. *The Geographical Journal*, *144*(1), 81–98. https://doi.org/10.2307/634651

Lancaster, N. (1986). Pans in the southwestern Kalahari. A preliminary report. *Palaeoecology of Africa*, *17*, 59–68.

Lancaster, N. (2009). Aeolian features and processes. In R. Young & L. Norby (Series Ed.), *Geological Monitoring* (pp. 1–25). Boulder, Colorado, U.S.: The Geological Society of America.

Landis, J. R., & Koch, G. G. (1977). The Measurement of Observer Agreement for Categorical Data. *Biometrics*, *33*(1), 159–174. https://doi.org/10.2307/2529310

Lee, J.-E., Seo, D.-H., Ro, H.-M., & Yun, S.-I. (2016). Yield Response of Chinese Cabbage to Compost, Gypsum, and Phosphate Treatments under the Saline-sodic Soil Conditions of Reclaimed Tidal Land. *Korean Journal of Horticultural Science & Technology*, *34*(4), 587–595. https://doi.org/10.12972/kjhst.20160060

Levin, N., Kidron, G. J., & Ben-Dor, E. (2007). Surface properties of stabilizing coastal dunes: Combining spectral and field analyses. *Sedimentology*, *54*(4), 771–788. https://doi.org/10.1111/j.1365-3091.2007.00859.x

Li, D., Chen, X., Peng, Z., Chen, S., Chen, W., Han, L., & Li, Y. (2012). Prediction of soil organic matter content in a litchi orchard of South China using spectral indices. *Soil and Tillage Research*, *123*, 78–86. https://doi.org/10.1016/j.still.2012.03.013

Li, J., Menenti, M., Mousivand, A., & Luthi, S. M. (2014). Non-Vegetated Playa Morphodynamics Using Multi-Temporal Landsat Imagery in a Semi-Arid Endorheic Basin: Salar de Uyuni, Bolivia. *Remote Sensing*, *6*(10), 10131–10151. https://doi.org/10.3390/rs61010131

Li, W., Du, Z., Ling, F., Zhou, D., Wang, H., Gui, Y., … Zhang, X. (2013). A Comparison of Land Surface Water Mapping Using the Normalized Difference Water Index from TM, ETM+ and ALI. *Remote Sensing*, *5*(11), 5530–5549. https://doi.org/10.3390/rs5115530

Liang, W., Hoja, D., Schmitt, M., & Stilla, U. (2011). *Change Detection for Reconstruction Monitoring based on Very High Resolution Optical Data*. Retrieved from http://www.researchgate.net/profile/Uwe_Stilla/publication/225007329_Change_Detection_for_Reconstruction_Monitoring_based_on_Very_High_Resolution_Optical_Data/links/00b4951e6ae8a247ea000000.pdf

Liao, M., Zhu, P., & Gong, J. (2000). Multivariate Change Detection Based on Canonical Transformation. *Journal of Remote Sensing*, *4*(3), 197–201.

Liu, C.-A., Gong, H., Shao, Y., Yang, Z., Liu, L., & Geng, Y. (2016). Recognition of salt crust types by means of PolSAR to reflect the fluctuation processes of an ancient lake in Lop Nur. *Remote Sensing of Environment*, *175*, 148–157. https://doi.org/10.1016/j.rse.2015.12.034

Loizzo, R., Guarini, R., Longo, F., Scopa, T., Formaro, R., Facchinetti, C., & Varacalli, G. (2018). Prisma: The Italian Hyperspectral Mission. In *Igarss 2018—2018 Ieee International Geoscience and Remote Sensing Symposium* (pp. 175–178). New York: Ieee.

Lopinto, E., Daraio, M. G., Guarini, R., & Loizzo, R. (2019). *Prisma Mission Management and Operation Strategy*. 1. Milan, Italy.

Lowenstein, T. K., & Hardie, L. A. (1985). Criteria for the recognition of salt-pan evaporites. *Sedimentology*, *32*(5), 627–644.

Lu, H., & Shao, Y. (2001). Toward quantitative prediction of dust storms: An integrated wind erosion modelling system and its applications. *Environmental Modelling & Software*, *16*(3), 233–249. https://doi.org/10.1016/S1364-8152(00)00083-9

Ma, L., Liu, Y., Zhang, X., Ye, Y., Yin, G., & Johnson, B. A. (2019). Deep learning in remote sensing applications: A meta-analysis and review. *ISPRS Journal of Photogrammetry and Remote Sensing*, *152*, 166–177. https://doi.org/10.1016/j.isprsjprs.2019.04.015

Ma, Y., Chen, F., Liu, J., He, Y., Duan, J., & Li, X. (2016). An Automatic Procedure for Early Disaster Change Mapping Based on Optical Remote Sensing. *Remote Sensing*, *8*(4), 272. https://doi.org/10.3390/rs8040272

Maidment, R. I., Grimes, D., Allan, R. P., Tarnavsky, E., Stringer, M., Hewison, T., … Black, E. (2014). The 30 year TAMSAT African Rainfall Climatology And Time series (TARCAT) data set. *Journal of Geophysical Research: Atmospheres*, *119*(18), 2014JD021927. https://doi.org/10.1002/2014JD021927

Maiersperger, T. K., Scaramuzza, P. L., Leigh, L., Shrestha, S., Gallo, K. P., Jenkerson, C. B., & Dwyer, J. L. (2013). Characterizing LEDAPS surface reflectance products by comparisons with AERONET, field spectrometer, and MODIS data. *Remote Sensing of Environment*, *136*, 1–13. https://doi.org/10.1016/j.rse.2013.04.007

Masek, J. G., Vermote, E. F., Saleous, N. E., Wolfe, R., Hall, F. G., Huemmrich, K. F., … Lim, T.-K. (2006). A Landsat surface reflectance dataset for North America, 1990-2000. *IEEE Geoscience and Remote Sensing Letters*, *3*(1), 68–72. https://doi.org/10.1109/LGRS.2005.857030

Masek, J. G., Vermote, E. F., Saleous, N. E., Wolfe, R., Hall, F. G., Huemmrich, K. F., … Lim, T.-K. (2013). *LEDAPS Calibration, Reflectance, Atmospheric Correction Preprocessing Code, Version 2*. https://doi.org/10.3334/ORNLDAAC/1146

Matter, A., & Tucker, M. E. (1978). Modern and Ancient Lake Sediments: An Introduction. In *Modern and Ancient Lake Sediments* (pp. 1–6). https://doi.org/10.1002/9781444303698.ch1

Meer, F. D. van der, & Jong, S. M. de. (2007). *Imaging Spectrometry: Basic Principles and Prospective Applications*. Springer Science & Business Media.

Mees, F. (1999). Distribution patterns of gypsum and kalistrontite in a dry lake basin of the southwestern Kalahari (Omongwa pan, Namibia). *Earth Surface Processes and Landforms*, *24*(8), 731–744. https://doi.org/10.1002/(SICI)1096-9837(199908)24:8<731::AID-ESP7>3.0.CO;2-0

Mees, F. (2002). The nature of calcareous deposits along pan margins in eastern central Namibia. *Earth Surface Processes and Landforms*, *27*(7), 719–735. https://doi.org/10.1002/esp.348

Mees, F., Casteñeda, C., Herrero, J., & Ranst, E. V. (2012). The Nature and Significance of Variations In Gypsum Crystal Morphology In Dry Lake Basins. *Journal of Sedimentary Research*, *82*(1), 37–52. https://doi.org/10.2110/jsr.2012.3

Mees, F., Hatert, F., & Rowe, R. (2008). Omongwaite, Na2Ca5(SO4)(6)*3H(2)O, a new mineral from recent salt lake deposits, Namibia. *Mineralogical Magazine*, *72*(6), 1307–1318. https://doi.org/10.1180/minmag.2008.072.6.1307

Mees, F., & Singer, A. (2006). Surface crusts on soils/sediments of the southern Aral Sea basin, Uzbekistan. *Geoderma*, *136*(1), 152–159. https://doi.org/10.1016/j.geoderma.2006.03.019

Mees, F., & Van Ranst, E. (2011). Micromorphology of sepiolite occurrences in recent lacustrine deposits affected by soil development. *Soil Research*, *49*(6), 547–557. https://doi.org/10.1071/SR11087

Melvin, J. L. (1991). *Evaporites, Petroleum and Mineral Resources*. Elsevier.

Metternicht, G. I., & Fermont, A. (1998). Estimating erosion surface features by linear mixture modeling. *Remote Sensing of Environment*, *64*(3), 254–265. https://doi.org/10.1016/S0034-4257(97)00172-7

Metternicht, G. I., & Zinck, J. A. (2003). Remote sensing of soil salinity: Potentials and constraints. *Remote Sensing of Environment*, *85*(1), 1–20. https://doi.org/10.1016/S0034-4257(02)00188-8

Mezned, N., Dkhala, B., & Abdeljaouad, S. (2015). Multi temporal and multi spectral images based change detection of mine wastes in Northern Tunisia. *2015 IEEE International Geoscience and Remote Sensing Symposium (IGARSS)*, 3426–3429. https://doi.org/10.1109/IGARSS.2015.7326556

Mielke, C., Muedi, T., Papenfuss, A., Boesche, N. K., Rogass, C., Gauert, C. D. K., … Wit, M. J. de. (2016). Multi- and hyperspectral spaceborne remote sensing of the Aggeneys base metal sulphide mineral deposit sites in the Lower Orange River region, South Africa. *South African Journal of Geology*, *119*(1), 63–76. https://doi.org/10.2113/gssajg.119.1.63

Mielke, C., Rogass, C., Boesche, N., Segl, K., & Altenberger, U. (2016). EnGeoMAP 2.0—Automated Hyperspectral Mineral Identification for the German EnMAP Space Mission. *Remote Sensing*, *8*(2), 127. https://doi.org/10.3390/rs8020127

Milewski, R., Chabrillat, S., & Behling, R. (2017). Analyses of Recent Sediment Surface Dynamic of a Namibian Kalahari Salt Pan Based on Multitemporal Landsat and Hyperspectral Hyperion Data. *Remote Sensing*, *9*(2), 170. https://doi.org/10.3390/rs9020170

Miller, R. M. (2008). *The Geology of Namibia: Upper palaeozoic to cenozoic*. Ministry of Mines and Energy, Geological Survey.

Millington, A. C., Drake, N. A., Townshend, J. R. G., Quarmby, N. A., Settle, J. J., & Reading, A. J. (1989). Monitoring salt playa dynamics using Thematic Mapper data. *IEEE Transactions on Geoscience and Remote Sensing*, *27*(6), 754–761. https://doi.org/10.1109/36.35964

Millington, A. C., Jones, A. R., Quarmby, N., & Townshend, J. R. G. (1987). Remote sensing of sediment transfer processes in playa basins. *Geological Society, London, Special Publications*, *35*(1), 369–381. https://doi.org/10.1144/GSL.SP.1987.035.01.25

Moret-Fernández, D., & Herrero, J. (2015). Effect of gypsum content on soil water retention. *Journal of Hydrology*, *528*, 122–126. https://doi.org/10.1016/j.jhydrol.2015.06.030

Mulder, V. L., de Bruin, S., Schaepman, M. E., & Mayr, T. R. (2011). The use of remote sensing in soil and terrain mapping—A review. *Geoderma*, *162*(1–2), 1–19. https://doi.org/10.1016/j.geoderma.2010.12.018

Murphy, R. J. (2015). Evaluating simple proxy measures for estimating depth of the ~1900nm water absorption feature from hyperspectral data acquired under natural illumination. *Remote Sensing of Environment*, *166*, 22–33. https://doi.org/10.1016/j.rse.2015.05.029

Mustard, J. F., & Sunshine, J. M. (1999). Spectral Analysis for Earth Science: Investigations Using Remote Sensing Data. In R. A. Ryerson & A. N. Rencz (Eds.), *Remote sensing for the earth sciences: Manual of remote sensing* (3rd ed., Vol. 3, pp. 251–307).

Mutanga, O., & Kumar, L. (2019). Google Earth Engine Applications. *Remote Sensing*, *11*(5), 591. https://doi.org/10.3390/rs11050591

Namibian Ministries of Agriculture, Basic Education and Health, office Aminuis. (2015). *Obervation of precipitation at Aminuis* [Personal communication].

Neal, J. T. (1975). Playa surface features as indicators of environment. In J. T. Neal (Ed.), *Playas and Dried Lakes* (Benchmark Papers in Geology, Halsted Press, pp. 363–380). Stroudsburg, Pennsylvania, U.S.: Dowden, Hutchinson & Ross.

Nickling, W. G., & Ecclestone, M. (1981). The effects of soluble salts on the threshold shear velocity of fine sand. *Sedimentology*, *28*(4), 505–510. https://doi.org/10.1111/j.1365-3091.1981.tb01698.x

Nieke, J., & Rast, M. (2018). Towards the Copernicus Hyperspectral Imaging Mission For The Environment (CHIME). *IGARSS 2018 - 2018 IEEE International Geoscience and Remote Sensing Symposium*, 157–159. https://doi.org/10.1109/IGARSS.2018.8518384

Nield, J. M., Bryant, R. G., Wiggs, G. F. S., King, J., Thomas, D. S. G., Eckardt, F. D., & Washington, R. (2015). The dynamism of salt crust patterns on playas. *Geology*, *43*(1), 31–34. https://doi.org/10.1130/G36175.1

Nield, J. M., Wiggs, G. F. S., King, J., Bryant, R. G., Eckardt, F. D., Thomas, D. S. G., & Washington, R. (2016). Climate–surface–pore-water interactions on a salt crusted playa: Implications for crust pattern and surface roughness development measured using terrestrial laser scanning. *Earth Surface Processes and Landforms*, *41*(6), 738–753. https://doi.org/10.1002/esp.3860

Nielsen, Allan A., Conradsen, K., & Simpson, J. J. (1998). Multivariate Alteration Detection (MAD) and MAF Postprocessing in Multispectral, Bitemporal Image Data: New Approaches to Change Detection Studies. *Remote Sensing of Environment*, *64*(1), 1–19. https://doi.org/10.1016/S0034-4257(97)00162-4

Nielsen, Allan Aasbjerg. (1994). *Analysis of regularly and irregularly sampled spatial, multivariate, and multi-temporal data* (Technical University of Denmark). Retrieved from http://www2.compute.dtu.dk/~alan/phd/phd-no-figs.pdf

Nielsen, Allan Aasbjerg. (2007). The Regularized Iteratively Reweighted MAD Method for Change Detection in Multi- and Hyperspectral Data. *IEEE Transactions on Image Processing*, *16*(2), 463–478. https://doi.org/10.1109/TIP.2006.888195

Nielsen, Allan Aasbjerg, Hecheltjen, A., Thonfeld, F., Canty, M. J., & others. (2010). Automatic change detection in RapidEye data using the combined MAD and kernel MAF methods. *IGARSS*, 3078–3081. Retrieved from http://www.researchgate.net/profile/Frank_Thonfeld/publication/220822622_Automatic_change_detection_in_RapidEye_data_using_the_combined_MAD_and_kernel_MAF_methods/links/02e7e534514b6ad69c000000.pdf

Norsk Elektro Optikk. (2017). HySpex Main Specifications. Retrieved 15 June 2017, from http://www.hyspex.no/products/all_specs.php

Okada, K., & Iwashita, A. (1992). Hyper-multispectral image analysis based on waveform characteristics of spectral curve. *Advances in Space Research*, *12*(7), 433–442. https://doi.org/10.1016/0273-1177(92)90250-2

Parris, R., & Child, G. (1979). The importance of pans to wildlife in the Kalahari and the effect of human settlement on these areas. *South African Journal of Wildlife Research*, *3*(1), 1–8.

Pathak, S. (2014). New Change Detection Techniques to monitor land cover dynamics in mine environment. *ISPRS - International Archives of the Photogrammetry, Remote Sensing and Spatial Information Sciences*, *XL–8*, 875–879. https://doi.org/10.5194/isprsarchives-XL-8-875-2014

Pearlman, J. S., Barry, P. S., Segal, C. C., Shepanski, J., Beiso, D., & Carman, S. L. (2003). Hyperion, a space-based imaging spectrometer. *IEEE Transactions on Geoscience and Remote Sensing*, *41*(6), 1160–1173. https://doi.org/10.1109/TGRS.2003.815018

Pelletier, J. D. (2006). Sensitivity of playa windblown-dust emissions to climatic and anthropogenic change. *Journal of Arid Environments*, *66*(1), 62–75. https://doi.org/10.1016/j.jaridenv.2005.10.010

Peon, J., Recondo, C., Fernandez, S., Calleja, J. F., De Miguel, E., & Carretero, L. (2017). Prediction of Topsoil Organic Carbon Using Airborne and Satellite Hyperspectral Imagery. *Remote Sensing*, *9*(12), 1211. https://doi.org/10.3390/rs9121211

Pesaran, M. H., & Timmermann, A. (2002). Market timing and return prediction under model instability. *Journal of Empirical Finance*, *9*(5), 495–510. https://doi.org/10.1016/S0927-5398(02)00007-5

Pignatti, S., Acito, N., Amato, U., Casa, R., Castaldi, F., Coluzzi, R., … Cuomo, V. (2015). Environmental products overview of the Italian hyperspectral prisma mission: The SAP4PRISMA project. *2015 IEEE International Geoscience and Remote Sensing Symposium (IGARSS)*, 3997–4000. https://doi.org/10.1109/IGARSS.2015.7326701

Pinnel, N. (2019, June). *Spaceborne Imaging Spectroscopy Mission Compilation*. Retrieved from http://www.enmap.org/sites/default/files/pdf/Hyperspectral_EO_Missions_2019_06_03.pdf

Plaza, A., Benediktsson, J. A., Boardman, J. W., Brazile, J., Bruzzone, L., Camps-Valls, G., … Trianni, G. (2009). Recent advances in techniques for hyperspectral image processing. *Remote Sensing of Environment*, *113*, S110–S122. https://doi.org/10.1016/j.rse.2007.07.028

Plumlee, G. S., & Ziegler, T. L. (2003). *The medical geochemistry of dusts, soils, and other Earth materials: Chapter 7* (Vol. 9). https://doi.org/10.1016/B0-08-043751-6/09050-2

Poch, R. M., Coster, W. D., & Stoops, G. (1998). Pore space characteristics as indicators of soil behaviour in gypsiferous soils. *Geoderma*, *87*(1–2), 87–109. https://doi.org/10.1016/S0016-7061(98)00068-8

Poch, R. M., & Verplancke, H. (1997). Penetration resistance of gypsiferous horizons. *European Journal of Soil Science*, *48*(3), 535–543. https://doi.org/10.1111/j.1365-2389.1997.tb00219.x

Pratt, K. A., Twohy, C. H., Murphy, S. M., Moffet, R. C., Heymsfield, A. J., Gaston, C. J., … Prather, K. A. (2010). Observation of playa salts as nuclei in orographic wave clouds. *Journal of Geophysical Research: Atmospheres*, *115*(D15), D15301. https://doi.org/10.1029/2009JD013606

Prospero, J. M., Ginoux, P., Torres, O., Nicholson, S. E., & Gill, T. E. (2002). Environmental Characterization of Global Sources of Atmospheric Soil Dust Identified with the Nimbus 7 Total Ozone Mapping Spectrometer (toms) Absorbing Aerosol Product. *Reviews of Geophysics*, *40*(1), 1002. https://doi.org/10.1029/2000RG000095

Pye, K. (1995). The nature, origin and accumulation of loess. *Quaternary Science Reviews*, *14*(7), 653–667. https://doi.org/10.1016/0277-3791(95)00047-X

Pye, K. (2015). *Aeolian Dust and Dust Deposits*. Elsevier.

Qadir, M., Schubert, S., Ghafoor, A., & Murtaza, G. (2001). Amelioration strategies for sodic soils: A review. *Land Degradation & Development*, *12*(4), 357–386. https://doi.org/10.1002/ldr.458

Ramaswamy, V., Boucher, O., Haigh, J., Hauglustaine, D., Haywood, J., Myhre, G., … Srinivasan, J. (2001). *Radiative Forcing of Climate Change* (No. 3; pp. 351–406). Cambridge: IPCC.

Ramsey, M. S., Christensen, P. R., Lancaster, N., & Howard, D. A. (1999). Identification of sand sources and transport pathways at the Kelso Dunes, California, using thermal infrared remote sensing. *GSA Bulletin*, *111*(5), 646–662. https://doi.org/10.1130/0016-7606(1999)111<0646:IOSSAT>2.3.CO;2

Rast, M., & Painter, T. H. (2019). Earth Observation Imaging Spectroscopy for Terrestrial Systems: An Overview of Its History, Techniques, and Applications of Its Missions. *Surveys in Geophysics*, *40*(3), 303–331. https://doi.org/10.1007/s10712-019-09517-z

Reath, K. A., & Ramsey, M. S. (2013). Exploration of geothermal systems using hyperspectral thermal infrared remote sensing. *Journal of Volcanology and Geothermal Research*, *265*, 27–38. https://doi.org/10.1016/j.jvolgeores.2013.08.007

Reeves, C. C. (1978). Economic Significance of Playa Lake Deposits. In Alberttter & urice E. Tucker (Eds.), *Modern and Ancient Lake Sediments* (pp. 279–290). https://doi.org/10.1002/9781444303698.ch15

Reynolds, R. L., Yount, J. C., Reheis, M., Goldstein, H., Chavez, P., Fulton, R., … Forester, R. M. (2007). Dust emission from wet and dry playas in the Mojave Desert, USA. *Earth Surface Processes and Landforms*, *32*(12), 1811–1827. https://doi.org/10.1002/esp.1515

Richter, R., & Schläpfer, D. (2002). Geo-atmospheric processing of airborne imaging spectrometry data. Part 2: Atmospheric/topographic correction. *International Journal of Remote Sensing*, *23*(13), 2631–2649. https://doi.org/10.1080/01431160110115834

Richter, R., & Schläpfer, D. (2016, March). *Atmospheric/topographic correction for airborne imagery. ATCOR-4 User Guide*. Retrieved from http://www.rese.ch/pdf/atcor4_manual.pdf

Rogass, C., Guanter, L., Mielke, C., Scheffler, D., Boesche, N. K., Lubitz, C., … Segl, K. (2014). An automated processing chain for the retrieval of georeferenced reflectance data from hyperspectral EO-1 HYPERION acquisitions. *EARSeL 34th Symposium Proceedings*. Retrieved from http://mobile.eproceedings.org/symposia/2014-symposium-Warsaw/pdf_proceedings/EARSeL-Symposium-2014_3_1_rogass.pdf

Rogass, C., Mielke, C., Scheffler, D., Boesche, N. K., Lausch, A., Lubitz, C., … Guanter, L. (2014). Reduction of Uncorrelated Striping Noise. Applications for Hyperspectral Pushbroom Acquisitions. *Remote Sensing*, *6*(11), 11082–11106. https://doi.org/10.3390/rs61111082

Roney, J. A., & White, B. R. (2004). Definition and measurement of dust aeolian thresholds. *Journal of Geophysical Research: Earth Surface*, *109*(F1). https://doi.org/10.1029/2003JF000061

Rosen, M. R. (1994). *Paleoclimate and Basin Evolution of Playa Systems*. Boulder, Colorado, U.S.: Geological Society of America.

Roy, D. P., Wulder, M. A., Loveland, T. R., C.e., W., Allen, R. G., Anderson, M. C., … Zhu, Z. (2014). Landsat-8: Science and product vision for terrestrial global change research. *Remote Sensing of Environment*, *145*, 154–172. https://doi.org/10.1016/j.rse.2014.02.001

Roy, P. D., Smykatz-Kloss, W., & Sinha, R. (2006). Late Holocene geochemical history inferred from Sambhar and Didwana playa sediments, Thar Desert, India: Comparison and synthesis. *Quaternary International*, *144*(1), 84–98. https://doi.org/10.1016/j.quaint.2005.05.018

Saayman, C. (2013). *Environmental Impact Assessment for the proposed Otjivalunda salt mining and soap production facility: Cultural Heritage specialist studyEnvironmental Impact Assessment for the proposed Otjivalunda salt mining and soap production facility: Cultural Heritage specialist study* (p. 47). Namibia: Enviro Dynamics.

SACS (The South African Committee for Stratigraphy). (1980). *Stratigraphy of South Africa. Part 1: Lithostratigraphy of the Republic of South Africa, South West Africa/Namibia and the Republics of Bophuthatswana, Transkei and Venda* (Vol. 1). Johannesburg, South Africa: Republic of South Africa, Department of Mineral and Energy Affairs, Geological Survey.

Schuller, I., Belz, L., Wilkes, H., & Wehrmann, A. (2018). Late Quaternary shift in southern African rainfall zones: Sedimentary and geochemical data from Kalahari pans. *Zeitschrift Für Geomorphologie*, *61*(4), 339–362. https://doi.org/info:doi/10.1127/zfg/2018/0556

Segl, K., Guanter, L., Rogass, C., Kuester, T., Roessner, S., Kaufmann, H., … Hofer, S. (2012). EeteS: The EnMAP End-to-End Simulation Tool. *IEEE Journal of Selected Topics in Applied Earth Observations and Remote Sensing*, *5*(2), 522–530. https://doi.org/10.1109/JSTARS.2012.2188994

Selebatso, M., Bennitt, E., Maude, G., & Fynn, R. W. S. (2018). Water provision alters wildebeest adaptive habitat selection and resilience in the Central Kalahari. *African Journal of Ecology*, *56*(2), 225–234. https://doi.org/10.1111/aje.12439

Shao, Y., & Lu, H. (2000). A simple expression for wind erosion threshold friction velocity. *Journal of Geophysical Research: Atmospheres*, *105*(D17), 22437–22443. https://doi.org/10.1029/2000JD900304

Shaw, P. A., & Bryant, R. G. (2011). Pans, Playas and Salt Lakes. In D. S. G. Thomas (Ed.), *Arid Zone Geomorphology* (3rd ed., pp. 373–401). Retrieved from http://onlinelibrary.wiley.com/doi/10.1002/9780470710777.ch15/summary

Shaw, P. A., & Thomas, D. S. G. (1989). Pans, Playas and Salt Lakes. In D. S. G. Thomas (Ed.), *Arid Zone Geomorphology* (1st ed., pp. 184–208). London: John Wiley & Sons, Ltd.

Shrestha, D. P., Margate, D. E., van der Meer, F., & Anh, H. V. (2005). Analysis and classification of hyperspectral data for mapping land degradation: An application in southern Spain. *International Journal of Applied Earth Observation and Geoinformation*, *7*(2), 85–96. https://doi.org/10.1016/j.jag.2005.01.001

Singer, A., Zobeck, T., Poberezsky, L., & Argaman, E. (2003). The PM10and PM2·5 dust generation potential of soils/sediments in the Southern Aral Sea Basin, Uzbekistan. *Journal of Arid Environments*, *54*(4), 705–728. https://doi.org/10.1006/jare.2002.1084

Skofronick-Jackson, G., Petersen, W. A., Berg, W., Kidd, C., Stocker, E. F., Kirschbaum, D. B., … Wilheit, T. (2016). The Global Precipitation Measurement (GPM) Mission for Science and Society. *Bulletin of the American Meteorological Society*, *98*(8), 1679–1695. https://doi.org/10.1175/BAMS-D-15-00306.1

Smara, Z. H. Y. (2015). *Oblique Striping Removal in EO-1 Hyperspectral Remote Sensing Imagery*. 6. Barcelona Spain.

Smith, M., & Compton, J. S. (2004). Origin and evolution of major salts in the Darling pans, Western Cape, South Africa. *Applied Geochemistry*, *19*(5), 645–664. https://doi.org/10.1016/j.apgeochem.2003.10.003

Smoot, J. P., & Castens-Seidell, B. (1994). *Sedimentary Features Produced by Efflorescent Salt Crusts, Saline Valley and Death Valley, California*. https://doi.org/10.2110/pec.94.50.0073

Smoot, J. P., & Lowenstein, T. K. (1991). Chapter 3 Depositional Environments of Non-Marine Evaporites. In Judith L. Melvin (Ed.), *Developments in Sedimentology* (pp. 189–347). Retrieved from http://www.sciencedirect.com/science/article/pii/S0070457108702619

Soil Resources, Management and Conservation Service, & FAO (Eds.). (1990). *Management of gypsiferous soils*. Rome.

Soltaninejad, A., Ranjbar, H., Honarmand, M., & Dargahi, S. (2018). Evaporite mineral mapping and determining their source rocks using remote sensing data in Sirjan playa, Kerman, Iran. *Carbonates and Evaporites*, *33*(2), 255–274. https://doi.org/10.1007/s13146-017-0339-4

Stone, A. E. C., & Edmunds, W. M. (2012). Sand, salt and water in the Stampriet Basin, Namibia: Calculating unsaturated zone (Kalahari dunefield) recharge using the chloride mass balance approach. *Water SA*, *38*(3), 367–378. https://doi.org/10.4314/wsa.v38i3.2

Sunshine, J. M., Pieters, C. M., & Pratt, S. F. (1990). Deconvolution of mineral absorption bands: An improved approach. *Journal of Geophysical Research: Solid Earth*, *95*(B5), 6955–6966. https://doi.org/10.1029/JB095iB05p06955

Sweeney, M. R., McDonald, E. V., & Etyemezian, V. (2011). Quantifying dust emissions from desert landforms, eastern Mojave Desert, USA. *Geomorphology*, *135*(1–2), 21–34. https://doi.org/10.1016/j.geomorph.2011.07.022

Tansey, K. J., & Millington, A. C. (2001). Investigating the potential for soil moisture and surface roughness monitoring in drylands using ERS SAR data. *International Journal of Remote Sensing*, *22*(11), 2129–2149. https://doi.org/10.1080/01431160121099

Taut, T., Kleeberg, R., & Bergmann, J. (1998). Seifert Software: The new Seifert Rietveld program BGMN and its application to quantitative phase analysis. *Materials Structure*, *5*(1), 57–66.

Tavin, F., Roman, A., Mathieu, S., Baret, F., Liu, W., & Gouton, P. (2008). Comparison of Metrics for the Classification of Soils Under Variable Geometrical Conditions Using Hyperspectral Data. *IEEE Geoscience and Remote Sensing Letters*, *5*(4), 755–759. https://doi.org/10.1109/LGRS.2008.2005212

Telfer, M. (2006). *Late Quaternary aeolian activity and palaeoenvironments of the southwestern Kalahari. Advances from an intensive chronometric investigation at Witpan, South Africa*. University of Sheffield.

Telfer, M. W., Thomas, D. S. G., Parker, A. G., Walkington, H., & Finch, A. A. (2009). Optically Stimulated Luminescence (OSL) dating and palaeoenvironmental studies of pan (playa) sediment from Witpan, South Africa. *Palaeogeography, Palaeoclimatology, Palaeoecology*, *273*(1), 50–60. https://doi.org/10.1016/j.palaeo.2008.11.012

The MathWorks, Inc. (2016). *MATLAB and Statistics Toolbox Release 2016b*.

Thomas, A. D., Dougill, A. J., Elliott, D. R., & Mairs, H. (2014). Seasonal differences in soil CO2 efflux and carbon storage in Ntwetwe Pan, Makgadikgadi Basin, Botswana. *Geoderma*, *219–220*, 72–81. https://doi.org/10.1016/j.geoderma.2013.12.028

Thomas, D., & Shaw, P. A. (1991). *The Kalahari Environment*. Cambridge, UK: Cambridge University Press.

Thome, K. J., Biggar, S. F., & Wisniewski, W. (2003). Cross comparison of EO-1 sensors and other Earth resources sensors to Landsat-7 ETM+ using Railroad Valley Playa. *IEEE Transactions on Geoscience and Remote Sensing*, *41*(6), 1180–1188. https://doi.org/10.1109/TGRS.2003.813210

Todd, M. C., Washington, R., Martins, J. V., Dubovik, O., Lizcano, G., M'Bainayel, S., & Engelstaedter, S. (2007). Mineral dust emission from the Bodélé Depression, northern Chad, during BoDEx 2005. *Journal of Geophysical Research: Atmospheres*, *112*(D6), D06207. https://doi.org/10.1029/2006JD007170

Tompkins, S. (1997). Optimization of endmembers for spectral mixture analysis. *Remote Sensing of Environment*, *59*(3), 472–489. https://doi.org/10.1016/S0034-4257(96)00122-8

Turk, L. J. (1970). Evaporation of Brine: A Field Study on the Bonneville Salt Flats, Utah. *Water Resources Research*, *6*(4), 1209–1215. https://doi.org/10.1029/WR006i004p01209

Ungar, S. G., Pearlman, J. S., Mendenhall, J. A., & Reuter, D. (2003). Overview of the Earth Observing One (EO-1) mission. *IEEE Transactions on Geoscience and Remote Sensing*, *41*(6), 1149–1159. https://doi.org/10.1109/TGRS.2003.815999

USGS. (2015). *Product Guide. Provisional Landsat 8 Surface Reflectance Product* (No. v1.8; p. 27). Retrieved from United States Geological Survey website: http://landsat.usgs.gov/documents/provisional_l8sr_product_guide.pdf

USGS. (2016). *Landsat 8 (L8) Data Users Handbook* (No. Version 2). Sioux Falls, SD, USA: United States Geological Survey (USGS).

USGS. (2017). *Product Guide. Landsat 8 Surface Reflectance Code (LaSRC) Product.* (No. 4.2; p. 39). Retrieved from United States Geological Survey website: https://landsat.usgs.gov/sites/default/files/documents/lasrc_product_guide.pdf

van der Linden, S., Rabe, A., Held, M., Jakimow, B., Leitão, P. J., Okujeni, A., … Hostert, P. (2015). The EnMAP-Box—A Toolbox and Application Programming Interface for EnMAP Data Processing. *Remote Sensing*, *7*(9), 11249–11266. https://doi.org/10.3390/rs70911249

Van der Meer, F. (2004). Analysis of spectral absorption features in hyperspectral imagery. *International Journal of Applied Earth Observation and Geoinformation*, *5*(1), 55–68. https://doi.org/10.1016/j.jag.2003.09.001

Veleen, M. van, & Baker, T. (2009). *Feasibility Study of the Potential for Sustainable Water Resources Development in the Molopo-Nossob Watercourse*.

Veraverbeke, S., Dennison, P., Gitas, I., Hulley, G., Kalashnikova, O., Katagis, T., … Stavros, N. (2018). Hyperspectral remote sensing of fire: State-of-the-art and future perspectives. *Remote Sensing of Environment*, *216*, 105–121. https://doi.org/10.1016/j.rse.2018.06.020

Verbesselt, J., Hyndman, R., Newnham, G., & Culvenor, D. (2010). Detecting trend and seasonal changes in satellite image time series. *Remote Sensing of Environment*, *114*(1), 106–115. https://doi.org/10.1016/j.rse.2009.08.014

Verbesselt, J., Zeileis, A., & Herold, M. (2012). Near real-time disturbance detection using satellite image time series. *Remote Sensing of Environment*, *123*, 98–108. https://doi.org/10.1016/j.rse.2012.02.022

Vermote, E., Justice, C., Claverie, M., & Franch, B. (n.d.). Preliminary analysis of the performance of the Landsat 8/OLI land surface reflectance product. *Remote Sensing of Environment*. https://doi.org/10.1016/j.rse.2016.04.008

Vickery, K. J., Eckardt, F. D., & Bryant, R. G. (2013). A sub-basin scale dust plume source frequency inventory for southern Africa, 2005-2008. *Geophysical Research Letters*, *40*(19), 5274–5279. https://doi.org/10.1002/grl.50968

Wadge, G., & Archer, D. J. (2003). Evaporation of groundwater from arid playas measured by C-band SAR. *IEEE Transactions on Geoscience and Remote Sensing*, *41*(7), 1641–1650. https://doi.org/10.1109/TGRS.2003.813747

Warren, J. K. (2016). *Evaporites: A Geological Compendium*. Springer.

Washington, R., Todd, M., Middleton, N. J., & Goudie, A. S. (2003). Dust-Storm Source Areas Determined by the Total Ozone Monitoring Spectrometer and Surface Observations. *Annals of the Association of American Geographers*, *93*(2), 297–313. https://doi.org/10.1111/1467-8306.9302003

Weindorf, D. C., Chakraborty, S., Herrero, J., Li, B., Castañeda, C., & Choudhury, A. (2016). Simultaneous assessment of key properties of arid soil by combined PXRF and Vis–NIR data. *European Journal of Soil Science*, *67*(2), 173–183. https://doi.org/10.1111/ejss.12320

White, K., & Eckardt, F. (2006). Geochemical mapping of carbonate sediments in the Makgadikgadi basin, Botswana using moderate resolution remote sensing data. *Earth Surface Processes and Landforms*, *31*(6), 665–681. https://doi.org/10.1002/esp.1289

Whiting, M. L., Li, L., & Ustin, S. L. (2004). Predicting water content using Gaussian model on soil spectra. *Remote Sensing of Environment*, *89*(4), 535–552. https://doi.org/10.1016/j.rse.2003.11.009

Wierzchos, J., Davila, A. F., Sánchez-Almazo, I. M., Hajnos, M., Swieboda, R., & Ascaso, C. (2012). Novel water source for endolithic life in the hyperarid core of the Atacama Desert. *Biogeosciences*, *9*(6), 2275–2286. https://doi.org/10.5194/bg-9-2275-2012

WMO. (2008). *Guide to meteorological instruments and methods of observation.* Geneva, Switzerland: World Meteorological Organization.

Wood, W. W., & Sanford, W. E. (1995). Eolian transport, saline lake basins, and groundwater solutes. *Water Resources Research*, *31*(12), 3121–3129. https://doi.org/10.1029/95WR02572

Wulder, M. A., Masek, J. G., Cohen, W. B., Loveland, T. R., & Woodcock, C. E. (2012). Opening the archive: How free data has enabled the science and monitoring promise of Landsat. *Remote Sensing of Environment*, *122*, 2–10. https://doi.org/10.1016/j.rse.2012.01.010

Xu, H. (2006). Modification of normalised difference water index (NDWI) to enhance open water features in remotely sensed imagery. *International Journal of Remote Sensing*, *27*(14), 3025–3033. https://doi.org/10.1080/01431160600589179

Yang, X., Zhao, S., Qin, X., Zhao, N., & Liang, L. (2017). Mapping of Urban Surface Water Bodies from Sentinel-2 MSI Imagery at 10 m Resolution via NDWI-Based Image Sharpening. *Remote Sensing*, *9*(6), 596. https://doi.org/10.3390/rs9060596

Yechieli, Y., & Wood, W. W. (2002). Hydrogeologic processes in saline systems: Playas, sabkhas, and saline lakes. *Earth-Science Reviews*, *58*(3–4), 343–365. https://doi.org/10.1016/S0012-8252(02)00067-3

Zazi, L., Boutaleb, A., & Guettouche, M. S. (2017). Identification and mapping of clay minerals in the region of Djebel Meni (Northwestern Algeria) using hyperspectral imaging, EO-1 Hyperion sensor. *Arabian Journal of Geosciences*, *10*(11), 252. https://doi.org/10.1007/s12517-017-3015-z

Zhang, L., Liao, M., Yang, L., & Lin, H. (2007). Remote sensing change detection based on canonical correlation analysis and contextual Bayes decision. *Photogrammetric Engineering & Remote Sensing*, *73*(3), 311–318.

Zhang, Xia, Shang, K., Cen, Y., Shuai, T., & Sun, Y. (2014). Estimating ecological indicators of karst rocky desertification by linear spectral unmixing method. *International Journal of Applied Earth Observation and Geoinformation*, *31*, 86–94. https://doi.org/10.1016/j.jag.2014.03.009

Zhang, Xiya, & Li, P. (2014). Lithological mapping from hyperspectral data by improved use of spectral angle mapper. *International Journal of Applied Earth Observation and Geoinformation*, *31*, 95–109. https://doi.org/10.1016/j.jag.2014.03.007

Appendix

Acknowledgments

I owe gratitude to many people for the completion of this thesis. First and foremost, I would like to give my special thanks to Dr. Sabine Chabrillat for many years of intense mentoring, generosity, and support both academically and personally. Your guidance was substantial, yet so sensitive that I always felt as if I had found my own way. Your experience and encouragement got me through the many difficult stages and your knowledge and ideas were always inspiring. Also, many thanks to Dr. Thomas Schmid for sharing his great experience in soil spectroscopy and associated field work with me.

I want to thank Prof. Dr. Hermann Kaufmann and Prof. Dr. Luis Guanter, the heads of the remote sensing section during the time of my thesis, for giving me lots of freedom in my work while always "having an open door" for questions and discussions and also for providing a great working atmosphere. I would like to thank all my colleagues of the Remote Sensing and Geoinformatics Section at GFZ Potsdam. It is incredible to witness the pleasant and friendly working climate. All the people are kind and very helpful. There is a lively professional exchange between all colleagues, as well as plentiful non-scientific conversations during the coffee breaks.

I want to thank Prof. Dr. Bodo Bookhagen for his supervision at the University of Potsdam. Thank you for acting as first reviewer and for helping with the official formalities, and your advices in the context of my thesis.

Many thanks to Dr. Robert Behling and Daniel Berger for their support during several field campaigns. You have been very patient, hard-working and yet always cheerful, making field work in the Kalahari efficient yet fun. Many thanks to Dr. Maximilian Brell for his help and expertise in airborne data processing. Thanks to Sylvia Magnussen for record time solutions to really all hard- and software related difficulties.

Finally, I want to thank my family and friends for moral and emotional support during the long period of my thesis. A big thank you goes to my parents for the steady support during my studies, as well as for the freedom and trust in all my life decisions. Cheers!